공학박사 학위논문

Projection-based Hyper Reduced-order Modeling and its Application for Nonlinear Structural Dynamics

투영기반 하이퍼 차수축소모델링 및 비선형 구조 동역학에 대한 응용 연구

2023 년 2 월

서울대학교 대학원

항공우주공학과

김 용 세

Projection-based Hyper Reduced-order Modeling and its Application for Nonlinear Structural Dynamics

투영기반 하이퍼 차수축소모델링 및 비선형 구조 동역학에 대한 응용 연구

지도교수 신 상 준

이 논문을 공학박사 학위논문으로 제출함

2022 년 12 월

서울대학교 대학원
항공우주공학과
김 용 세

김용세의 공학박사 학위논문을 인준함

2022 년 12 월

위 원 장 윤 군 진 (인)

부위원장 신 상 준 (인)

위 원 양 진 규 (인)

위 원 조 해 성 (인)

위 원 이 두 열 (인)

Abstract

Projection-based Hyper Reduced-order Modeling and its Application for Nonlinear Structural Dynamics

Yongse Kim

Department of Aerospace Engineering

The Graduate School

Seoul National University

In this dissertation, a finite element (FE)-based nonlinear analysis framework capable of predicting the geometric nonlinearity is developed. A nonlinear dynamic simulation requires large computation owing to its iterative solution algorithm. To reduce the anticipated computational expense, a projection-based reduced-order modeling (ROM) combine with hyper-reduction will be applied. To efficiently perform the computation, the following three hyper-reduction approaches will be employed to approximate the nonlinear finite-element matrices: discrete empirical interpolation method (DEIM), Gauss–Newton with approximated tensors (GNAT), and energy-conserving sampling and weighting (ECSW). The present frameworks are applied to the time-transient simulation of a propeller, including the parametrized material and load properties. Compared with DEIM approach, GNAT and ECSW approaches exhibit better enhancement in terms of the accuracy and robustness of

the reduced-order representation. Additionally, the computational efficiency of ECSW approach is improved significantly compared with that of the other projection-based ROM approaches.

On the other hand, if FE representation varies owing to the geometric defect or imperfection, the reduced order representation will be expensively reconstructed. To avoid such computational inefficiency, an improved nonlinear reduced-order modeling technique capable of describing the parametrized shape defect will be proposed. In the proposed framework, the reduced-order representation is created in a polynomial form comprised a set of reduced-tensor coefficients of defect and physical displacement field. However, constructing the reduced tensors using a large number of discretized elements usually requires enormous amounts of the computational resources. Therefore, to reduce the computational expense, a quadratic-manifold-based ECSW approach will be employed to obtain the reduced tensors concerning only a few optimally selected elements. This approach can be used to conduct both time-transient and frequency response analyses on the rotating mechanical components. It is found that the proposed approach can accurately estimate the broad defect-parametric variation. In particular, its computational efficiency demonstrates a significant improvement in contrast to that of the existing approaches.

Keywords: **Projection-based model-order reduction, Proper orthogonal decomposition, Geometric nonlinearity, Structural dynamics Hyper-reduction, Defect-parametric reduced-order model**

Student Number: 2019-32693

Contents

Page

List of Tables

Page

List of Figures

Page

Chpater 1

Introduction

1.1 Background and Motivation

The mechanical and aerospace hardware (Fig. 1.1) such as the turbomachinery, aircraft propeller, and wings usually operate under severe condition owing to large power requirement. In particular, rotating components such as turbine blades and propellers exhibit large displacement owing to the high-speed rotation and periodic aerodynamic excitation, called as the forced vibration (Fig. 1.2). Moreover, complex design for improving the aerodynamic performance, such as twisted-surfaced, increased slenderness, and the larger-aspect ratio of the relevant geometric shape, might cause considerable influence on their geometric nonlinearity. A geometrically nonlinear simulation based on the larger dimensional representation, usually by the finite element (FE) method [1], is considered an indispensable method of assessing their structural integrity during the design process. However, the relevant nonlinear analysis consumes significant amount of time, owing to its iterative solution procedure. Additionally, multi-fidelity analysis strategies, such as the fluid-structure interaction and design optimization, which involve large number of the parametric simulations, consume substantially larger amount of the computing resource. While the parallel computing based on the domain decomposition method (e.g. finite element tearing and interconnecting (FETI) [2] may be capable of the large-size

simulation as the computation is performed in a distributed manner, it will not reduce memory requirement.

Instead, the model-order reduction (MOR) techniques have been proposed as the viable means for reducing the relevant computational expense. MOR aims to reduce the dimensions of the full-order model (FOM), that is, the construction of a reduced-order model (ROM) along with the minimal loss of accuracy. In other words, MOR is able to describe the key characteristics by reducing the number of degrees of freedom (DOFs) of the representation (Fig. 1.3). Therefore, the large-size simulation can be performed faster and cheaper, yet acceptably represent the original large-size object. Generally, MOR procedure comprises a computationally expensive off-line stage, wherein ROM is constructed and executed in an efficient online stage. During the off-line stage, a set of samples will be collected from the numerous simulations, using the high-fidelity analysis. The relevant solutions are used to construct the reduced-order representation. During the online stage, the simulation will be executed using the reduced-order representation. Once ROMs are constructed, it will be possible to obtain fast and accurate solution. In other words, repeated computations can be performed for a variety of different conditions without going through the off-line stage processes (Fig. 1.4).

The various MOR techniques (Fig. 1.5) have been developed and introduced in many fields such as the mechanical, aerospace, chemistry, biomedicine, microelectronic, and neuroscience, etc. Furthermore, MOR technique has been recently utilized for the advanced structural maintenance or design (e.g. structural

health monitoring (SHM) or condition-based maintenance (CBM)) based on a predictive digital twin technology which essentially requires a real-time solution.

In the following sections, the previous studies regarding the relevant MOR techniques will be discussed.

Fig. 1.1 Mechanical and aerospace components

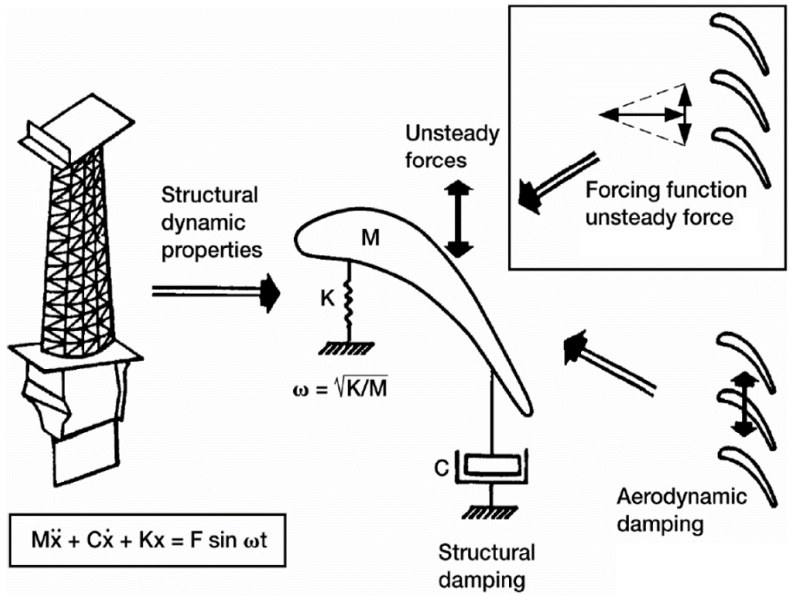

Fig. 1.2 Primary elements of the forced vibration [3]

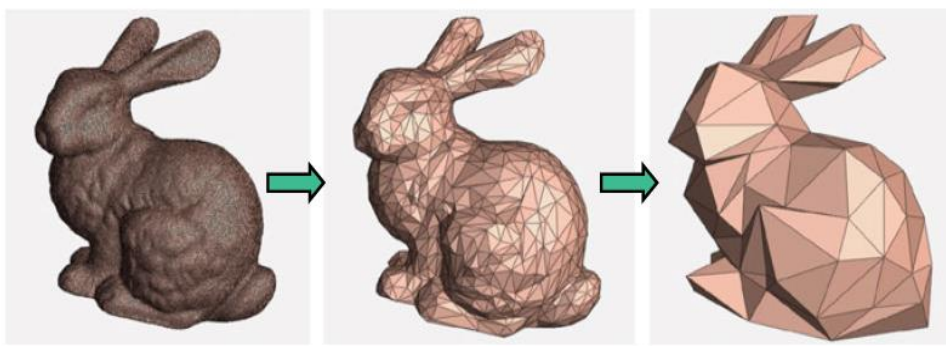

Fig. 1.3 Graphical illustration of the model order reduction [4]

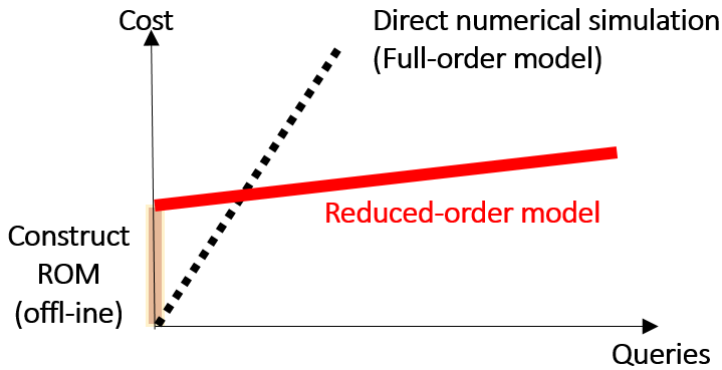

Fig. 1.4 Computational cost in the MOR

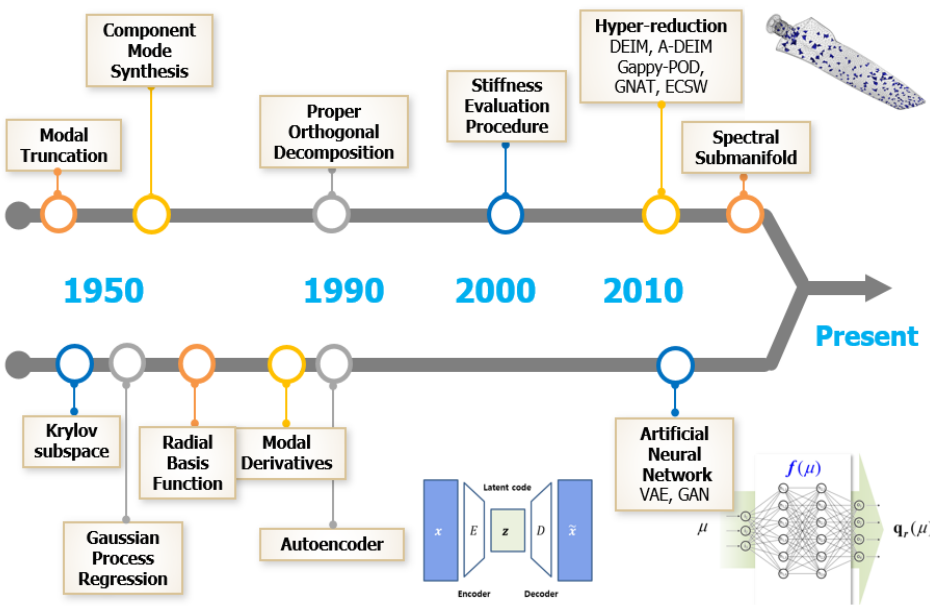

Fig. 1.5 Techniques for the MOR

1.2 Literature Review

1.2.1 Projection-based Model-order Reduction

There are two different types of approaches for constructing ROMs in the off-line stage: data-fitting- and projection-based approaches (Fig. 1.6). Data-fitting based MOR uses the relationship between the input parameter and output result directly for constructing ROMs. The resulting ROM is constructed as a black box and is independent of the governing formulation. This will be implemented by applying either regression or interpolation techniques (e.g. radial basis function [5], Gaussian process [6], Grassman manifold [7], autoencoder [8], and neural network [9, 10]) on the full-order simulation solution. These approaches have been applied to nonlinear systems such as structural dynamics [11], design optimization [12], fluid dynamics [13], and combustion problem [14].

The data-fitting-based MOR does not require knowledge of the system governing equation or the problem physics. In this respect, it will be an advantage if only a commercial software solver is available for ROM construction. However, the data fitting-based MOR will typically require extensive FOM computations and corresponding solutions in the off-line stage. This may significantly affect the overall computational cost, including the off-line cost.

Projection-based MOR [15] builds a reduced-order representation by projecting the larger-dimensional system of equations onto a reduced basis (i.e. Galerkin projection). Therefore, such ROM techniques will retain the properties of the original governing equation, and a solution algorithm with system consistency applied to the

full-order representation may be used on the reduced one. Moreover, the off-line computational cost will be lower than that of the data fitting-based MOR.

In this dissertation, the projection-based MOR technique will be applied to deal with the geometrically nonlinear behavior of a structural component in the reduced space. In the context of the nonlinear solid mechanics, the projection-based MOR technique will differ based on the selection of the reduced basis which span the original (full-order) representation solution subspace. Furthermore, it will be different for different methodologies that are available for reduced nonlinear term approximation, such as the internal force and tangent stiffness matrix.

Selection of the Reduced Basis

Regarding the reduced basis selection, there exist two main approaches: data- and model-driven. In the data-driven approach, the reduced basis will be usually obtained from the precomputed FOM result, called as the snapshot. Proper orthogonal decomposition (POD) [16] is a representative and favored data-driven approach, and whose basis comprises the snapshots' leading principal component. POD-based ROMs have been utilized in the various fields, including aeroelasticity, controls and optimization [17–19]. In the structural analysis framework, POD-based ROMs have been successfully applied to both linear and nonlinear formulations and enhanced computational efficiency [20–22].

Conversely, the model-driven approach directly derives the reduced basis from the discretized formulation for FOM, also known as the data-free approach. Although

the model-based approach is not widely used as the data-driven approach based on POD, it will not require a high-cost FOM simulation, especially for the solid analysis. Free vibration modes, i.e., the eigenvectors of the undamped linear system, are one of the well-known reduced basis vectors for the linear structural dynamics. In contrast, modal derivatives [23, 24], dual modes [25–27] approaches have been utilized for the nonlinear structural dynamics.

Approximation of the Reduced Nonlinear Terms

The reduced nonlinear term may be approximated by either the non-intrusive or intrusive method. In the non-intrusive method, the reduced nonlinear term is described as a polynomial form of the reduced coordinates with the stiffness coefficients, which will in turn be determined from the sufficient nonlinear static simulation (compatible with the commercial FE software) with the imposed displacements or forces. The stiffness-evaluation procedure (STEP) [28, 29], implicit condensation, and expansion (ICE) [30] have been used for the non-intrusive projection-based reduction method. Recent studies are found in [31–33].

In the intrusive method, the reduced nonlinear term will be approximated directly by projecting the full-order nonlinear term onto the reduced basis at an element level. Therefore, a systematic access to FE formulation is required, unlike the non-intrusive methods. However, for the nonlinear simulation, which have a larger number of degrees of freedom (DOFs), will require repetitive projection processes of the large number of nonlinear terms via the reduced basis. This may incur significant

computational time and resources. Specifically, for a linear time-transient formulation, the projection-based ROM can be easily expressed by the time-invariant equations. By contrast, a nonlinear time-transient formulation will usually attempt to solve simultaneous linearized time-varying equations using an appropriate iterative-solution algorithm.

To compensate for such computational inefficiency, sparse-sampling methods, including hyper-reduction, have been suggested. The hyper-reduction approach can alleviate such computational bottlenecks, allowing the reconstruction of the nonlinear term in the reduced dimension by using either a few sampling points or a reduced number of meshes. As a result, the computational cost for constructing the reduced-order representation will be decreased significantly by using the reduced nonlinear term during the recursive projection.

One representative approach is the discrete empirical interpolation method (DEIM) proposed by Chaturantabut and Sorensen [34]. DEIM, a discrete version of EIM [35], uses interpolation to determine the optimality of nonlinear terms in the reduced-order basis. This will enable an approximation of the non-affinely parameterized functions. DEIM has been employed in nonlinear structural dynamics, including elastoplasticity [36], hyper-elasticity [37], and viscoplasticity [38]. Negri et al. and Bonomi et al. suggested a matrix version of DEIM (MDEIM) as an extension of DEIM [39, 40]. It was used to efficiently approximate Jacobian matrices, i.e., to find an optimality in the reduced-order basis for a tangent matrix. Willcox [41] recommended the missing-point estimation approach using gappy-POD, which used

regression to approximate the nonlinear terms. That method was successfully applied to the unsteady flow sensing.

In the hyper-reduction approach, the reliability and computational efficiency of ROM are usually determined by the quality sampling points. Hence, neither DEIM nor gappy-POD leads to a reliable solution because they use an insufficient number of sampling points [42]. Subsequent investigations discovered the convergence difficulties induced by the non-symmetry of the matrices in the POD-based ROM, in combination with either DEIM or gappy-POD [43, 44].

As an alternative to Galerkin projection, Gauss-Newton with approximated tensors (GNAT) was proposed by Carlberg et al. [45]. GNAT will approximate the nonlinear terms by solving using the low-cost least-squares approach, and it will enable the resulting ROM to obtain a stable solution. Moreover, POD-based ROMs combined with GNAT were applied to the fluid dynamics [46] and microscopic formulation [47], and its numerical stability and computational efficiency were verified. Farhat et al. [48] proposed an energy-conserving sampling and weighting (ECSW) method that directly approximated the reduced nonlinear terms while preserving their numerical stability. ECSW considers the virtual work of FE-based dynamic system to define the reduced meshes and their relevant weights. This approach achieved sufficient accuracy and numerical stability for the structural and turbulent problems [49, 50].

However, in the hyper-reduction approach, a smaller number of the selected elements are typically chosen from the training set specified by the nonlinear FOM

simulation. Those simulations may incur a computationally expensive off-line stage. Jain et al. [51] proposed the quadratic manifold (QM)-based reduction approach to inexpensively generate the training set for ECSW. In this approach, the nonlinear full-order solution was obtained via nonlinear mapping of the inexpensive linear modal solution.

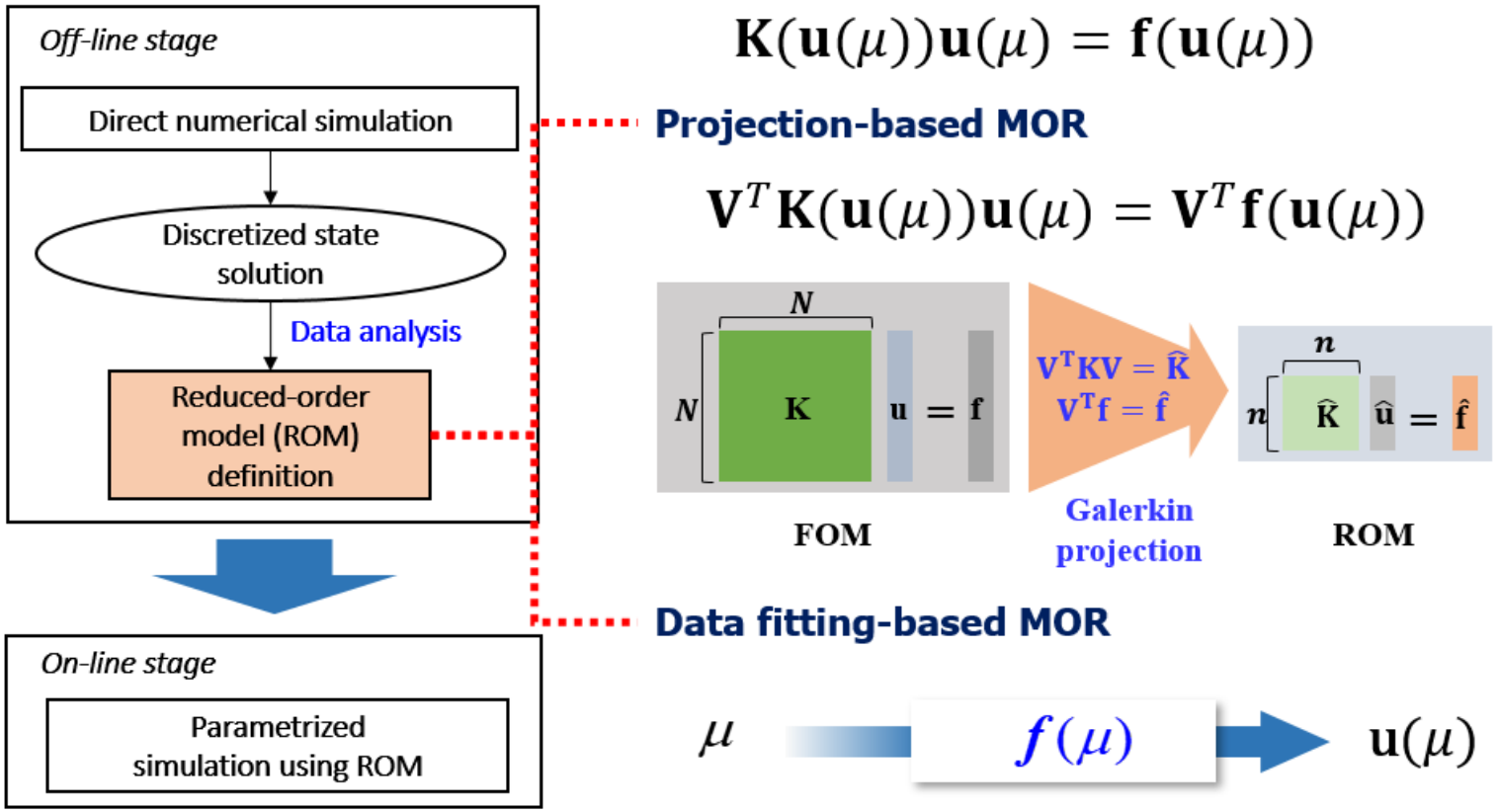

Fig. 1.6 Projection- and Data fitting-based MOR.

1.2.2 Parametric Reduced-order Modeling for a Shape Imperfection

The aforementioned FE-based nonlinear ROMs typically use a nominal representation (blueprint), which refer to the geometry without any imperfection or shape deformation. However, considering the structural design or optimization process, even small geometric defect, such as the mistuning of the turbine blade [52] and manufacturing imperfection [53, 54], may significantly affect the dynamic characteristics of the entire component. Therefore, numerous repeated simulations considering the probability of various geometric defect, such as the stochastic analysis via Monte Carlo simulation [55], will be required. Therefore, it is necessary to develop an improved FE representation that includes the shape defect by varying the geometry (e.g., CAD drawing modification) and discretizing elements, or directly shifting the nominal FE discretization node location. Then, the resulting ROM will be constructed to solve the resulting nonlinear problem. This procedure will be repeated whenever the shape defects are varied, which will significantly decrease the efficiency owing to an increase in the off-line computational expense.

To avoid such computational inefficiency, Marconi. et al. [56] suggested a nonlinear parametric ROM for the geometric nonlinearity and parametrized geometric defect, which is known as the defect-parametric reduced-order model (DpROM). In DpROM, the pre-determined displacement field of the shape defect or the nonuniformity from the nominal FE representation will be inserted in the strain formulation. By using such modified approximation, the nonlinear internal forces will be represented as a polynomial function comprised of the tensor coefficients

concerning the defect- and practical displacement fields. Those full-order tensors will be reduced via Galerkin projection using the selected reduced basis at an element level, that is, during the assembly procedure for the discretized elements. Moreover, in [57], DpROM was improved by introducing the higher-order strain approximation exploiting Neumann expansion, which achieved a higher accuracy. DpROM based on such intrusive tensorial approach was successfully applied to MEMS gyroscope components with a set of defect-shape [57], as shown in Fig. 1.7.

However, considering that the full-order tensors in DpROM framework containing up to the higher-order elements will be evaluated for each element, a large number of Galerkin projections and assembling procedures will be required. This will directly influence the off-line cost for constructing the reduced tensor. Therefore, large discretization and the increased number of DOFs may result in computational inefficiency and out-of-resource situation.

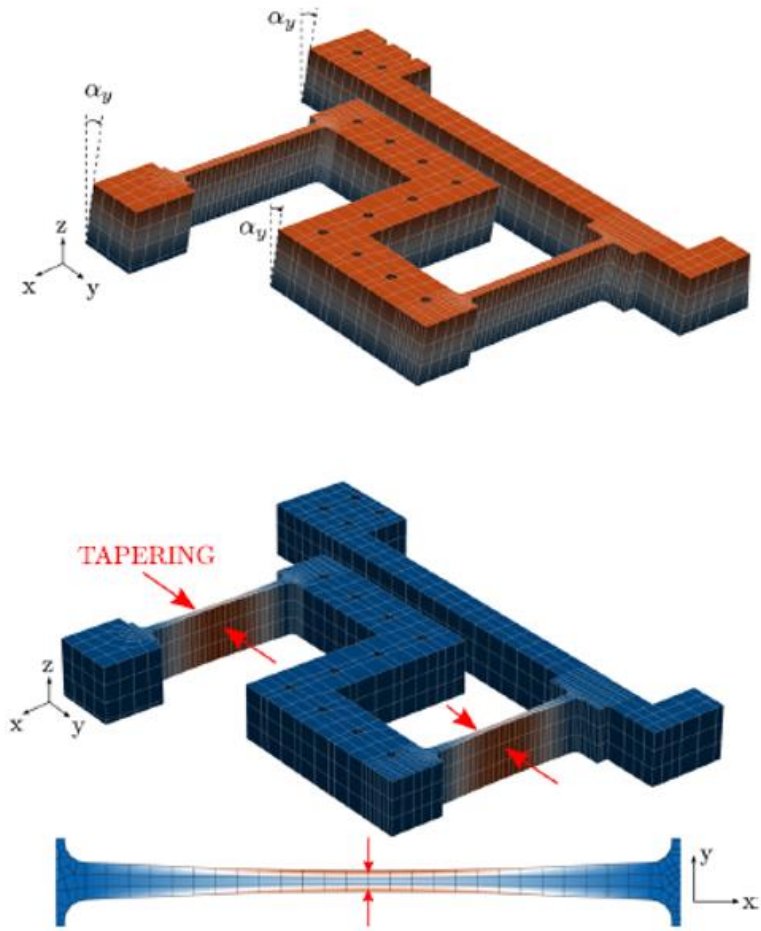

Fig. 1.7 MEMS gyroscope component with a set of defect-shape (wall angle and tapering defects) [57].

1.3 Objectives and Contributions

The objective of this dissertation is to develop a projection-based ROM and systematically evaluate the resulting ones regarding the prediction capability for the nonlinear formulation accurately and quickly. In particular, the hyper-reduction approach will be introduced to alleviate the computational bottleneck that the projection-based ROM requires the repetitive multiplications of the huge nonlinear terms by the reduced basis. To achieve such goal, various hyper-reduction-based ROMs will be developed and verified by applying the present approach to the structural components such as the aircraft propeller and turbine blades. Moreover, DpROM combined with the hyper-reduction will be developed to mitigate the issues in the off-line stage, such as the computational burden resulting from an increased number of the element-level tensors. Herein, the hyper-reduction approach will be employed to evaluate and assemble the element-level tensor by using only a few selected elements.

The novel contributions of this dissertation may be summarized as follows:

- Hyper-reduction-based ROMs based on the three-dimensional finite element are developed to handle the geometrically nonlinear formulation.

- A systematic comparison of the hyper-reduction-based ROMs will be performed, specifically those related to the geometrically nonlinear structural dynamics of the rotating component, which is published in [58].

- Various and practical application of the hyper-reduction-based ROMs will be examined for the nonlinear structural dynamics, i.e., modal, time-transient, and forced vibration, which are published in [58, 59]

- An improved parametric reduced-order modeling technique by the hyper-reduction will be developed for a geometrically imperfect component, which is published in [60, 61].

1.4 Outline of Dissertation

To provide an outline of this dissertation, the contents of the chapters are presented in the following.

In Chapter 2, the projection-based MOR technique will be presented. The reduced bases for the structural dynamics will be introduced. Then, a reduced-order representation by the reduced basis will be presented in a context of the geometrically nonlinear dynamic formulation. Moreover, an explicit tensorial representation will be presented.

In Chapter 3, the hyper-reduction approaches, i.e., DEIM, GNAT, and ECSW, will be described in detail. Moreover, the hyper reduced-order representation for the nonlinear dynamics will be presented.

In Chapter 4, the hyper-reduction-based ROMs will be applied to a rotating component. Then, the obtained results will be compared against those obtained using the other ROM approaches, in terms of the accuracy, stability, and computational efficiency. In addition, their strengths and weaknesses will be discussed.

In Chapter 5, an improved DpROM framework based on the hyper-reduction will be presented. Numerical examination will be performed to evaluate whether the present DpROM framework is capable of accurately and rapidly predicting the

structural dynamics of the rotating components which possess the shape defect and geometrically nonlinear characteristics.

Finally, concluding remarks and future works will be presented in Chapter 6.

Chpater 2

Projection-based Model-order Reduction Technique

2.1 Key Concept of the Projection-based MOR

Fundamentals and relevant formulations of the projection-based MOR will be described in this section. The projection-based MOR constructs a reduced-order representation (with a small n-DOFs) by directly projecting the full-order representation (with a large N-DOFs) onto the reduced basis **V**, as shown in Fig. 2.1. Such procedure is called as Galerkin projection.

For an FE-based nonlinear dynamic system, the discretized nonlinear structural formulation for the full-order representation can be expressed as follows:

$$\mathbf{M}\ddot{\mathbf{u}} + \mathbf{C}\dot{\mathbf{u}} + \mathbf{f}_{int}(\mathbf{u}) = \mathbf{f}_{ext} \tag{2.1}$$

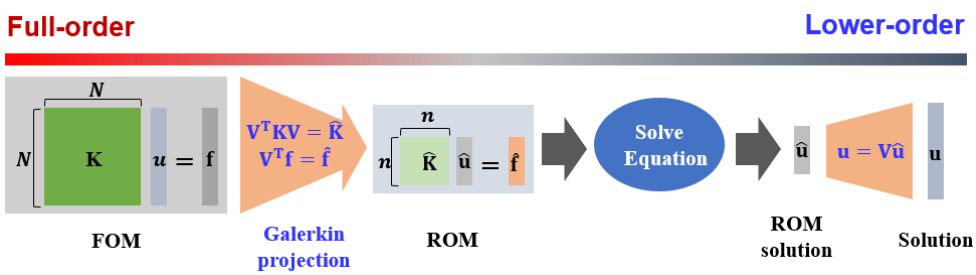

Fig. 2.1 Concept of the Projection-based MOR.

where $\mathbf{M} \in \mathbb{R}^{N\times N}$, $\mathbf{C} \in \mathbb{R}^{N\times N}$, $\mathbf{f}_{int} \in \mathbb{R}^{N}$, and $\mathbf{f}_{ext} \in \mathbb{R}^{N}$ indicate the constant mass matrix, linear proportional damping matrix based on an initial configuration, internal and external force vector, respectively. $\mathbf{u} \in \mathbb{R}^{N}$, $\dot{\mathbf{u}} \in \mathbb{R}^{N}$, and $\ddot{\mathbf{u}} \in \mathbb{R}^{N}$, are the unknown vectors, i.e., displacement, velocity, and acceleration, respectively. N denotes the dimension of the full-order representation. Each vector is a function of the unknown vectors. In case of a linear system, $\mathbf{f}_{int}(\mathbf{u})$ in Eq. (2.1) may be replaced by $\mathbf{K}|_{eq}\mathbf{u}$, in which $\mathbf{K}|_{eq}$ is the stiffness matrix, i.e., Jacobian of the internal force $\partial \mathrm{f}(\mathbf{u})/\,\partial \mathbf{u}|_{u=0}$.

To reduce the full-order representation, Eq. (2.1), the generalized coordinate vector $\mathbf{u}$ will be approximated as a weighted linear combination of the set of the reduced basis vectors.

$$\mathbf{u} \approx \mathbf{V}\boldsymbol{\eta}, \tag{2.2}$$

where $\mathbf{V} \in \mathbb{R}^{N\times n}$ and the $\boldsymbol{\eta} \in \mathbb{R}^{n}$ denote the reduced basis and reduced coordinate vector, respectively.

By substituting Eq. (2.2) into Eq. (2.1), the resulting representation is as follows:

$$\mathbf{M}\mathbf{V}\ddot{\boldsymbol{\eta}} + \mathbf{C}\mathbf{V}\dot{\boldsymbol{\eta}} + \mathbf{f}_{int}(\mathbf{V}\boldsymbol{\eta}) = \mathbf{f}_{ext} + \mathbf{r}, \tag{2.3}$$

where $\mathbf{r}$ denotes the residual originated from the approximation.

In order for Eq. (2.3) to be uniquely determined, the residual $\mathbf{r}$ will be constrained to be orthogonal to the column space of the reduced subspace $\mathbf{V}$:

$$\mathbf{V}^{T}\mathbf{r} = \mathbf{0}. \tag{2.4}$$

This results in

$$\underbrace{\mathbf{V}^T\mathbf{M}\mathbf{V}}_{\hat{\mathbf{M}}}\ddot{\boldsymbol{\eta}} + \underbrace{\mathbf{V}^T\mathbf{C}\mathbf{V}}_{\hat{\mathbf{C}}}\dot{\boldsymbol{\eta}} + \underbrace{\mathbf{V}^T\mathbf{f}_{int}(\mathbf{V}\boldsymbol{\eta})}_{\hat{\mathbf{f}}_{int}} = \underbrace{\mathbf{V}^T\mathbf{f}_{ext}}_{\hat{\mathbf{f}}_{ext}}, \tag{2.5}$$

where ^ denotes the components of the reduced-order representation. $\hat{\mathbf{M}} \in \mathbb{R}^{n\times n}$, $\hat{\mathbf{C}} \in \mathbb{R}^{n\times n}$, $\hat{\mathbf{f}}_{int} \in \mathbb{R}^n$, and $\hat{\mathbf{f}}_{ext} \in \mathbb{R}^n$ indicate the reduced constant mass matrix, reduced damping matrix, reduced internal force vector and external force vector, respectively.

It is noted that the reduced-order representation, Eq. (2.5), can be preserved the symmetric properties. Also, the reduced terms $\hat{\mathbf{M}}$, $\hat{\mathbf{C}}$, and $\hat{\mathbf{f}}_{ext}$ will be pre-computed in the off-line stage. However, the reduced nonlinear internal force $\hat{\mathbf{f}}_{int}$ still need to be evaluated under the full-order representation in the online stage. Therefore, an efficient computation of $\hat{\mathbf{f}}_{int}$ will determine the online expense of the projection-based ROM.

Furthermore, as mentioned in Introduction, the reduced basis $\mathbf{V}$ will play an important role for constructing an accurate ROM in the projection-based MOR framework. Representative approaches to select a proper reduced basis for the structural dynamics will be discussed in the following section.

2.2 Reduced Basis for Structural Dynamics

2.2.1 Mode Superposition Method (MSM)

For linear structural dynamics, one of the oldest and conventional MOR techniques is the mode superposition method (MSM) which is also known as the modal truncation. The approach is based on the free vibration modes which will be obtained by solving the undamped eigenvalue expression:

$$\mathbf{M\ddot{u}} + \mathbf{K}|_{eq}\mathbf{u} = \mathbf{0}, \tag{2.6}$$

$$\left(\mathbf{K}|_{eq} - \omega_i^2\mathbf{M}\right)\boldsymbol{\phi}_i = \mathbf{0}, \tag{2.7}$$

where ω_i and ϕ_i are the ith eigenvalue (natural frequency) and corresponding eigenvector, respectively. Moreover, the contribution of the spin-softening effect is considered for the rotating components (i.e., $\mathbf{K}|_{eq} = \partial \mathrm{f}(\mathbf{u})/\,\partial\mathbf{u}|_{u=0} - \mathbf{K}_{sp}$)

The linear reduced basis can be obtained by selecting n_Φ free vibration modes:

$$\mathbf{V} = \left[\boldsymbol{\phi}_1, \boldsymbol{\phi}_2, \ldots, \boldsymbol{\phi}_{n_\Phi}\right], \tag{2.8}$$

Herein, $\boldsymbol{\phi}_{n_\Phi}$ is the eigenvector associated with the nth natural frequency which retains up to approximately twice the highest frequency of interest.

For a linear dynamic system including Rayleigh damping, the reduced-order representation will approximate by a superposition of the modal displacements (Fig. 2.2):

$$\mathbf{u} \approx \sum_{k=1}^{n_\Phi} \boldsymbol{\phi}_k \boldsymbol{\eta}_k = \boldsymbol{\Phi\eta}, \tag{2.9}$$

$$\underbrace{\mathbf{V}^T\mathbf{M}\mathbf{V}}_{\mathbf{I}}\ddot{\boldsymbol{\eta}} + \mathbf{V}^T\mathbf{C}\mathbf{V}\dot{\boldsymbol{\eta}} + \underbrace{\mathbf{V}^T\mathbf{K}|_{eq}\mathbf{V}}_{\boldsymbol{\Lambda}}\boldsymbol{\eta} = \mathbf{V}^T\mathbf{f}^{ext}, \tag{2.10}$$

where $\mathbf{I} \in \mathbb{R}^{n_\Phi \times n_\Phi}$ and $\boldsymbol{\Lambda} = \mathrm{diag}\{\omega_1^2, \omega_2^2, \ldots, \omega_{n_\Phi}^2\} \in \mathbb{R}^{n_\Phi \times n_\Phi}$ are the identity and diagonal eigenvalue matrices, respectively.

In addition, several variants [62-64] of MSM have been developed for the linear structural dynamics (e.g. mode displacement method, mode acceleration correction, and mode truncation augmentation).

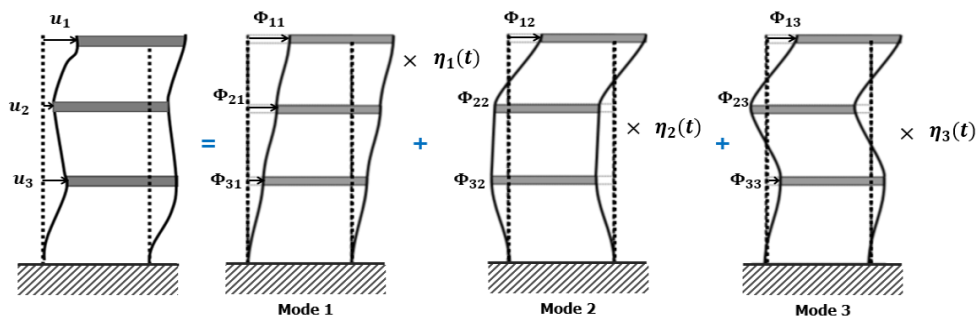

Fig. 2.2 Modal superposition method.

2.2.2 Modal Derivatives

The linear reduced basis comprised of the free-vibration modes, Eq. (2.8), is no longer suitable for approximation of the nonlinear full-order representation. Specifically, the linear basis does not feature the geometric nonlinearity such as the dominant coupling effect between the free vibration modes.

Idelsohn and Cardona [23] suggested the modal derivatives to capture such nonlinear response which is deviated from the linear behavior. Fundamentally, the modal derivatives are the mode shapes derived from the pre-selected free vibration modes. Specifically, the modal derivatives will describe the key deformation shape owing to the finite deflection in the direction of the dominant free vibration modes.

The modal derivatives $\boldsymbol{\Theta}$ are obtained by differentiating the undamped eigenvalue expression with respect to the modal amplitude $\boldsymbol{\eta}$.

$$\left(\mathbf{K}|_{eq} - \omega_i^2\mathbf{M}\right)\left.\frac{\partial \boldsymbol{\phi}_i}{\partial \boldsymbol{\eta}_j}\right|_{eq} + \left(\left.\frac{\partial \mathbf{K}}{\partial \boldsymbol{\eta}_j}\right|_{eq} - \left.\frac{\partial \omega_i^2}{\partial \boldsymbol{\eta}_j}\right|_{eq}\mathbf{M}\right)\boldsymbol{\phi}_i|_{eq} = 0, \quad i,j \in \{1,\dots,n_\Phi\} \tag{2.11}$$

where $\boldsymbol{\theta}_{ij} = \frac{\partial \boldsymbol{\phi}_i}{\partial \boldsymbol{\eta}_j}$ is the derivatives of the ith mode in the jth modal direction. $\frac{\partial \mathbf{K}}{\partial \boldsymbol{\eta}_j}$ is the tangent stiffness matrix evaluated for a displacement $\mathbf{u} = \boldsymbol{\eta}_j\boldsymbol{\phi}_j$, as follows:

$$\left.\frac{\partial \mathbf{K}}{\partial \boldsymbol{\eta}_j}\right|_{eq} = \left.\frac{\partial \mathbf{K}\left(\mathbf{u} = \boldsymbol{\phi}_j\boldsymbol{\eta}_j|_{eq}\right)}{\partial \boldsymbol{\eta}_j}\right|_{eq}. \tag{2.12}$$

To solve Eq. (2.11), an additional constraint will be required as the coefficient

matrix $\left(\mathbf{K}|_{eq} - \omega_i^2\mathbf{M}\right)$ in Eq. (2.11) is singular. Thus, the mass normalization of the free vibration modes regarding the constant mass matrix will be employed as follows:

$$\boldsymbol{\phi}_i{}^T\mathbf{M}\boldsymbol{\theta}_{ij} = 0 \tag{2.13}$$

Generally, the modal derivative computation may incur significant cost because the large-dimensional matrices need to be factorized for each modal derivative. Thus, a cost-effective version of the modal derivatives, usually called as the static modal derivatives [65], was proposed, which was obtained by neglecting the mass term in Eq. (2.11):

$$\boldsymbol{\theta}_{ij} = \left.\frac{\partial\boldsymbol{\phi}_i}{\partial\boldsymbol{\eta}_j}\right|_{eq} = -\mathbf{K}|_{eq}^{-1}\left.\frac{\partial\mathbf{K}\left(\mathbf{u} = \boldsymbol{\phi}_j\boldsymbol{\eta}_j\big|_{eq}\right)}{\partial\boldsymbol{\eta}_j}\right|_{eq}\boldsymbol{\phi}_i, \tag{2.14}$$

Herein, the static modal derivatives are symmetric, which was proved in [65]:

$$\boldsymbol{\theta}_{ij} = \left.\frac{\partial\boldsymbol{\phi}_i}{\partial\boldsymbol{\eta}_j}\right|_{eq} = \left.\frac{\partial\boldsymbol{\phi}_j}{\partial\boldsymbol{\eta}_i}\right|_{eq} = \boldsymbol{\theta}_{ji}. \tag{2.15}$$

These static modal derivatives have been successfully utilized for the geometrically nonlinear multibody dynamics [66, 67].

Figure 2.3 shows an example of the first three free vibration modes and the corresponding static modal derivatives for the flat rectangular plate supported at both ends. It is observed that the vibration modes illustrate the out-of-plane displacement only, whereas the modal derivatives contain the in-plane contribution to capture the geometrically nonlinear coupling effect. Moreover, the symmetry property of the

static modal derivatives is observed as shown in Fig. 2.3 (i.e., $\boldsymbol{\theta}_{12} = \boldsymbol{\theta}_{21}$, $\boldsymbol{\theta}_{13} = \boldsymbol{\theta}_{31}$, and $\boldsymbol{\theta}_{23} = \boldsymbol{\theta}_{32}$).

Hence, when a set of n_Φ free vibration modes are selected, $n_\Phi(n_\Phi + 1)/2$ modal derivatives will be obtained. Consequently, n vectors of the reduced basis $\mathbf{V}$ will correspond to $(3/2 + n_\Phi/2)\, n_\Phi$ basis vectors:

$$\mathbf{V} = \left[\boldsymbol{\phi}_1, \boldsymbol{\phi}_2, \dots, \boldsymbol{\phi}_{n_\Phi}, \boldsymbol{\theta}_{11}, \boldsymbol{\theta}_{12}, \dots, \boldsymbol{\theta}_{n_\Phi n_\Phi}\right], \quad i, j \in \{1, \dots, n_\Phi\} \tag{2.16}$$

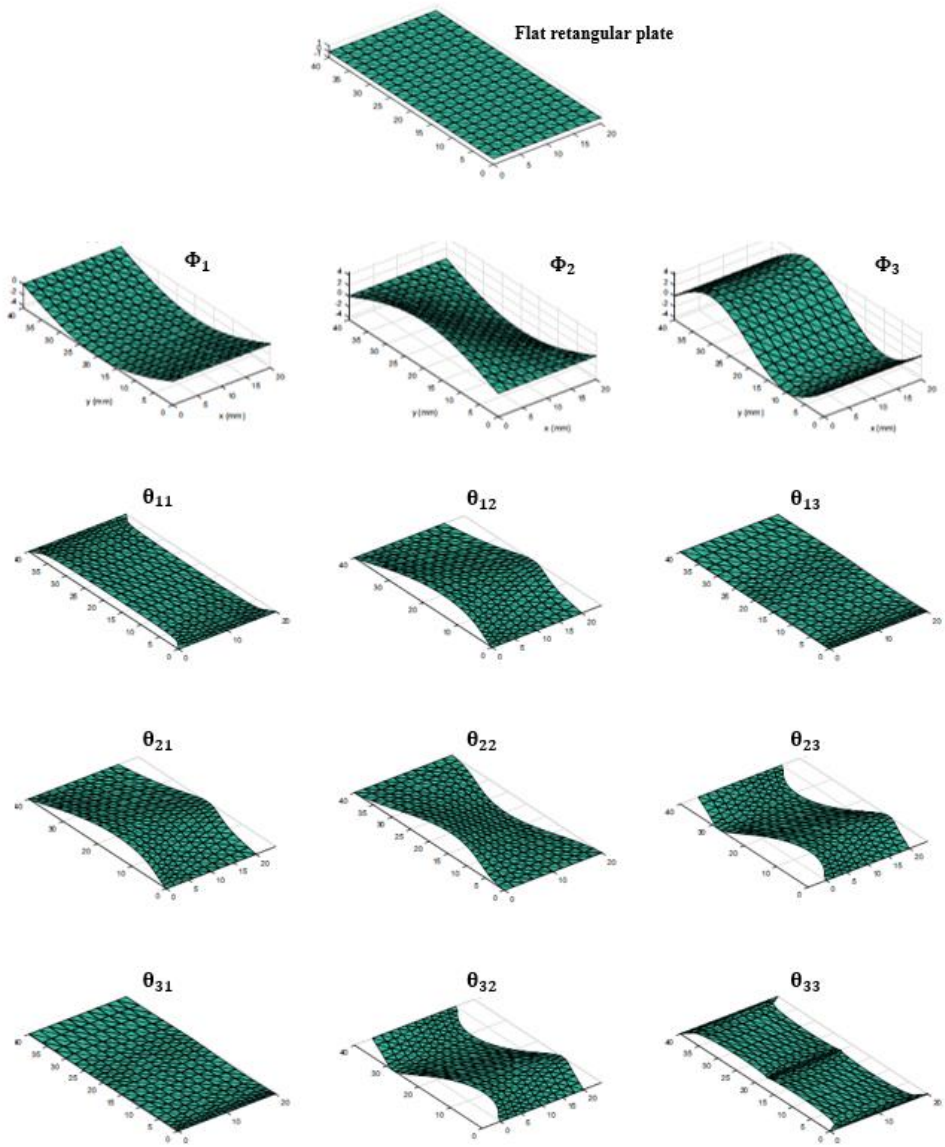

Fig. 2.3 First three free vibration modes and the corresponding static modal derivatives for the flat rectangular plate [65].

2.2.3 Proper Orthogonal Decomposition (POD)

POD formulates an optimal basis required to represent a nonlinear dynamical system. It has been applied to many engineering and scientific systems, including the lower-dimensional dynamics modeling.

In the POD-based MOR framework, a reduced-order representation will be defined based on the precomputed full-order solution, considering the parameter variations, e.g., time-transient displacement response. Those precomputed results are arranged into a so-called snapshot matrix $\mathbf{W}_d \in \mathbb{R}^{N \times N_s}$, where q denotes the discretized state solution obtained by FOM, N the number of DOFs of the full-order representation, S the number of snapshots at each parameter μ, and N_s the total number of snapshots.

$$\mathbf{W}_d = \begin{bmatrix} {q_1}^{(1,1)} & \cdots & {q_1}^{(S_1,1)} & {q_1}^{(1,2)} & \cdots & {q_1}^{(S_2,2)} & {q_1}^{(1,\mu)} & \cdots & {q_1}^{(S_\mu,\mu)} \\ \vdots & \ddots & \vdots & \vdots & \ddots & \vdots & \vdots & \ddots & \vdots \\ {q_N}^{(1,1)} & \cdots & {q_N}^{(S_1,1)} & {q_N}^{(1,2)} & \cdots & {q_N}^{(S_2,2)} & {q_N}^{(1,\mu)} & \cdots & {q_N}^{(S_\mu,\mu)} \end{bmatrix}. \tag{2.17}$$

If the neutral point of the displacement response in time domain is zero, the mean value will be used. Otherwise, it will be composed of an instantaneous fluctuation except for the mean value, as follows:

$$\mathbf{q}(x, \mathrm{t}) = \mathbf{q}_{original}(x, t) - \mathbf{q}_{average}(x). \tag{2.18}$$

The reduced basis **V** will be obtained by implementing the snapshot method [68] or the singular value decomposition (SVD).

In the snapshot method, the eigenvalue expression will be defined. Thus, the average operator is evaluated as a space average over the domain. Then, a temporal-correlation function from the snapshot can be obtained as:

$$\mathbf{C} = \mathbf{W}_d{}^T \mathbf{W}_d. \tag{2.19}$$

In addition, it is possible to formulate an eigenvalue problem to compute the reduced basis.

$$\mathbf{CQ} = \boldsymbol{\lambda}\mathbf{Q}, \tag{2.20}$$

$$\mathbf{V} = [\boldsymbol{\Psi}_1, \boldsymbol{\Psi}_2, \dots, \boldsymbol{\Psi}_n], \tag{2.21}$$

$$\mathbf{V}_i = \frac{1}{\sqrt{\lambda_i}} \mathbf{W}_d \mathbf{Q}_i, \quad i, \in \{1, \dots, n\}, \tag{2.22}$$

where n and $\boldsymbol{\lambda}$ are the selected number of the reduced basis vectors and the energy ratio in the full-order representation, respectively.

When SVD is employed, the snapshot matrix will be decomposed into $\mathbf{W}_d = \boldsymbol{\Psi} \sum \boldsymbol{\Lambda}^{\mathbf{T}}$. Here, $\boldsymbol{\Psi} \in \mathbb{R}^{N \times N_s}$, $\sum = diag(\sigma_1, \dots, \sigma_{N_s})$, and $\boldsymbol{\Lambda}^{\mathbf{T}} \in \mathbb{R}^{N_s \times N}$. The reduced basis vectors **V** are composed of the first *n* column vectors of the left singular matrix $\boldsymbol{\Psi}$ in the resulting SVD.

A suitable number of the basis vectors *n* may be selected based on the ratio between the accumulated and total energies quantified by the singular values, as follows:

$$\text{Energy ratio}(\%) = \frac{\sum_{i=1}^{n} \sigma_i}{\sum_{i=1}^{N_S} \sigma_i} \times 100 \ \geq \ \epsilon_{POD} \ \ (n \ll N) \, . \tag{2.23}$$

The relevant POD procedure is summarized in Algorithm 1.

Algorithm 1 Compute the POD basis

Input: POD basis $\mathbf{T_m} = [\mathbf{t_1}, \dots, \mathbf{t}_m]$

Output: Interpolation indices $\mathbf{p_m} = [\boldsymbol{p_1}, \dots, \boldsymbol{p}_m]$

Procedure POD

Implement SVD of $\mathbf{W}_d = \boldsymbol{\Psi} \sum \boldsymbol{\Lambda}^{\mathbf{T}}$

Select the dimension of POD basis *n*, which is evaluated by Eq. (2.23).

Construct $\mathbf{V}$ by using the selected POD basis vectors $\mathbf{V}_i = [\boldsymbol{\Psi}_1, \dots, \boldsymbol{\Psi}_n]$

It is noted that samples of the snapshot can be collected from the different instances of the parameters so that **V** may not rely on the parameter μ.

2.3 Representation of the Projection-based MOR

2.3.1 Full-order Representation

A reduced-order representation by the reduced basis is presented with a focus on the nonlinear dynamics, especially the time-transient formulation of a rotating component which exhibits large displacement. To achieve it, the relevant full-order representation will be first described in this subsection.

For a nonlinear time-transient formulation, the solution to Eq. (2.1) will be obtained by an implicit generalized-α time integration [69]. The relevant procedure is summarized in Table 1, where α_m, α_f, β, and γ are the algorithm-relevant parameters. The subscripts t and $t+\Delta t$ denote the current and next time step, respectively. When it is written as a non-subscript expression, Δt will denote the size of the time increment.

These nonlinear equations are solved by Newton-Raphson approach, introducing the residual force vector $\mathbf{r}^{k}_{t+\Delta t}$, as follows:

$$\mathbf{r}^{k}_{t+\Delta t} = \mathbf{f}_{ext,t+\Delta t-\alpha_f} - \mathbf{f}_{int}\left(\mathbf{u}^{k}_{t+\Delta t-\alpha_f}\right) - \mathbf{M}\ddot{\mathbf{u}}^{k}_{t+\Delta t-\alpha_m} - \mathbf{C}\dot{\mathbf{u}}^{k}_{t+\Delta t-\alpha_f}, \tag{2.24}$$

$$\left[\frac{1}{\beta\Delta t^2}\mathbf{M} + \frac{\gamma}{\beta\Delta t}\mathbf{C} + (1-\alpha_f)\mathbf{K}\left(\mathbf{u}^{k}_{t+\Delta t}\right)\right]\Delta\mathbf{u}^{k}_{t+\Delta t} = \mathbf{r}^{k}_{t+\Delta t}, \tag{2.25}$$

where the superscript k indicates an iteration index for Newton-Raphson procedure in a single time step, and $\mathbf{K}\left(\mathbf{u}^{k}_{t+\Delta t}\right)$ is the tangent stiffness matrix in terms of the displacement vector.

The updated-Lagrangian (UL) formulation [70] will be employed to consider

geometrical nonlinearity. The local elemental-stiffness matrix $\mathbf{K}^e(\mathbf{u})$ and elemental internal-force vector $\mathbf{f}_{int}^e(\mathbf{u})$, which respectively comprise the global tangent stiffness matrix and internal force vector in Eqs. (2.24) and (2.25), are defined in the deformed (current) configuration, as follows:

$$\mathbf{K}^e(\mathbf{u}) = \int_{\mathbf{v}} \mathbf{B}_L^{\mathrm{T}} \mathbf{C} \mathbf{B}_L \mathrm{dV} + \int_{\mathbf{v}} \mathbf{B}_{NL}^{\mathrm{T}} \boldsymbol{\tau} \mathbf{B}_{NL} \mathrm{dV}, \tag{2.26}$$

$$\mathbf{f}_{int}^e(\mathbf{u}) = \int_{\mathbf{v}} \mathbf{B}_{\mathrm{L}}^{\mathrm{T}} \hat{\boldsymbol{\tau}} \mathrm{dV}, \tag{2.27}$$

where v is the volume of the deformed elements, and $\mathbf{C}$ is the constitutive matrix of the corresponding linear elastic material. $\mathbf{B}_L$ and $\mathbf{B}_{NL}$ are the linear and nonlinear strain-displacement matrices, respectively. $\boldsymbol{\tau}$ and $\hat{\boldsymbol{\tau}}$ are Cauchy (true) stress matrix and vector, respectively. As mentioned previously, all the quantities are derived with respect to the deformed configuration. The stress stiffening effect is included in the second term on the right-hand side, as shown in Eq. (26).

For a rotating structure, the centrifugal force will vary owing to the deformation. When significant axial elongation occurs, a relevant increase in the centrifugal force will become equivalent to a decrease in the stiffness under a constant centrifugal force. In this context, a full-order representation will implement a spin-softening matrix $\mathbf{K}_{sp}$. This will be required to precisely reflect the contribution of the centrifugal-force variation, in accordance with the deformation when the rotational speed is imposed. To consider the contribution of the constant mass, the elemental

spin-softening matrix $\mathbf{K}_{sp}^{e}$ will be defined in the undeformed coordinate, and is expressed as follows [71]:

$$\mathbf{K}_{sp}^{e} = \int_{\mathbf{v}} \rho \mathbf{N}^{\mathrm{T}} \mathbf{\Omega}^{\mathrm{T}} \mathbf{\Omega} \mathbf{N} \mathrm{dV}, \tag{2.28}$$

where V and ρ are the volume and density of the undeformed configuration, respectively. $\mathbf{N}$ and $\mathbf{\Omega}$ are the interpolation and skew-symmetric matrices for the rotational velocity, respectively. Hence, Eqs. (2.24) and (2.25) are substituted with the following equations for the rotating component:

$$\begin{aligned} \mathbf{r}_{\mathrm{t+\Delta t}}^{\mathrm{k}} = \mathbf{f}_{ext,\mathrm{t+\Delta t-\alpha_f}} - \mathbf{f}_{int}\left(\mathbf{u}_{\mathrm{t+\Delta t-\alpha_f}}^{\mathrm{k}}\right) + \left(\mathbf{K}_{sp}\mathbf{u}\right)_{\mathrm{t+\Delta t-\alpha_f}}^{\mathrm{k}} \\ -\mathbf{M}\ddot{\mathbf{u}}_{\mathrm{t+\Delta t-\alpha_m}}^{\mathrm{k}} - \mathbf{C}\dot{\mathbf{u}}_{\mathrm{t+\Delta t-\alpha_f}}^{\mathrm{k}}, \end{aligned} \tag{2.29}$$

where $\left(\mathbf{K}_{sp}\mathbf{u}\right)_{t+\Delta t-\alpha_f}^{k} = \left(1-\alpha_f\right)\mathbf{K}_{sp,t}\mathbf{u}_t + \alpha_f \mathbf{K}_{sp,t+\Delta t}\mathbf{u}_{t+\Delta t}^{k}$ and

$$\left[\frac{1}{\beta \Delta t^2}\mathbf{M} + \frac{\gamma}{\beta \Delta t}\mathbf{C} + \left(1-\alpha_f\right)\left(\mathbf{K}\left(\mathbf{u}_{t+\Delta t}^{k}\right) - \mathbf{K}_{sp,t+\Delta t}\right)\right]\Delta \mathbf{u}_{t+\Delta t}^{k} = \mathbf{r}_{t+\Delta t}^{\mathrm{k}}, \tag{2.30}$$

where $\mathbf{K}_{sp,t}$ and $\mathbf{K}_{sp,t+\Delta t}$ indicate the spin-softening matrices corresponding to the rotational speed for the current and next time step, respectively. The centrifugal force estimated with respect to the undeformed configuration is included as an external force vector in Eq. (2.29).

It is noted that all the sparse global matrices, e.g., $\mathbf{M}$, $\mathbf{C}$, $\mathbf{K}$, $\mathbf{K}_{sp}$, and the sum of the square bracket in Eq. (2.30), can be treated in the symmetric compressed-row

storage (CRS) format. The row and column indices required for the CRS format are efficiently arranged based on the element connectivity, without explicitly generating the dense matrix format. In other words, only the terms related to the elemental connectivity will need to be stored. In most finite-element formulations, the CRS format has shown a better performance than the conventional skyline format, in terms of the storage requirement and equation-solving capability [72]. The CRS format is also capable of exploiting the sparse matrix routines provided by the Intel math kernel library (MKL) [73].

The nonlinear formulation in Eq. (2.30) and the relevant updated solution are expressed as the following simplified linearized expression, using Newton-Raphson approach.

$$\mathbf{K_T}^k\left(\mathbf{u}^k(\mu);\mu\right)\Delta\mathbf{u}(\mu) = \mathbf{r}^k\left(\mathbf{u}^k(\mu);\mu\right), \tag{2.31}$$

$$\mathbf{u}^{k+1}(\mu) = \mathbf{u}^k(\mu) + \Delta\mathbf{u}(\mu) \tag{2.32}$$

where $\mathbf{K_T}$ denotes the tangent stiffness matrix as a square bracket on the left-hand side of Eq. (2.30), and μ denotes an input parameter.

Table 2.1 Generalized-α method for the nonlinear time-transient formulation

1. Equilibrium

$$\mathbf{M}\ddot{\mathbf{u}}_{t+\Delta t-\alpha_m} + \mathbf{C}\dot{\mathbf{u}}_{t+\Delta t-\alpha_f} = \mathbf{f}_{ext,t+\Delta t-\alpha_f} - \mathbf{f}_{int}\left(\mathbf{u}_{t+\Delta t-\alpha_f}\right)$$

2. Time integration

$$\dot{\mathbf{u}}_{t+\Delta t} = \frac{\gamma}{\beta\Delta t}(\mathbf{u}_{t+\Delta t} - \mathbf{u}_t) - \left(\frac{\gamma}{\beta} - 1\right)\dot{\mathbf{u}}_t - \left(\frac{\gamma}{2\beta} - 1\right)\Delta t\ddot{\mathbf{u}}_t$$

$$\ddot{\mathbf{u}}_{t+\Delta t} = \frac{1}{\beta\Delta t^2}(\mathbf{u}_{t+\Delta t} - \mathbf{u}_t) - \frac{1}{\beta\Delta t}\dot{\mathbf{u}}_t - \left(\frac{1}{2\beta} - 1\right)\ddot{\mathbf{u}}_t$$

3. Time average

$$\ddot{\mathbf{u}}_{t+\Delta t-\alpha_m} = (1-\alpha_m)\ddot{\mathbf{u}}_t + \alpha_m\ddot{\mathbf{u}}_{t+\Delta t}$$

$$\dot{\mathbf{u}}_{t+\Delta t-\alpha_f} = (1-\alpha_f)\dot{\mathbf{u}}_t + \alpha_f\dot{\mathbf{u}}_{t+\Delta t}$$

$$\mathbf{u}_{t+\Delta t-\alpha_f} = (1-\alpha_f)\mathbf{u}_t + \alpha_f\mathbf{u}_{t+\Delta t}$$

$$\mathbf{f}_{ext,t+\Delta t-\alpha_f} = (1-\alpha_f)\mathbf{f}_{ext,t} + \alpha_f\mathbf{f}_{ext,t+\Delta t}$$

$$\mathbf{f}_{int}\left(\mathbf{u}_{t+\Delta t-\alpha_f}\right) = (1-\alpha_f)\mathbf{f}_{int}(\mathbf{u}_t) + \alpha_f\mathbf{f}_{int}(\mathbf{u}_{t+\Delta t})$$

2.3.2 Reduced-order Representation

The order reduction via the projection-based MOR procedure converts the full-order representation into an overdetermined equation. Thus, to define ROM, the Galerkin projection approach will be introduced for projecting the nonlinear equations. By applying Galerkin projection to the governing equation, Eq. (2.31), onto a smaller-dimensional subspace, the reconstructed solutions will be approximated into a weighted linear combination of the set of reduced basis vectors.

$$\mathbf{u}(\mu) \approx \underbrace{\mathbf{V}}_{N\times n}\ \underbrace{\boldsymbol{\eta}(\mu)}_{n\times 1} \text{ and } \Delta\mathbf{u}(\mu) \approx \underbrace{\mathbf{V}}_{N\times n}\ \Delta\underbrace{\boldsymbol{\eta}(\mu)}_{n\times 1}, \tag{2.33}$$

While considering Eq. (2.31), the resulting ROM at the iteration step k using Galerkin projection will be expressed as

$$\widehat{\mathbf{K}}_{\mathbf{T}}^{k} = \underbrace{\mathbf{V}^{\mathbf{T}}}_{n\times N}\ \underbrace{\mathbf{K}_{\mathbf{T}}\left(\mathbf{V}\boldsymbol{\eta}^{k}(\mu);\mu\right)}_{N\times N}\ \underbrace{\mathbf{V}}_{N\times n}, \tag{2.34}$$

$$\hat{\mathbf{r}}^{k} = \underbrace{\mathbf{V}^{\mathbf{T}}}_{n\times N}\ \underbrace{\mathbf{r}\left(\mathbf{V}\boldsymbol{\eta}^{k}(\mu);\mu\right)}_{N\times 1}. \tag{2.35}$$

By adopting Newton-Raphson scheme, the updated approximate solution will become as follows:

$$\boldsymbol{\eta}^{k+1}(\mu) = \boldsymbol{\eta}^{k}(\mu) + \Delta\boldsymbol{\eta}(\mu). \tag{2.36}$$

Herein, the increment $\Delta\boldsymbol{\eta} = -\left[\widehat{\mathbf{K}}_{\mathbf{T}}^{k}\right]^{-1}\hat{\mathbf{r}}^{k}$ becomes optimized because it minimizes the discrepancy between the solution by ROM and that by FOM, in terms

of **K**-norm in [74]:

$$\Delta\boldsymbol{\eta} = \arg\min_{\mathbf{z}\in\mathbb{R}^n} \left\| \mathbf{V}\boldsymbol{z} - \left[\mathbf{K}_{\mathbf{T}}^{-1}\,\mathbf{r}\right] \right\|. \tag{2.37}$$

It is noted that the reduced tangent stiffness matrix will become symmetric positive definite.

The projection-based ROM will cause the number of degrees of freedom included in the nonlinear simultaneous equations to be decreased significantly, further reducing the computational cost. Nonetheless, Galerkin projection approach still relies on the full-order representation, as indicated in the matrix and vector multiplication in Eqs. (2.34) and (2.35), respectively. Such operations are required for each Newton-Raphson iteration and time step. Hence, additional relieving manipulation will be needed, with regard to this aspect.

On the other hand, considering the geometric nonlinearities, the resulting internal forces may be explicitly written as a tensorial third-order polynomial in terms of **u** [76] for the linear elastic constitutive law and Green-Lagrange strain tensor:

$$\mathbf{f}_{int}(\mathbf{u}) = {}_2\mathbf{K}\mathbf{u} + {}_3\mathbf{K} : (\mathbf{u}\otimes\mathbf{u}) + {}_4\mathbf{K} \vdots (\mathbf{u}\otimes\mathbf{u}\otimes\mathbf{u}), \tag{2.38}$$

where ${}_2\mathbf{K} \in \mathbb{R}^{N\times N}$, ${}_3\mathbf{K} \in \mathbb{R}^{N\times N\times N}$, and ${}_4\mathbf{K} \in \mathbb{R}^{N\times N\times N\times N}$ are the stiffness tensor coefficients for the linear, quadratic, and cubic internal forces, respectively.

Herein, the number in the left-subscript of each tensor indicates the order of tensors, whereas the symbols $\otimes$, $:$, and $\vdots$ denote the dyadic product, and the double and triple contraction operations, respectively. For example, by using Einstein summation convention, ${}_3\mathbf{A} : {}_2\mathbf{B}$ will yield a vector $\mathbf{c}$ $\left(\text{i.e.}, c_I = {}_3\mathbf{A} :\right.$

$_2\mathbf{B} = A_{Iij}B_{ij}\big)$.

By substituting Eq. (33) into (38), the reduced-order representation will be obtained as follows:

$$\hat{\mathbf{f}}_{int}(\boldsymbol{\eta}) = {}_2\mathbf{Q}\boldsymbol{\eta} + {}_3\mathbf{Q} : (\boldsymbol{\eta} \otimes \boldsymbol{\eta}) + {}_4\mathbf{Q} \vdots (\boldsymbol{\eta} \otimes \boldsymbol{\eta} \otimes \boldsymbol{\eta}), \tag{2.39}$$

where $_2\mathbf{Q} \in \mathbb{R}^{n\times n}$, $_3\mathbf{Q} \in \mathbb{R}^{n\times n\times n}$, and $_4\mathbf{Q} \in \mathbb{R}^{n\times n\times n\times n}$ are the reduced stiffness tensor coefficients for the linear, quadratic, and cubic internal forces, respectively.

Such tensorial approach results in the straightforward computation of the nonlinear terms by introducing a displacement function alone. In particular, pre-computing high-order constant tensors prevents the evaluation and element-wise assemblage of the displacement-dependent nonlinear term at every NR iteration.

However, computing the full-order tensor (third- and fourth-order) would be prohibitive owing to limited computational resources. Therefore, the projection-based MOR technique will be employed to construct reduced tensors. During the off-line stage, the full-order tensor dimension is reduced by projecting the element-level tensor by the selected reduced basis. Accordingly, the online computation time will be significantly reduced, considering that the resulting ROM only relies on the reduced basis dimension by virtue of the explicit tensorial representation.

The detailed derivation of reduced tensors will be described in Chapter 5 which presents DpROM based on the tensorial approach.

Chpater 3

Hyper-reduction approach

3.1 Discrete Empirical Interpolation Method (DEIM)

The hyper-reduction technique is crucial for preventing the time-consuming multiplication in the full-order representation matrices. The larger-dimensional nonlinear terms are approximated to reduce their dimensions. Therefore, the computational cost for Eqs. (2.34) and (2.35) will be substantially diminished, and the relevant reduced-order representation will be defined with regard to the hyper-reduction technique.

DEIM technique allows the residual force vector to be properly approximated as a linearized expression by the independent terms. A column vector $\mathbf{r}(\mathbf{V}\boldsymbol{\eta}(\mu);\mu)$ for an arbitrary $\boldsymbol{\eta}$ can be expressed as an orthogonal expansion, as follows:

$$\mathbf{r}(\mathbf{V}\boldsymbol{\eta}(\mu);\mu) \approx \mathbf{T_m}\mathbf{c}(\mu), \tag{3.1}$$

where $\mathbf{T_m} \in \mathbb{R}^{N\times m}$ represents POD basis, which is obtained by POD procedure (Algorithm 1), based on the snapshots of the residual force vector $\mathbf{W}_f$ during Newton-Raphson iterative computation. The subscript *m* denotes the number of the selected interpolation locations.

As Eq. (3.1) is an overdetermined representation and $\mathbf{T_m}$ is modified by introducing a Boolean matrix **P**,

$$\mathbf{P^T r}(\mathbf{V\eta}(\mu);\mu) = \left(\mathbf{P^T T_m}\right)\mathbf{c}(\mu), \tag{3.2}$$

where **P** is considered as a matrix composed of *m* vectors.

$$\mathbf{P} = \left[\mathbf{e}_{p_1}, \dots, \mathbf{e}_{p_m}\right] \in \mathbb{R}^{N\times m}, \tag{3.3}$$

where $\mathbf{e}_{p_m}$ denotes the $p_m{}^{th}$column of $N \times N$ identity matrix. The coefficients of **c** are obtained by solving Eq. (3.2) and substituting it into Eq. (3.1); the approximated residual force vector is expressed as follows:

$$\mathbf{c}(\mu) = \left(\mathbf{P^T T_m}\right)^{-1}\mathbf{P^T r}(\mathbf{V\eta}(\mu);\mu), \tag{3.4}$$

$$\tilde{\mathbf{r}} \approx \mathbf{T_m c}(\mu) = \underbrace{\mathbf{T_m}\left(\mathbf{P^T T_m}\right)^{-1}}_{N\times m}\underbrace{\mathbf{P^T r}(\mathbf{V\eta}(\mu);\mu)}_{m\times 1}. \tag{3.5}$$

Similar to Eq. (3.5), the tangent matrix is approximated as follows:

$$\tilde{\mathbf{K}}_\mathbf{T} = \underbrace{\mathbf{T_m}\left(\mathbf{P^T T_m}\right)^{-1}}_{N\times m}\underbrace{\mathbf{P^T K_T}(\mathbf{V\eta}(\mu);\mu)}_{m\times N}. \tag{3.6}$$

The approximated nonlinear terms are handled by using only *m* components defined by **P**. The unknown value of **P** can be determined using Algorithm 2. Algorithm 2 provides DEIM basis vector, which contains the interpolation indices and extracts the optimal section of *m* rows, based on POD basis vector $\mathbf{T_m}$.

Algorithm 2 Compute DEIM indices

Input: POD basis $\mathbf{T_m} = [\mathbf{t}_1, \dots, \mathbf{t}_m]$

Output: Interpolation indices $\mathbf{p_m} = [p_1, \dots, p_m]$

procedure DEIM

set $p_1 = maxloc\{\mathbf{t}_1\}$

$\mathbf{T_m} = [\mathbf{t}_1], \mathbf{P} = [\mathbf{e}_{p_1}]$

for k = 2 to m **do**

solve $\mathbf{c} = \left(\mathbf{P^T T_m}\right)^{-1} \mathbf{P^T t}_k$

$\mathbf{w} = \mathbf{t}_k - \mathbf{T_m}\,\mathbf{c}$

$p_k = maxloc\{\mathbf{w}\}$

$\mathbf{T_m} \leftarrow [\mathbf{T_m}\ \mathbf{t}_k], \quad \mathbf{P} \leftarrow [\mathbf{P}\ \mathbf{e}_{p_k}]$

end for

end procedure

By combining DEIM approximation with Galerkin projection, the resulting ROM at an iteration step k will be expressed as follows:

$$\hat{\mathbf{r}}^{k} = \underbrace{\mathbf{V^T T_m}\left(\mathbf{P^T T_m}\right)^{-1}}_{n\times m} \underbrace{\mathbf{P^T r}(\mathbf{V\eta}(\boldsymbol{\mu});\boldsymbol{\mu})}_{m\times 1} = \mathbf{V^T \tilde{r}} \tag{3.7}$$

$$\widehat{\mathbf{K}}_{\mathbf{T}}^{k} = \underbrace{\mathbf{V^T T_m}\left(\mathbf{P^T T_m}\right)^{-1}}_{n\times m} \underbrace{\mathbf{P^T K_T}(\mathbf{V\eta}(\mu);\mu)\mathbf{V}}_{m\times n} = \mathbf{V^T \tilde{K}_T V}\ , \tag{3.8}$$

where, once n and m are selected, the first term $\mathbf{V^T T_m}\left(\mathbf{P^T T_m}\right)^{-1}$ will become an

invariant component; therefore, it will be determined in the off-line phase.

In contrast to the approach of solely applying Galerkin projection, i.e., Eqs. (2.34) and (2.35), it will be noted that $\mathbf{K_T}$ and $\mathbf{r}$ in Eqs. (3.7) and (3.8) are not explicitly generated during the iterative procedure. Instead, the row-reduced matrix $\mathbf{P^T K_T}$ and vector $\mathbf{P^T r}$ are directly applied, which will enable the algorithm to become more efficient by avoiding the assemblage of matrices and vector entries, specifically preventing the selection of irrelevant rows. $\mathbf{P^T K_T}$ and the other reduced-sized matrices for generating $\mathbf{P^T r}$, e.g., $\mathbf{P^T M}$ and $\mathbf{P^T C}$, are also the sparse matrices. As those matrices are treated in the non-symmetric CRS manipulation, multiplication with the other matrices and vectors will be needed infrequently, in proportion to the sparsity of the matrix.

3.2 Gauss-Newton with Approximated Tensors (GNAT)

As expressed in Eq. (2.37), an optimal solution for the projection-based ROM is obtained, such that the discrepancy between ROM and FOM may be minimized when the tangent stiffness matrix is symmetric. In DEIM, however, the approximated tangent matrix $\widetilde{\mathbf{K}}_{\mathbf{T}}$ is no longer guaranteed to be symmetric [37, 74]. Consequently, the matrices reduced by Galerkin projection in DEIM approach may often lead to inappropriate solution.

As an alternative combination with Galerkin projection, GNAT will mitigate the drawback mentioned in the previous paragraph by solving it using a nonlinear least-squares approach, e.g., Gauss-Newton method.

$$\Delta\boldsymbol{\eta} = \arg\min_{\mathbf{z}\in\mathbb{R}^n} \left\| \widehat{\mathbf{K}}_{\mathbf{T}}(\mathbf{V}\boldsymbol{\eta}(\mu);\mu)\mathbf{z} - \hat{\mathbf{r}}(\mathbf{V}\boldsymbol{\eta}(\mu);\mu) \right\|_2. \tag{3.9}$$

In GNAT, using DEIM approximation for the nonlinear terms, the resulting ROM at the k^{th} iteration step will be expressed as

$$\hat{\mathbf{r}}^k = \underbrace{\left(\mathbf{P}^{\mathbf{T}}\mathbf{T}_{\mathbf{m}}\right)^{-1}}_{m\times m} \underbrace{\mathbf{P}^{\mathbf{T}}\mathbf{r}(\mathbf{V}\boldsymbol{\eta}(\mu);\mu)}_{m\times 1}, \tag{3.10}$$

$$\widehat{\mathbf{K}}_{\mathbf{T}}^k = \underbrace{\left(\mathbf{P}^{\mathbf{T}}\mathbf{T}_{\mathbf{m}}\right)^{-1}}_{m\times m} \underbrace{\mathbf{P}^{\mathbf{T}}\mathbf{K}_{\mathbf{T}}(\mathbf{V}\boldsymbol{\eta}(\mu);\mu)\mathbf{V}}_{m\times n}. \tag{3.11}$$

The relevant updated approximate solution will result in the following.

$$\Delta\boldsymbol{\eta} = \arg\min_{\mathbf{z}\in\mathbb{R}^n} \left\| \left(\mathbf{P}^{\mathbf{T}}\mathbf{T}_{\mathbf{m}}\right)^{-1}\mathbf{P}^{\mathbf{T}}\mathbf{K}_{\mathbf{T}}(\mathbf{V}\boldsymbol{\eta}(\mu);\mu)\mathbf{V}\boldsymbol{z} - \left(\mathbf{P}^{\mathbf{T}}\mathbf{T}_{\mathbf{m}}\right)^{-1}\mathbf{P}^{\mathbf{T}}\mathbf{r}(\mathbf{V}\boldsymbol{\eta}(\mu);\mu) \right\|_2, \tag{3.12}$$

where † denotes Moore-Penrose pseudo-inverse.

Figure 3.1 presents the computational algorithm for DEIM and GNAT, in which the relevant equations are distinguished between DEIM (green) and GNAT (red). In the off-line stage, the full-order representation is used to solve the range of appropriately selected parameters. For the various parameters, the displacement results $\mathbf{u}(\mu_i)$ and the residual force vector $\mathbf{r}\left(\mathbf{u}^k(\mu_i);\mu_i\right), i = 1, \dots, n_s$, are stored in the snapshot matrices $\mathbf{W}_d$ and $\mathbf{W}_f$, respectively. The former is stored at each time step, and the latter at each Newton-Raphson iteration k. Subsequently, the reduced bases $\mathbf{V}$ and $\mathbf{T}_{\mathbf{m}}$ for Galerkin projection and DEIM approximation are respectively extracted.

Next, DEIM algorithm is employed to compute the interpolation location for $\mathbf{T}_{\mathbf{m}}$ and define the reduced meshes. Finally, the off-line terms are required during the online stage, and the online stage is executed. The nonlinear time-transient analysis requires only the assemblage of the reduced meshes and the solution of the smaller-dimensional representation at each iterative procedure.

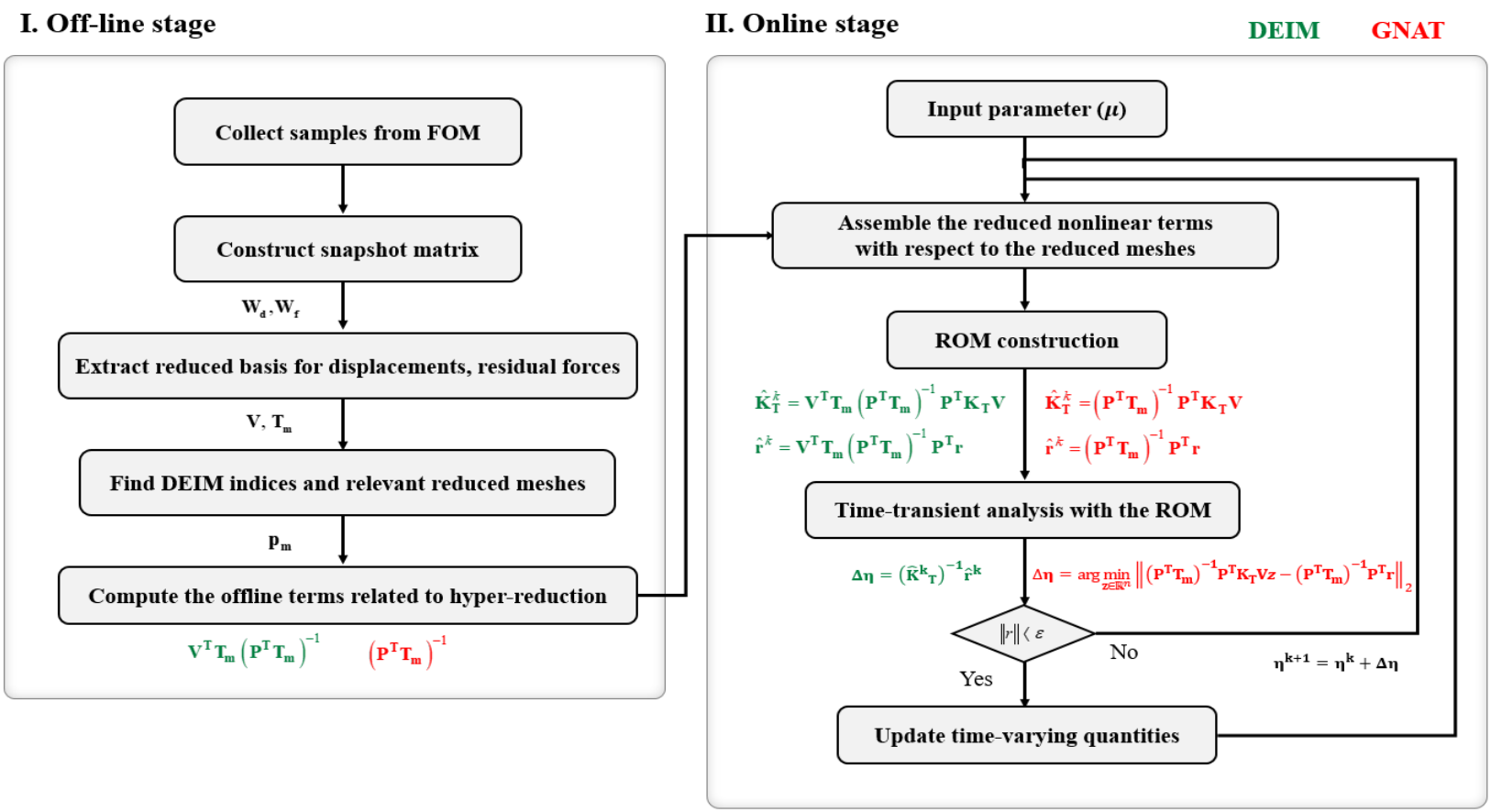

Fig. 3.1 Computational algorithm for DEIM and GNAT

3.3 Energy-Conserving Sampling and Weighting (ECSW)

Unlike in DEIM and GNAT, the projected Galerkin nonlinear terms can be directly approximated in ECSW. A subset of elements $\tilde{\mathbf{E}}$ in a finite element mesh ($|\tilde{\mathbf{E}}| \ll N_e$) is used to approximate only the reduced nonlinear terms that are related to the selected element level. Specifically, ECSW conserves the virtual work (energy) done by the internal force vector $\mathbf{f}_{int}$ or tangent stiffness matrix $\mathbf{K_T}$, along the set of the reduced basis $\mathbf{V}$ on the reduced FE mesh. Consequently, the approximated tangent stiffness matrix is guaranteed to be symmetric, and the resulting ROM can be constructed without losing the numerical stability of the full-order representation [48].

For an FE-based dynamical system with N_e the total number of elements, the reduced internal force vector $\hat{\mathbf{f}}_{int}$ at the k^{th} iteration step will be expressed as the summation over the selected elements:

$$\hat{\mathbf{f}}_{int}^{k} = \sum_{e=1}^{N_e} \mathbf{V}^{eT} \mathbf{f}_{int}^{e}(\mathbf{V}^{e}\boldsymbol{\eta}(\mu);\mu) \approx \sum_{e\in\tilde{\mathbf{E}}} W_e \mathbf{V}^{eT} \mathbf{f}_{int}^{e}(\mathbf{V}^{e}\boldsymbol{\eta}(\mu);\mu), \tag{3.13}$$

where $W_e \in \mathbb{R}^{N_e}$ is the weights of element e used to provide the optimal approximation of the reduced nonlinear term.

Similar to Eq. (3.13), the reduced tangent stiffness matrix can be approximated as follows:

$$\widehat{\mathbf{K}}_{\mathbf{T}}^{k} = \sum_{e=1}^{N_e} \mathbf{V}^{eT} \mathbf{K}_{T}^{e}(\mathbf{V}^{e}\boldsymbol{\eta}(\mu);\mu)\mathbf{V}^{e} \approx \sum_{e\in\tilde{\mathbf{E}}} W_e \mathbf{V}^{eT} \mathbf{K}_{T}^{e}(\mathbf{V}^{e}\boldsymbol{\eta}(\mu);\mu)\mathbf{V}^{e}. \tag{3.14}$$

It is noted that this procedure is analogous to Gaussian quadrature method in which a certain integral is approximated by the integral function evaluation at specified points and then weighted by pre-defined weighting factors.

The elements and weights can be determined from the training dataset specified by the displacement results, using the snapshot matrix with N_s number of time steps). The relevant training dataset can then be computed using the least-squares approach as follows:

$$\boldsymbol{\tau}^{(i)} = \left(\mathbf{V}^{\mathbf{T}}\mathbf{V}\right)^{-\mathbf{1}}\mathbf{V}^{\mathbf{T}}\mathbf{u}^{(i)}, \tag{3.15}$$

where the superscript i indicates the i^{th} training vector in the training data set.

For each of the training vectors, the element-level contribution of the projected internal force can be assembled into a matrix **G** and vector **b** as follows:

$$\mathbf{G} = \begin{bmatrix} \mathbf{g}_{11} & \cdots & \mathbf{g}_{1N_e} \\ \vdots & \ddots & \vdots \\ \mathbf{g}_{N_s1} & \cdots & \mathbf{g}_{N_sN_e} \end{bmatrix} \in \mathbb{R}^{nN_s \times N_e}, \qquad \mathbf{b} = \begin{bmatrix} \mathbf{b}_1 \\ \vdots \\ \mathbf{b}_{N_s} \end{bmatrix} \in \mathbb{R}^{nN_s}, \tag{3.16}$$

where $\mathbf{g}_{ie} = \mathbf{V}_e^{\mathbf{T}}\mathbf{f}_{int}^{e}(\mathbf{V}_e\boldsymbol{\tau}^{(i)}) \in \mathbb{R}^n$ and $\mathbf{b}_i = \sum_{e=1}^{N_e}\mathbf{g}_{ie} \in \mathbb{R}^n$ represent the elemental reduced nonlinear internal force vector and their element-wise summation evaluated at the i^{th} training vector, respectively.

The unknown element weights $\mathbf{W}$ and the subset of relevant elements $\tilde{\mathbf{E}}$ are obtained by solving a sparse non-negative least-squares (NNLS) problem [47] as follows:

$$\mathbf{W} = \arg\min_{\widetilde{W}\epsilon\mathbb{R}^{N_e},\widetilde{W}\geq 0}\left\|\mathbf{G}\widetilde{\mathbf{W}} - \mathbf{b}\right\|_2 \leq \epsilon_{nnls}\|\mathbf{b}\|_2\,, \tag{3.17}$$

where $\widetilde{\mathbf{W}}$ and $\mathbf{W} = [W_1, W_2, \dots, W_{N_e}] \in \mathbb{R}^{N_e}$ are the sparse vector and set of positive weights associated with each element, respectively. $\epsilon_{nnls} \in [0, 1]$ denotes a training tolerance for controlling the sparsity of $\widetilde{\mathbf{W}}$.

The relevant sparse NNLS procedure for ECSW is summarized as Algorithm 3.

Algorithm 3 Compute the sparse NNLS for ECSW

Input: $\mathbf{G}$, $\mathbf{b}$, ϵ_{nnls}

Output: element weight $\mathbf{W} \in \mathbb{R}^{N_e}$, selected elements $\tilde{\mathbf{E}} \subset \{1, \dots, N_e\}$

procedure NNLS

$\tilde{\mathbf{E}} = \mathbf{null}$, $\mathbf{Z} = \{1, \dots, N_e\}$, $\mathbf{W} = \mathbf{0}$, $\mathbf{f}_{int}^{\mathbf{NNLS}} = \mathbf{b}$

while $\|\mathbf{R}\|_2 < \epsilon_{nnls}\|\mathbf{b}\|_2$ **do**

$p = maxloc\{\mathbf{G}^{\boldsymbol{T}}\mathbf{f}_{int}\}$

$\tilde{\mathbf{E}} \leftarrow \tilde{\mathbf{E}} \cup \{p\}$, $\mathbf{Z} \leftarrow \mathbf{Z} \backslash \{p\}$

loop

solve $\boldsymbol{\zeta}_{\tilde{\mathbf{E}}} = \mathbf{G}_{\tilde{\mathbf{E}}}^{\dagger}\mathbf{b}$

$\boldsymbol{\zeta}_{\mathbf{Z}} = \mathbf{0}$

if $\boldsymbol{\zeta}_{\tilde{\mathbf{E}}} > \mathbf{0}$ **then**

$\mathbf{W} = \boldsymbol{\zeta}$

break

end if

$\alpha = min\{W_k / (W_k - \zeta_k) \mid \zeta_k \leq 0,\ k \in \tilde{\mathbf{E}}\}$

$\mathbf{W} \leftarrow \mathbf{W} + \alpha(\boldsymbol{\zeta} - \mathbf{W})$

$\tilde{\mathbf{E}} \leftarrow \tilde{\mathbf{E}} \cup \{k \mid W_k = 0\}$, $\mathbf{Z} \leftarrow \mathbf{Z} \backslash \{k \mid W_k = 0\}$

end loop

$\mathbf{f}_{int}^{\mathbf{NNLS}} = \mathbf{b} - \mathbf{G}_{\tilde{\mathbf{E}}}^{T}\mathbf{W}_{\tilde{\mathbf{E}}}$

end while

end procedure

3.4 Quadratic Manifold-based ECSW

As mentioned earlier, it is necessary to generate the training dataset (snapshots) for sampling the elements in ECSW, which would comprise the full-order time-varying displacement results. However, these numerous full-order simulations result in a computationally expensive off-line stage.

Jain [51] suggested the QM-based reduction approach to collect the training set for ECSW in an inexpensive manner. In this approach, the full-order nonlinear time-transient solution (t) is obtained by nonlinearly mapping the inexpensive reduced linear solution $\mathbf{q}(t)$, without the nonlinear FOM simulation:

$$\mathbf{u}(\mathrm{t}) \approx \boldsymbol{\Gamma}\big(\mathbf{q}(\mathrm{t})\big), \tag{3.18}$$

where $\boldsymbol{\Gamma} : \mathbb{R}^n \to \mathbb{R}^N$ is the nonlinear mapping function.

The relevant reduced linear solution is usually obtained via the mode superposition method. For a linear dynamic system with Rayleigh damping, the reduced-order representation by the selected n_Φ free vibration modes is expressed as follows:

$$\underbrace{\boldsymbol{\Phi}^T\mathbf{M}\boldsymbol{\Phi}}_{\mathbf{I}}\ddot{\mathbf{q}}(t) + \boldsymbol{\Phi}^T\mathbf{C}\boldsymbol{\Phi}\dot{\mathbf{q}}(t) + \underbrace{\boldsymbol{\Phi}^T\mathbf{K}|_{eq}\boldsymbol{\Phi}}_{\boldsymbol{\Lambda}}\mathbf{q}(t) = \boldsymbol{\Phi}^T\mathbf{f}_{ext}(t), \tag{3.19}$$

$$\mathbf{u}_{lin}(\mathrm{t}) = \boldsymbol{\Phi}\mathbf{q}(t), \tag{3.20}$$

where $\mathbf{I} \in \mathbb{R}^{n_\Phi \times n_\Phi}$ and $\boldsymbol{\Lambda} = \mathrm{diag}\{\omega_1^2, \omega_2^2, \dots, \omega_{n_\Phi}^2\} \in \mathbb{R}^{n_\Phi \times n_\Phi}$ are the identity and diagonal eigenvalue matrices, respectively. $\boldsymbol{\Phi} \in \mathbb{R}^{N \times n_\Phi}$ and $\mathbf{q}(t) \in \mathbb{R}^{n_\Phi}$ are the linear reduced basis comprising the selected free vibration modes and the

resulting time-varying displacement vector in terms of the reduced coordinate, respectively.

Then, the nonlinear mapping $\mathbf{\Gamma}(\mathbf{q}(\mathrm{t}))$ is defined as a quadratic function, which is referred to as QM:

$$\mathbf{u}(\mathrm{t}) \approx \mathbf{\Gamma}(\mathbf{q}(\mathrm{t})) := \mathbf{\Phi}\mathbf{q}(t) + \frac{1}{2}\mathbf{\Omega} : (\mathbf{q}(t) \otimes \mathbf{q}(t)), \tag{3.21}$$

where $\mathbf{\Omega} \in \mathbb{R}^{N \times n_\Phi \times n_\Phi}$ is the quadratic component composed of static modal derivatives derived from the free vibration modes, which helps reflect the geometrically nonlinear (second-order) effects, as shown in Fig. 3.2.

It is noted that the free vibration modes and associated modal derivatives in Eq. (3.21) are pre-computed basis vectors used to construct the reduced-order representation in the projection-based MOR. Algorithm 4 summarizes the relevant computational procedure of ECSW, including QM-based training set generating.

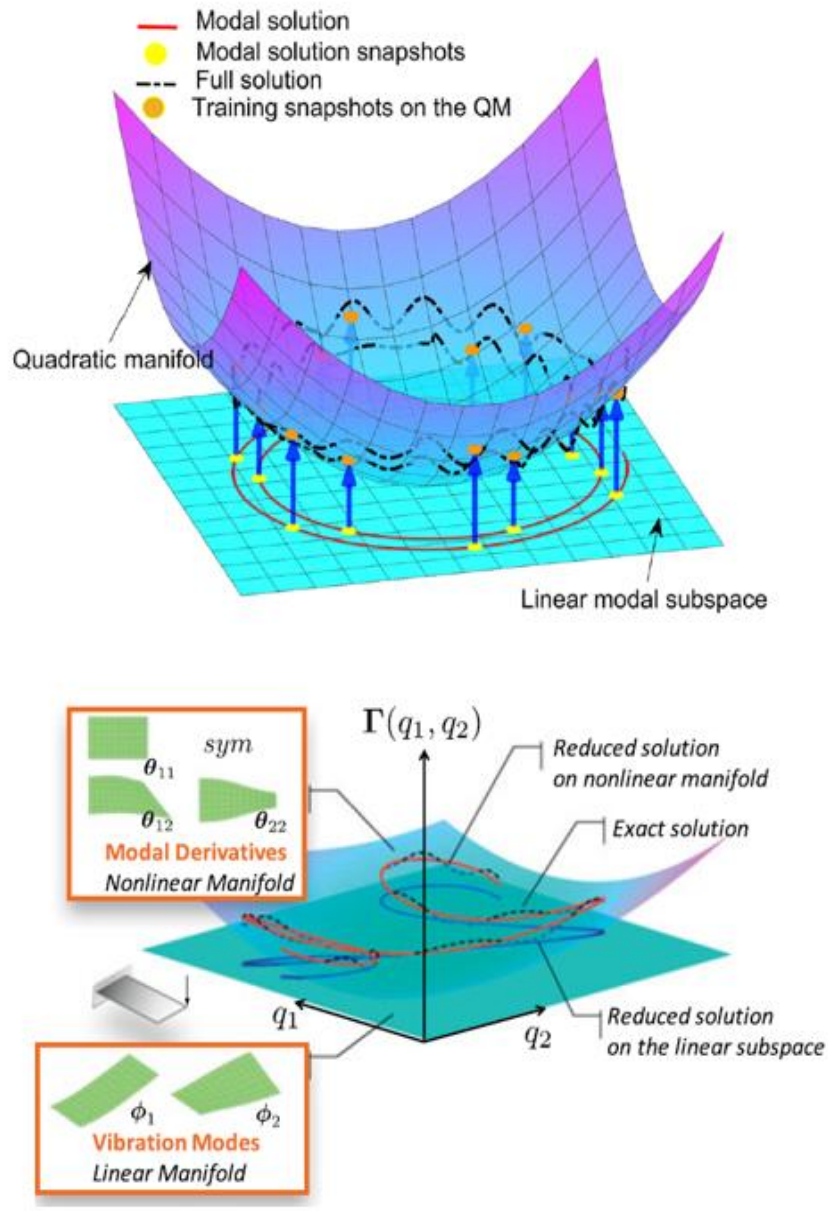

Fig. 3.2 Schematic of the QM-based training set generation [51, 75].

Algorithm 4 ECSW including QM-based training set generation

Input: free vibration modes $\mathbf{\Phi} \in \mathbb{R}^{N \times n_\Phi}$, static modal derivatives $\mathbf{\Theta} \in \mathbb{R}^{N \times \frac{n_\Phi (n_\Phi + 1)}{2}}$, ϵ_{nnls}, nominal FE representation (Eq. (2.1))

Output: element weight $\mathbf{W} \in \mathbb{R}^{N_e}$, selected elements $\tilde{\mathbf{E}} \subset \{1, \dots, N_e\}$

procedure QM-based ECSW

<Generation of the training data set>

$\mathbf{\Omega} \leftarrow$ *third-order null tensor* $\in \mathbb{R}^{N \times n_\Phi \times n_\Phi}$

for $j = 1$ to n_Φ **do**

  for $i = 1$ to n_Φ **do**

    $\mathbf{\Omega}_{kij} = (\boldsymbol{\theta}_{ij})_k,\ k \in \{1, \dots, N\}$

    if $i \neq j$ **then**

      $\mathbf{\Omega}_{kij} = \left(\boldsymbol{\theta}_{ji}\right)_k$

    endif

  end for

end for

Define QM: $\mathbf{\Gamma}\left(\mathbf{q}(t)\right)$, Eq. (3.21)

Compute $\mathbf{q}(\mathrm{t})$ using Eq. (3.19)

for $i = 1$ to N_s **do**

  Compute $\mathbf{u}^{(i)} = \mathbf{\Gamma}\left(\mathbf{q}(t_i)\right)$

  Compute $\boldsymbol{\tau}^{(i)} = \left(\mathbf{V^T V}\right)^{-1} \mathbf{V^T u}^{(i)}$

end for

<Sampling of the elements and associated weights>

Assemble **G** and **b** using Eq. (3.16)

Acquire $\mathbf{W}$ and $\tilde{\mathbf{E}}$ by solving the sparse NNLS problem (Algorithm 3)

end procedure

Chpater 4

Evaluation on Hyper Reduced-order Model

4.1 POD-based MOR including Hyper-reduction

As mention in the previous chapter, the hyper-reduction approaches, DEIM, GNAT, and ECSW, can alleviate such computational bottleneck, allowing the reconstruction of the nonlinear term in the reduced dimension by using either a few sampling points or a reduced number of meshes. As a result, the computational cost for constructing the reduced-order representation will be decreased significantly by using the reduced nonlinear term during the recursive projection. Such hyper-reduction-based ROMs have been applied to numerous engineering fields.

However, a thorough comparison of the aforementioned hyper-reduction-based ROMs has not been reported, specifically those related to the geometrically nonlinear structural dynamics. Therefore, the parameterized POD-based MOR framework that includes hyper-reduction approach will be developed and systematically evaluated for the resulting ones regarding the prediction capability for the nonlinear formulations accurately and fast. To achieve this goal, a full-order representation is developed to provide a set of samples over a range of selected parameters. A nonlinear structural analysis, based on the updated Lagrangian formulation, is developed and applied to rotating components undergoing large displacements. The variation in their dynamic characteristics, owing to the rotation

effect, is included in the updated Lagrangian formulation. Then, POD-based ROMs combined with the hyper-reduction technique are developed to construct a reduced-order representation. The relevant reduced nonlinear terms are approximated using DEIM, GNAT, and ECSW approaches. The resulting ROMs are applied to the structural dynamics of a propeller blade, including geometric nonlinear parametric variations. Finally, the obtained results are compared to those obtained using the other ROM approaches, in terms of accuracy, stability, and computational efficiency.

Figure 4.1 illustrates the POD-based ROM framework, including the hyper-reduction approach. In the off-line stage, a sampling analysis is carried out using the full-order representation, and the reduced basis is extracted from these results. In the online stage, the ROM is defined by assembling the reduced basis and the nonlinear terms at each iteration step. Herein, the hyper-reduction technique is employed to overcome the computational bottleneck due to the recursive computation.

The mathematical expressions for the relevant ROMs are summarized in Table 4.1

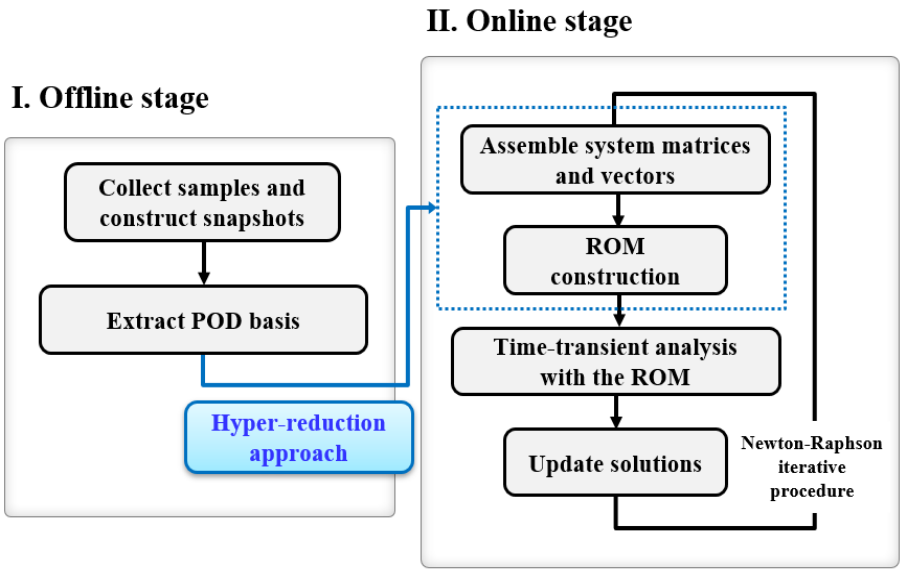

Fig. 4.1 General POD-based framework, including the hyper-reduction.

Table 4.1 Comparison of the reduced nonlinear terms between the POD-based ROMs

	Reduced nonlinear terms (at k^{th} iteration)
POD	$\hat{\mathbf{K}}_{\mathbf{T}}^{k} = \mathbf{V}^{\mathbf{T}}\mathbf{K}_{\mathbf{T}}\mathbf{V}$ $\hat{\mathbf{r}}^{k} = \mathbf{V}^{\mathbf{T}}\mathbf{r}$
POD-DEIM	$\hat{\mathbf{K}}_{\mathbf{T}}^{k} = \mathbf{V}^{\mathbf{T}}\mathbf{T}_{\mathbf{m}}(\mathbf{P}^{\mathbf{T}}\mathbf{T}_{\mathbf{m}})^{-1}\mathbf{P}^{\mathbf{T}}\mathbf{K}_{\mathbf{T}}\mathbf{V}$ $\hat{\mathbf{r}}^{k} = \mathbf{V}^{\mathbf{T}}\mathbf{T}_{\mathbf{m}}(\mathbf{P}^{\mathbf{T}}\mathbf{T}_{\mathbf{m}})^{-1}\mathbf{P}^{\mathbf{T}}\mathbf{r}$
POD-GNAT	$\hat{\mathbf{K}}_{\mathbf{T}}^{k} = (\mathbf{P}^{\mathbf{T}}\mathbf{T}_{\mathbf{m}})^{\dagger}\mathbf{P}^{\mathbf{T}}\mathbf{K}_{\mathbf{T}}\mathbf{V}$ $\hat{\mathbf{r}}^{k} = (\mathbf{P}^{\mathbf{T}}\mathbf{T}_{\mathbf{m}})^{\dagger}\mathbf{P}^{\mathbf{T}}\mathbf{r}$
POD-ECSW	$\hat{\mathbf{K}}_{\mathbf{T}}^{k} = \sum_{e\in\tilde{\mathbf{E}}} W_e \mathbf{V}^{eT}\mathbf{K}_{T}^{e}\mathbf{V}^{e}$ $\hat{\mathbf{r}}^{k} = \sum_{e\in\tilde{\mathbf{E}}} W_e \mathbf{V}^{eT}\mathbf{r}^{e}$

4.2 Numerical Results

A nonlinear time-transient analysis is performed based on the proposed framework, and its validation is presented in this section. The numerical example is the 54H60 propeller blade, which is mainly installed on the C-130 or P-3 aircraft. It has a slender configuration with a twisted surface and a high aspect ratio. The relevant configuration and analysis conditions are shown in Fig. 4.2. The three-dimensional propeller-blade configuration is discretized by ten-node tetrahedral elements (5,903 nodes with 17,709 degrees of freedom). The base surface of the blade is clamped, and harmonic excitation is applied to all the nodes of the top surface. The relevant amplitude of the excitation is chosen to be 500 N. Moreover, to investigate the geometrically nonlinear behavior involving large displacements, the blade is excited at a frequency of 150 $\mathrm{rad/s}$, which corresponds to the first bending mode. Point A, α_e, and ω_e represent the nodes showing the maximal displacement, excitation load, and frequency factor, respectively.

To examine the performance of the parametric variations, three parameters (μ_1, μ_2, μ_3), i.e., Young's modulus $E = \mu_1$ GPa ($\mu_1 \in [70, 75]$), density $\rho = \mu_2$ kg/m^3 ($\mu_2 \in [2{,}500, 3{,}000]$), and constant rotational velocity $\Omega = \mu_3$ rpm ($\mu_3 \in [1{,}000, 1{,}500]$), are utilized. Eight relevant training points (red circles) are selected at the upper and lower bounds (Fig. 4.3), and four test cases (green triangles) with different variables are randomly selected to investigate the performance of the parametric variation. The material properties are assumed to correspond to 7,000-series aluminum alloys with a 1% damping ratio [77]. An

inertial Rayleigh damping is considered for the structural viscous damping, $\mathbf{C} = \beta_m \mathbf{M}$, where β_m denotes the coefficient for Rayleigh damping.

To validate the present full-order representation, a time-transient analysis is conducted for up to 0.2 s (200 steps) for Case 1 ($\alpha_e = 1.0,\ \omega_e = 1.0$). These results are validated using the ANSYS commercial simulation software [78]. Figure 4.4-a shows a comparison of the tip-displacement history between ANSYS and the FOM. The FOM results show good agreement with those obtained using ANSYS. Considerable differences are found when comparing the linear and nonlinear analysis results. The geometrically nonlinear results show that the maximum response and resonant frequency are different, when compared with those of the linear analysis results (Fig. 4.4-b). Hence, the geometric nonlinearity may significantly influence the dynamic property prediction of the blade, and it should also be included in the reduced-order representation.

To construct the reduced-order representation, a sampling analysis using the full-order representation is conducted at the upper and lower bounds of the eight training points. A nonlinear transient solution is obtained over 200 steps. Moreover, 1,600 and 7,806 snapshots are collected from the displacements (at each time step) and residual force vectors (at each iteration), respectively. The sampling procedures are summarized in Table 4.2. Subsequently, the POD and DEIM bases are extracted from the snapshots and used for the successive comparison of ROMs.

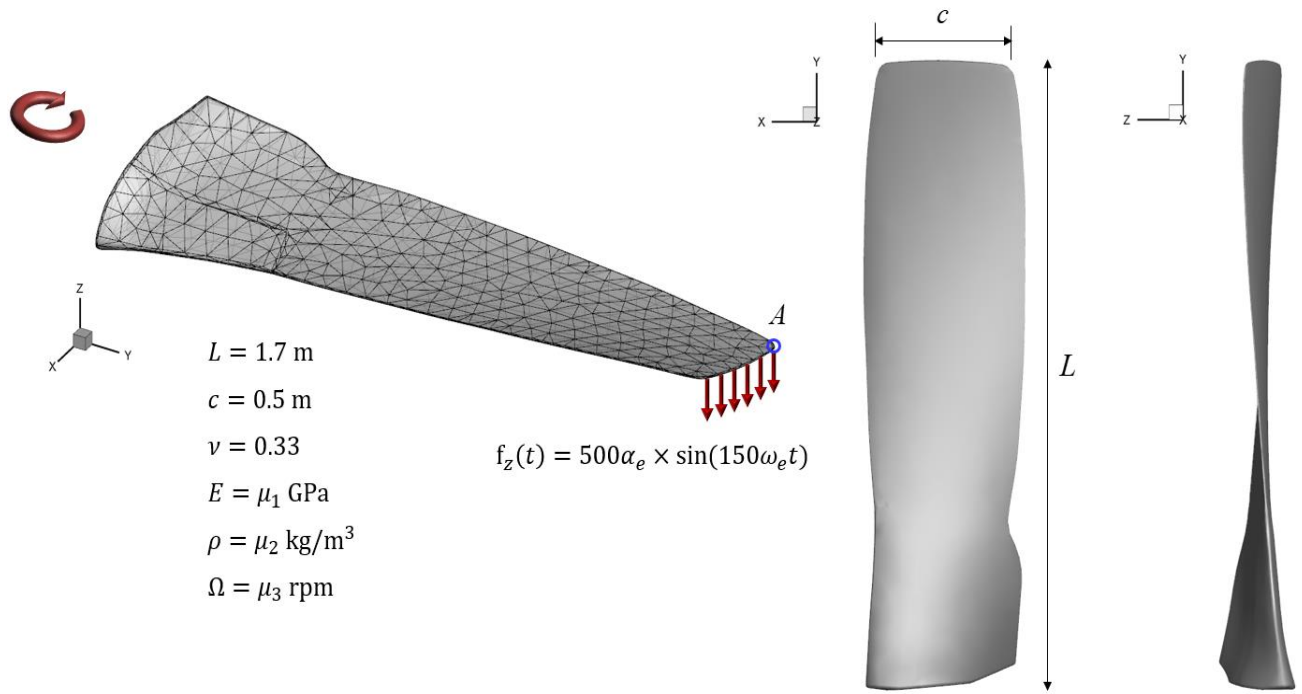

Fig. 4.2 Configuration and analysis conditions for a 54H60 propeller blade.

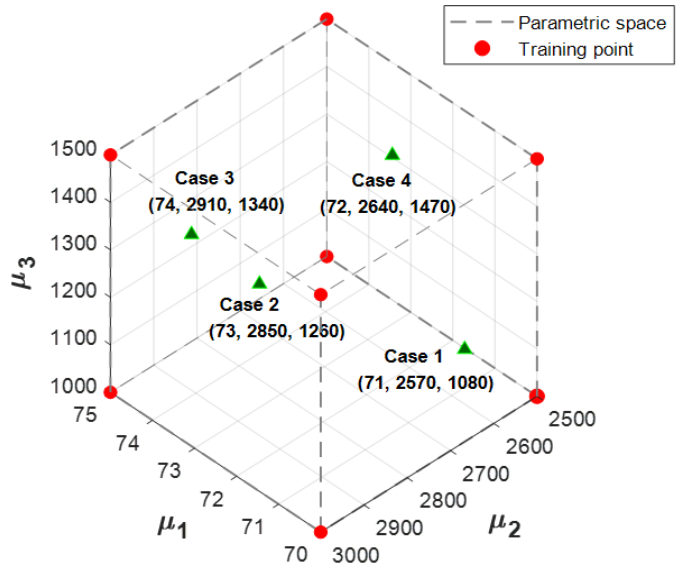

Fig. 4.3 Eight training points and four test cases for the parametric variations.

Table 4.2 Sampling analysis results for extracting the reduced basis

No. of training points	Sampling time	Time-step size (Δt)	No. of snapshots	
			Displacements	Residual force
8	0-0.2s (200 time steps)	0.001s	1,600	7,806

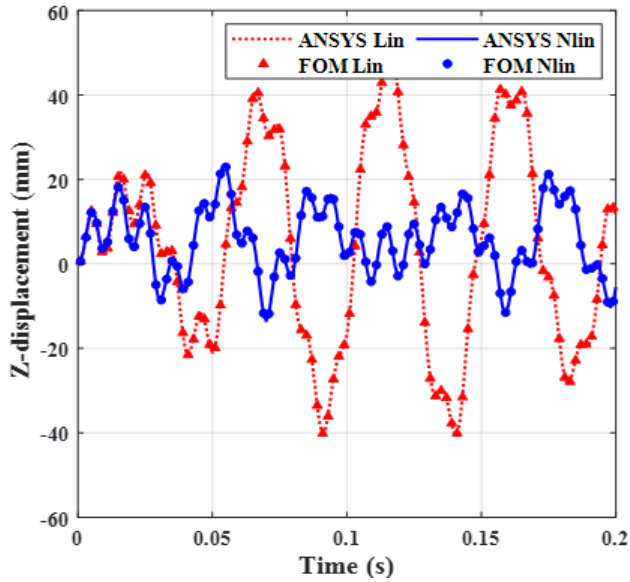

(a) Time domain

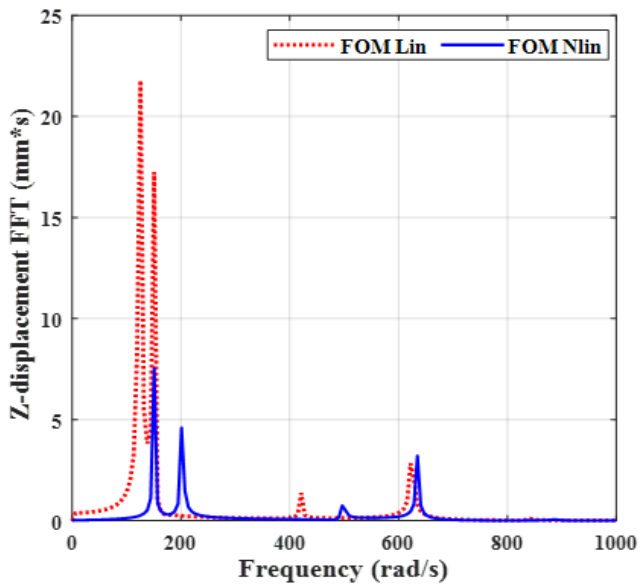

(b) Frequency domain

Fig. 4.4 Comparison of the displacement history at Point A between ANSYS and FOM

4.2.1 Accuracy Factor

The accuracy of the present ROMs, namely POD, POD-DEIM, POD-GNAT, and POD-ECSW, is evaluated using five accuracy factors proposed based on different levels of interest. Each factor e_i is the normalized value, which varies from 0 to 1 through comparisons with the solutions obtained from the full- and reduced-order representations; the closer the value is to 1, the better is its accuracy. Negative factor values are set to 0 while computing the accuracy factor. Several factors (e_1, e_4, and e_5) are cited from Ref. [31].

i. Relative discrepancy of the energy

$$e_1 = \max\left(0, \quad 1 - \frac{\sqrt{\sum_t [E(t)]^2}}{\sqrt{\sum_t [E_{FOM}(t)]^2}}\right), \tag{4.1}$$

where $E(t)$ is the sum of the kinetic and linear deformation energies.

$$E(t) = \frac{1}{2}\dot{\mathbf{u}}(t)^{\mathrm{T}}\mathbf{M}\dot{\mathbf{u}}(t) + \frac{1}{2}\mathbf{u}(t)^{\mathrm{T}}\mathbf{K}\mathbf{u}(t),$$
$$\Delta E(t) = E_{FOM}(t) - E_{ROM}(t). \tag{4.2}$$

ii. Relative discrepancy of the displacement

$$e_2 = \max\left(0, \quad 1 - \frac{\sqrt{\sum_t [\Delta\mathbf{u}(t)^{\mathrm{T}}\Delta\mathbf{u}(t)]}}{\sqrt{\sum_t [\mathbf{u}_{\mathrm{FOM}}(t)^{\mathrm{T}}\mathbf{u}_{\mathrm{FOM}}(t)]}}\right), \tag{4.3}$$

where

$$\Delta\mathbf{u}(t) = \mathbf{u}_{\mathrm{FOM}}(t) - \mathbf{u}_{\mathrm{ROM}}(t). \tag{4.4}$$

iii. Relative discrepancy of the velocity

$$e_3 = \max\left(0, \quad 1 - \frac{\sqrt{\sum_t [\Delta\dot{\mathbf{u}}(t)^{\mathrm{T}} \Delta\dot{\mathbf{u}}(t)]}}{\sqrt{\sum_t [\dot{\mathbf{u}}_{\mathrm{FOM}}(t)^{\mathrm{T}} \dot{\mathbf{u}}_{\mathrm{FOM}}(t)]}}\right), \tag{4.5}$$

where

$$\Delta\dot{\mathbf{u}}(t) = \dot{\mathbf{u}}_{\mathrm{FOM}}(t) - \dot{\mathbf{u}}_{\mathrm{ROM}}(t). \tag{4.6}$$

iv. Relative oscillatory deviation at the blade tip

$$e_4 = \max\left(0, \quad 1 - \sqrt{\frac{1}{N_{tip}} \sum_{i \in \boldsymbol{I_{tip}}} \left(\frac{o_{FOM,i} - o_{ROM,i}}{o_{FOM,i}}\right)^2}\right), \tag{4.7}$$

where $\mathrm{I}_{tip} \in \mathbb{R}^{N_{tip}}$ contains N_{tip}, the number of displacement indices corresponding to the degree of freedom of the blade-tip surface.

$$o_i = \max[\mathbf{u}_i(t)] - \min[\mathbf{u}_i(t)]. \tag{4.8}$$

v. Relative discrepancy of the displacement at the blade-tip node

$$e_5 = \max\left(0, \quad 1 - \frac{\sqrt{\sum_t [\Delta\mathbf{u}^{tip}(t)^{\mathrm{T}} \Delta\mathbf{u}^{tip}(t)]}}{\sqrt{\sum_t \left[\mathbf{u}_{FOM}^{tip}(t)^{\mathrm{T}} \mathbf{u}_{FOM}^{tip}(t)\right]}}\right), \tag{4.9}$$

where

$$\Delta\mathbf{u}^{tip}(t) = \Delta\mathbf{u}_{FOM}^{tip}(t)^{\mathrm{T}} - \Delta\mathbf{u}_{ROM}^{tip}(t). \tag{4.10}$$

4.2.2 Comparison among POD-based ROMs

Based on the proposed accuracy factors, the POD-based ROMs are assessed in terms of accuracy and robustness. A nonlinear time-transient simulation is performed for up to 0.5 s (500 steps) in the first test case, which has an analysis condition of $\alpha_e = 1.0$ and $\omega_e = 1.0$. The tolerance concerning the nonlinear force residual is set to be $\epsilon \leq 10^{-5}$ for the converged solutions. If the ROM fails to obtain a converged solution, it is indicated by an "x" in the subsequent results figure.

In hyper-reduction-based ROMs, both POD-DEIM and POD-GNAT can be used to define a reduced mesh by considering the number of POD (n) and DEIM (m) bases independently, whereas POD-ECSW can only be used to define a different reduced mesh that depends on the number of POD bases and the training tolerance ϵ_{NNLS} in Eq. (3.17). In this example, the training tolerance ϵ_{NNLS} was set to 10^{-4} [48]. The number of selected elements was determined by examining the number of PODs used. Information about the number of the selected elements is summarized in Table 4.3.

Table 4.3 Summary of the selected elements for POD-ECSW

No. of POD bases (n)	10	20	30	40	50	60	70	80	90	100
No. of sampled elements ($\tilde{\mathbf{E}}$)	73	109	218	288	357	427	512	584	664	755

Figure 4.5 shows the five accuracy factors used for the various number of POD and DEIM bases. In all the POD-based-ROMs, it is observed that the accuracy

factors tend to increase as the number of POD bases increase. However, the POD-DEIM approach shows numerical instability in all the accuracy factors, failing to converge when a certain number of bases are selected. Specifically, when more than 90 POD bases are used, POD-DEIM will not converge for any number of DEIM bases. Considering the convergence tendency, a sufficient number of DEIM bases will be needed when the number of POD bases is increased. Such instability may be due to the loss of the symmetric property when the tangent matrix $\tilde{\mathbf{K}}$ is approximated by applying the Galerkin projection in the hyper-reduction approach. From that perspective, POD-DEIM may lead to unstable situations for multi-query or parametric formulations when using a variety of arbitrary inputs.

By contrast, POD-GNAT shows good convergence characteristics for all the selected numbers of POD and DEIM bases. When the number of POD bases is constant, even if the number of DEIM bases increased, the effect on the accuracy factors is much smaller than that of POD-DEIM. It should be noted that in POD-GNAT, accuracy increases almost linearly in proportion to the number of POD bases used, and even a smaller number of DEIM bases is capable of guaranteeing converged solutions. The stability of POD-GNAT is due to the minimization of the global residual by applying the Gauss-Newton approach in Eq. (3.12) to the non-symmetric tangent matrix $\tilde{\mathbf{K}}$. POD-ECSW exhibits improved numerical stability by achieving high accuracy and convergence characteristics for all the selected numbers of POD bases. Specifically, sufficient accuracy is exhibited for only a small number of POD bases, similar to the result obtained in the approach that solely applied the

POD-Galerkin projection. This improvement is owing to the application of ECSW that preserved the symmetric properties and energies of the full-order representation, as shown by the trend in Fig. 4.6. Consequently, POD-GNAT and POD-ECSW build a more robust reduced-order representation than POD-DEIM.

Additionally, the computational costs of CPU time during the off-line and online stages are compared to evaluate the computational efficiency. The value of the CPU time during the online stage corresponds to the time-transient simulation (1,000 steps) for Case 1 ($\alpha_e = 1.0,\ \omega_e = 1.0$). Moreover, all computations are performed using serial operations (single CPU).

Each ROM is constructed using numbers of bases with accuracy factors exceeding 0.95, as shown in Fig. 4.5. Hence, 350 and 200 DEIM bases are used to approximate the nonlinear terms in POD-DEIM and POD-GNAT, respectively. It is noted that POD-GNAT is used with a relatively larger number of POD bases than that of POD-DEIM, while the DEIM bases used are significantly fewer than those of POD-DEIM. In contrast, POD-ECSW is applied using a comparatively smaller number of POD bases than both POD-DEIM and POD-GNAT. Subsequently, 218 selected elements associated with the 30 POD bases are obtained to define the reduced meshes. The relevant configuration of the reduced meshes is presented in Fig. 4.7, and the information about the bases is summarized in Table 4.4.

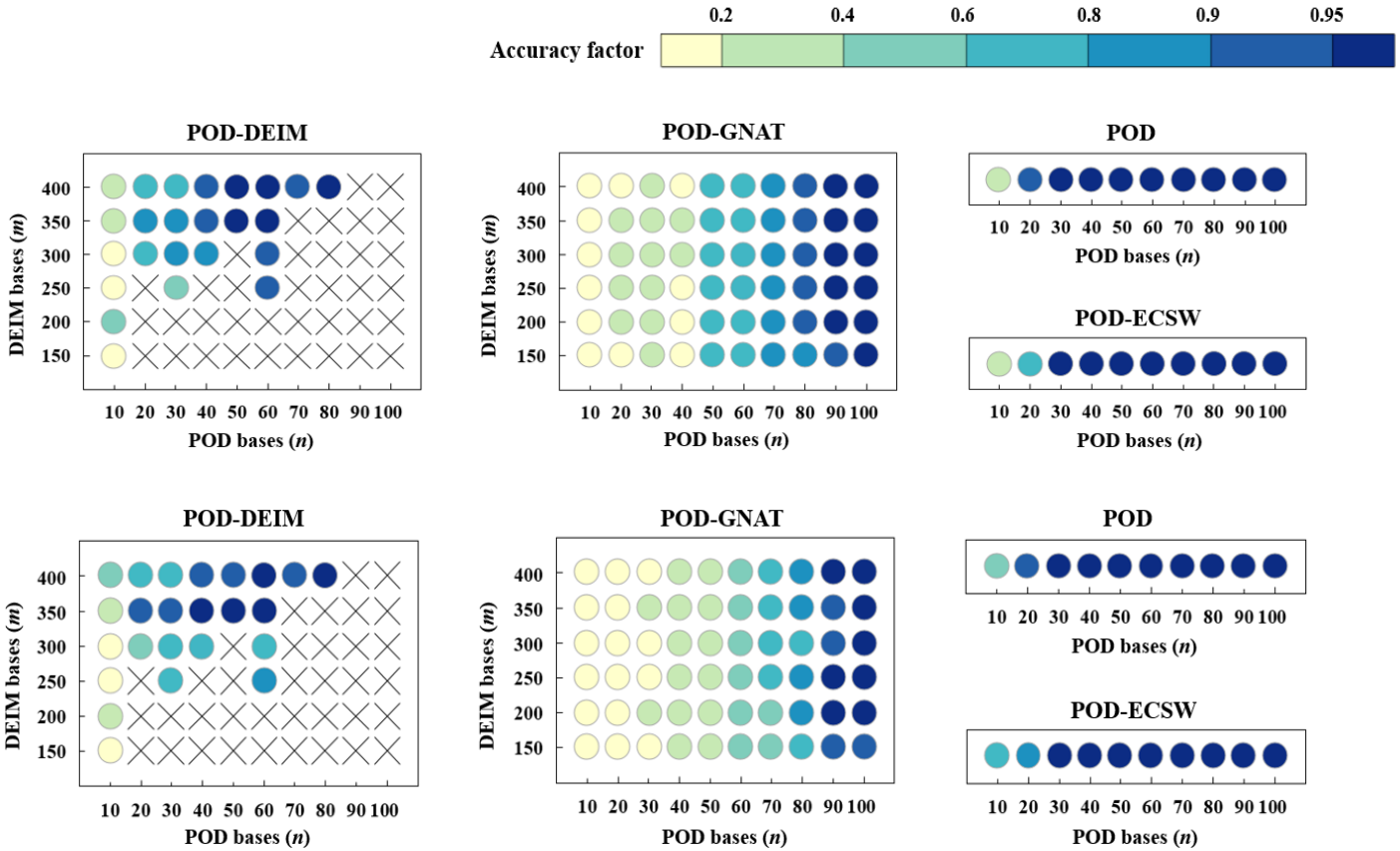

Fig. 4.5 Comparison of the accuracy factors in terms of the number of reduced bases.

c) e_3

d) e_4

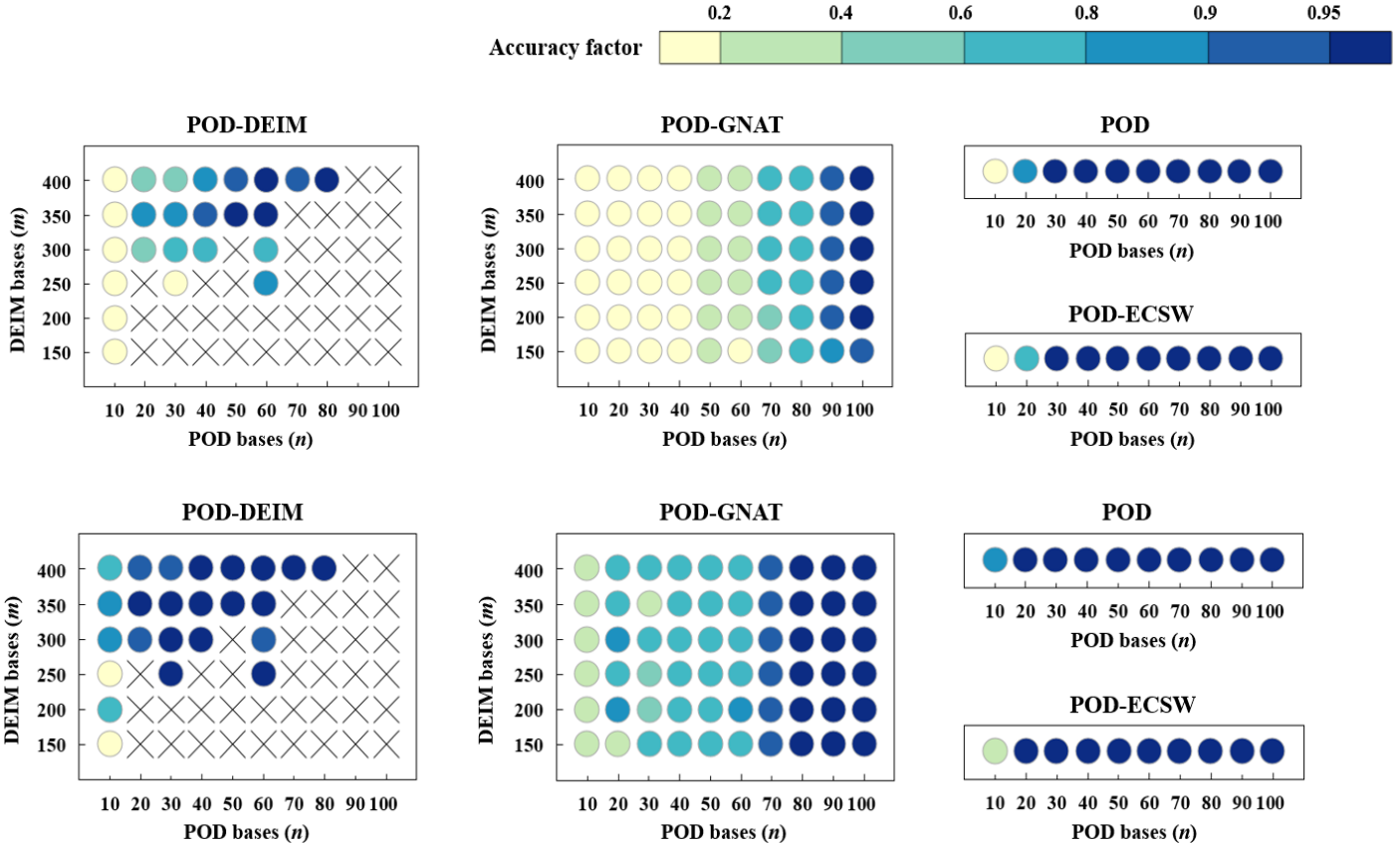

Fig. 4.5 Comparison of the accuracy factors in terms of the number of reduced bases (cont.).

e) e_5

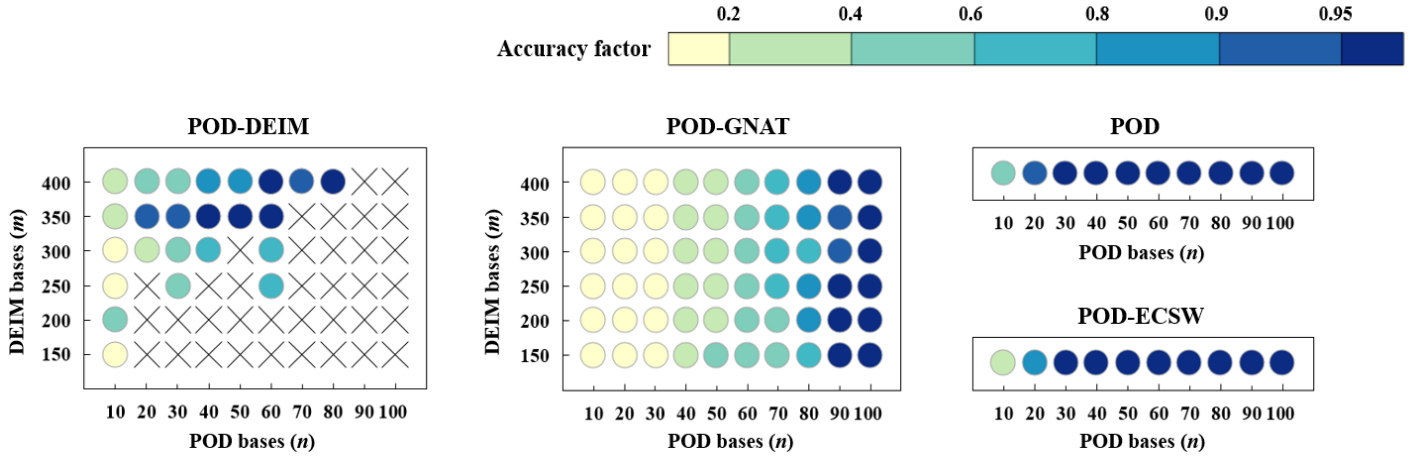

Fig. 4.5 Comparison of the accuracy factors in terms of the number of reduced bases (cont.).

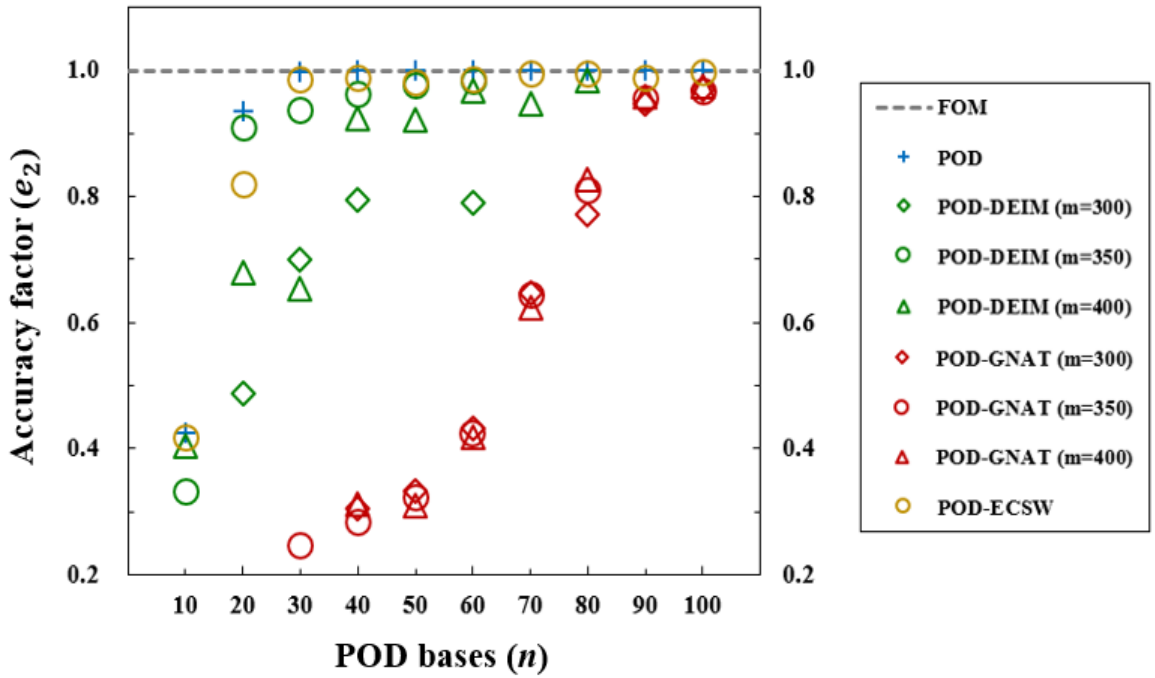

Fig. 4.6 Accuracy factors with respect to increasing reduced bases.

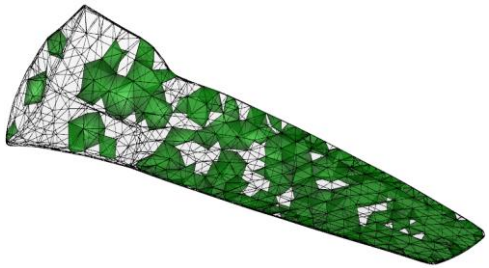

a) POD-DEIM

(350 DEIM bases)

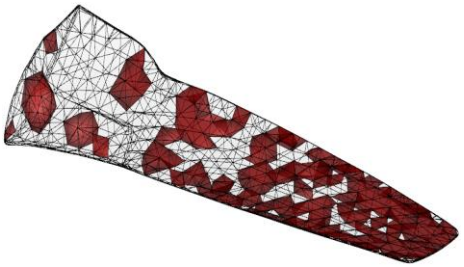

b) POD-GNAT

(200 DEIM bases)

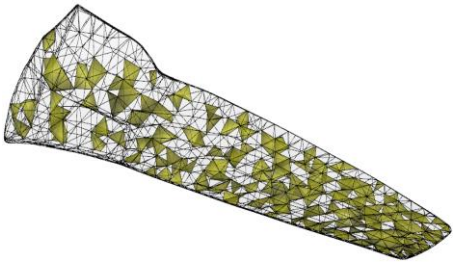

c) POD-ECSW

(218 selected elements)

Fig. 4.7 Accuracy factors with respect to increased reduced bases.

Table 4.4 Number of the reduced bases used for ROM

	POD	POD-DEIM	POD-GNAT	POD-ECSW	
POD bases (n)	30	50	100	30*	* No. of sampled elements : 218
DEIM bases (m)	-	350	200	-	

Figure 4.8-a compares the computational time between FOM and the POD-based ROMs during the online stage. Applying POD alone improves the computational time by only twice, when compared to FOM. In contrast, the hyper-reduction-based ROMs (POD-DEIM, POD-GNAT, and POD-ECSW) exhibit significant improvements in the computational time (11.1, 14.8, and 20.7 times faster than the FOM prediction, respectively). In particular, POD-ECSW, which is applied using a smaller number of POD bases than POD-DEIM and POD-GNAT, exhibits the optimum online computational efficiency (its CPU times are 1.9 times and 1.4 times faster, respectively). It should be noted that POD-GNAT, which is used with a smaller number of DEIM bases and a larger number of POD bases than POD-DEIM, shows improved computational efficiency. This implies that the computational efficiency of a hyper-reduction-based ROM combined with DEIM approximation mainly depends on the number of DEIM bases used. This determines the scale of the repetitive computations for constructing the reduced-order representation during the online stage.

The total computational time, including the off-line stage, in terms of the number of computations, is compared between FOM and POD-based ROMs. The off-line time consists of a sum of the time for sampling analysis, time for extracting the reduced-order basis, and time for constructing off-line terms related to the reduced meshes. Herein, POD-DEIM and POD-GNAT extract DEIM bases from the huge snapshots of the residual-force vectors. POD-ECSW extracts the selected elements from an enormous training dataset. Then, they consume more off-line computational

phase time than that by the POD. Among those, POD-ECSW shows the highest off-line computational time because it solves a time-consuming sparse NNLS problem (Fig. 4.8-b). Such off-line computational time is required once at the beginning of the computation. Then, the online computational time is obtained and accumulated for computational cost. Hence, it is expected that the total computational cost in the ROM framework will generally improve as similar computations are repeated. Specifically, the hyper-reduction-based ROMs, which has a remarkably larger speed-up factor compared to POD in the online stage, show a significant reduction in the cumulative CPU time while the similar computation is repeated.

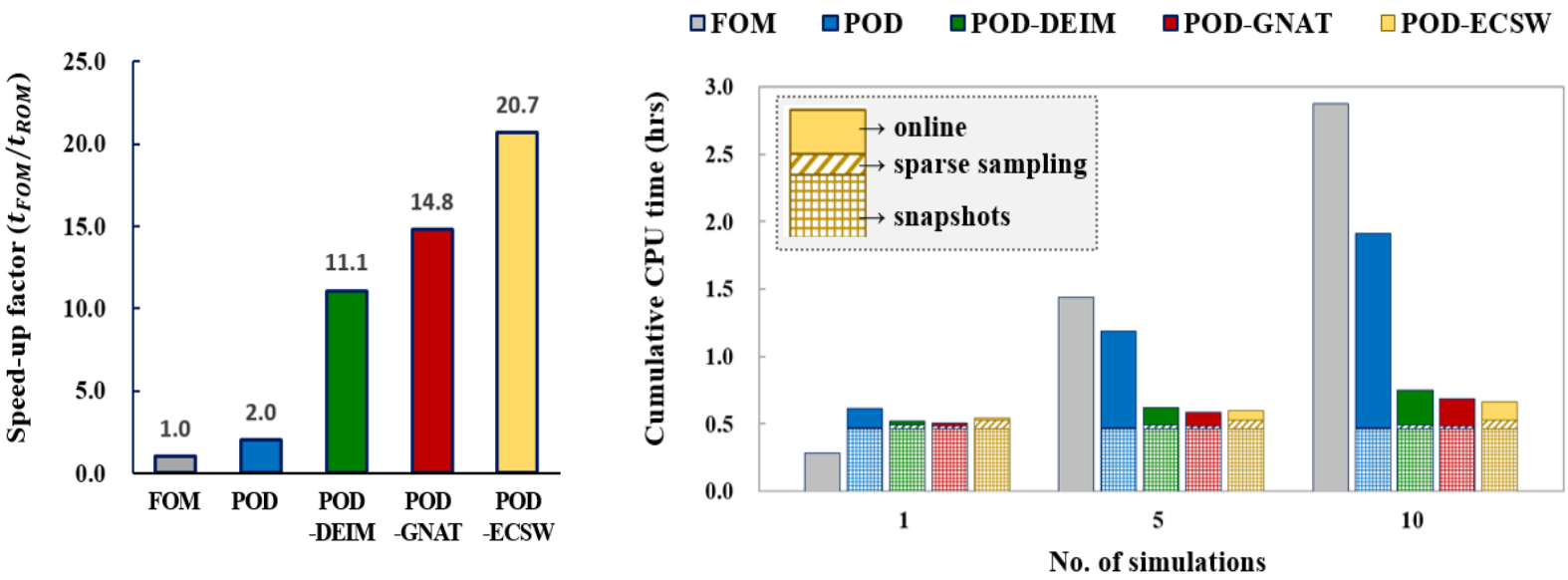

a) Online stage

b) Off-line and online stage

Fig. 4.8 Computational cost among FOM and POD-based ROMs.

4.2.3 Parametric Study of POD-based ROMs

To demonstrate the performance of the ROMs within the parametric variations, three test cases are examined. The number of bases used for ROM construction is identical to that shown in Table 4.4. The relevant analysis conditions for the parametric study are listed in Table 4.5.

Table 4.5 Summary of test conditions for the parametric study

Condition No.	Case No. (E, ρ, Ω)	Excitation factor	
		Loading (α_e)	Frequency (ω_e)
I	2 (73, 2850, 1260)	1.0	1.0
II	3 (74, 2910, 1340)	1.5	1.0
III	4 (72, 2640, 1470)	0.5	2.0

The deformation history at Point A (the trailing edge at the blade tip) is used to evaluate the accuracy of the ROMs. Moreover, the relative discrepancy in the deformation field between the FOM and ROMs is introduced. The total deformation is defined as follows:

$$\mathbf{u}_A^{tot} = \sqrt{\left(\mathbf{u}_{x,A}\right)^2 + \left(\mathbf{u}_{y,A}\right)^2 + \left(\mathbf{u}_{z,A}\right)^2}, \tag{4.11}$$

where $\mathbf{u}_{x,A}$, $\mathbf{u}_{y,A}$, and $\mathbf{u}_{z,A}$ denote the displacement component of each direction at the Point A.

Figure 4.9 shows the total deformation history at Point A. For Conditions I and II, all ROMs are in good agreement when compared to the FOM. Herein, the solution

history from the ROMs is recovered using POD bases. For Condition III, which has a larger nonlinearity than Conditions I and II, POD-DEIM does not deliver an accurate solution and diverged. However, POD, POD-GNAT, and POD-ECSW show a better correlation with FOM.

To quantify the discrepancy in the hyper-reduction-based ROMs, the root mean squared relative error (RMSRE) of the total deformation history at Point A is considered. Table 4.6 provides a comparison of the RMSRE values between the ROMs. POD-GNAT and POD-ECSW achieve a significantly higher accuracy for Conditions I and II (the average relative discrepancy was within 2%). However, POD-GNAT shows a relative difference for Condition III. The accuracy trend of the number of reduced bases indicate that the accuracy will improve when the number of reduced-order bases is increased (Figs. 4.6 and 4.7).

The reduced-order representations based on hyper-reduction reveal that the stability of POD-GNAT and POD-ECSW is better than that of POD-DEIM. Thus, POD-ECSW can accurately address broad parametric variation. This is determined by comparing the von Mises stress field between FOM and hyper-reduction-based ROMs. Figure 4.10 demonstrates von Mises stress field, which is computed at the time of maximum deformation in each condition. When compared against FOM results, POD-ECSW shows better correlation for all the conditions.

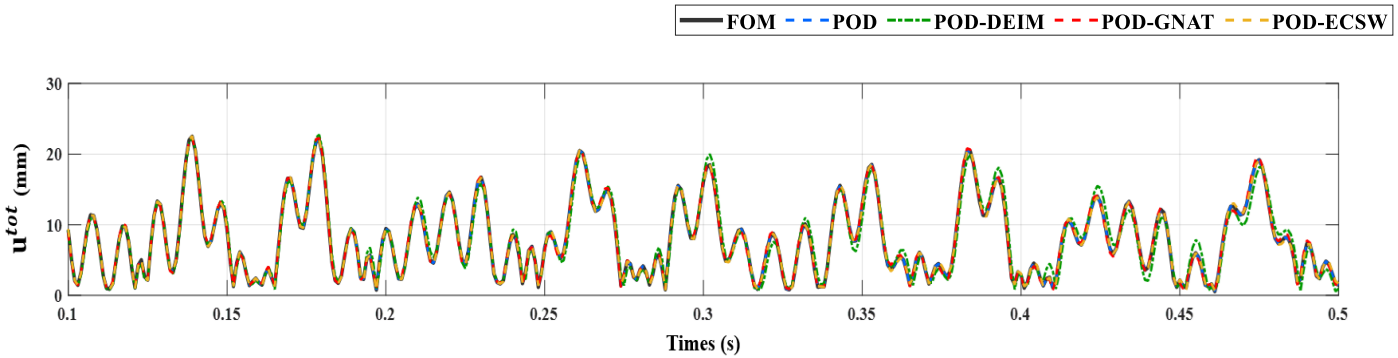

a) Condition I

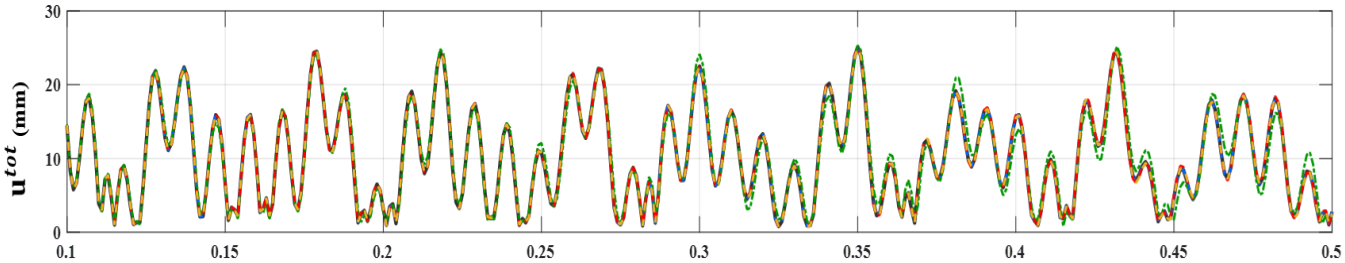

b) Condition II

Fig. 4.9 Comparison of the total deformation for the different conditions.

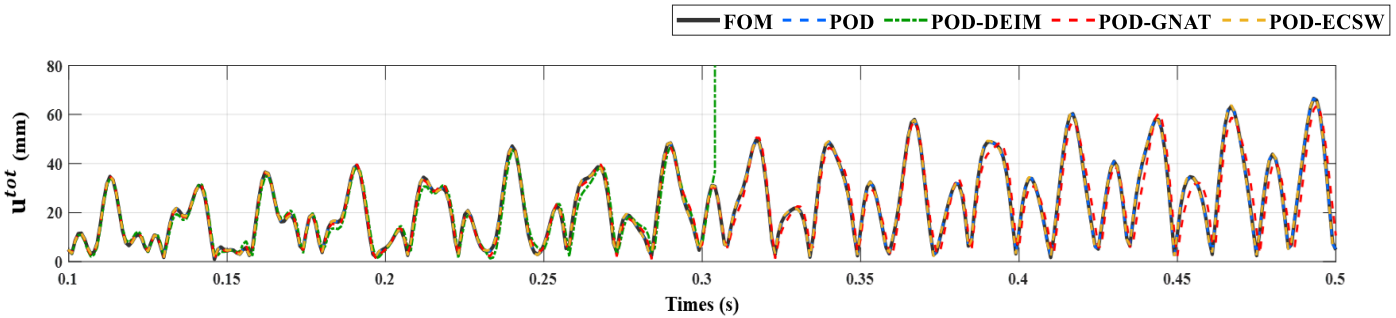

c) Condition III

Fig. 4.9 Comparison of the total deformation for the different conditions (cont.).

Table 4.6 Comparison of the RMSRE (%) regarding the total deformation

	POD-DEIM	POD-GNAT	POD-ECSW
Condition I	4.205	1.915	1.620
Condition II	6.312	1.638	1.013
Condition III	N/A	7.911	1.429

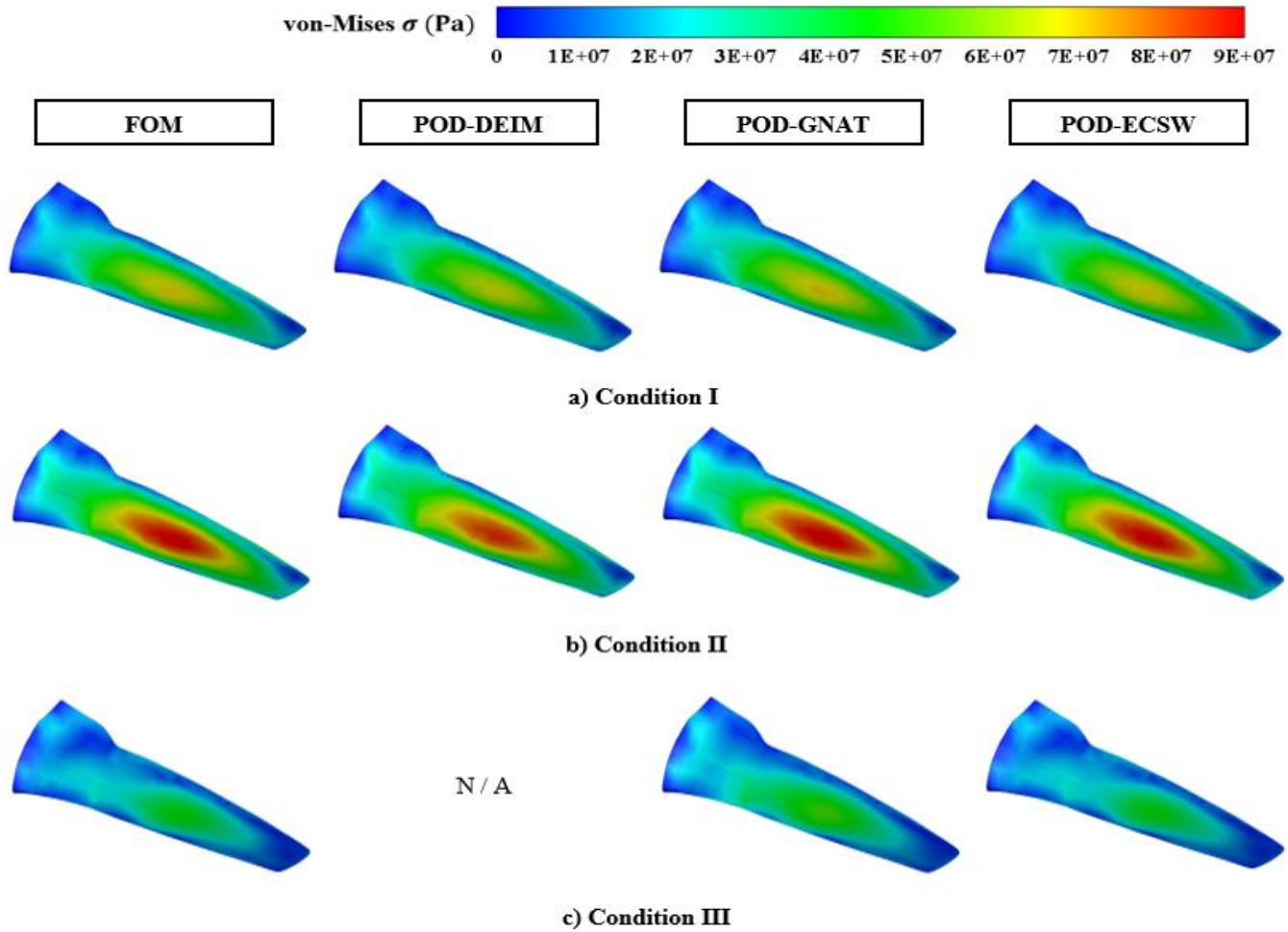

Fig. 4.10 Comparison of von Mises stress for the different conditions.

4.3 Extension to Other Frameworks

Based on the results presented in the foregoing sections, it is found that POD-ECSW approach provide the most robust reduced-order representation for the nonlinear time-transient formulation, including parametric variations.

In this section, POD-ECSW will be further extended to modal and forced vibration frameworks of rotating component. The rotating component is frequently subjected to various vibratory loads that may cause catastrophic failures such as high cycle fatigue [79]. There have been two approaches to prevent HCF problems [80]. The first approach is to design to avoid dangerous resonances in the operating range. This is a qualitative standard design practice to avoid resonance using the Campbell diagram. Generally, the resonance should be avoided in the lower-order structural modes (first bending, torsion modes, etc.). The second approach is to allow resonance in the operating range and to quantitatively assess the associated response level of the blades in resonant conditions. This approach is required to accurately predict the structural response under the resonant condition by conducting a forced vibration analysis. Therefore, in the design process of a rotating component, the modal and forced vibration analyses need to be performed to investigate their vibration characteristics. However, rather expensive nonlinear static and linear frequency response analyses are usually accompanied by a frequency domain analysis. The traditional mode superposition method (MSM) effectively reduces the cost of the frequency response analysis. However, the nonlinear static analysis of earlier processes remains as the computational bottleneck.

In this section, the application of POD-ECSW regarding the modal and forced vibration analyses of turbomachinery rotating blades will be investigated, respectively. Moreover, as in the previous subsection (time-transient analysis), the present results are validated by comparison with those obtained using FOM.

4.3.1 Modal Analysis

In this subsection, the modal analysis is executed. The relevant example is the transonic fan blade, NASA Rotor 67. The three-dimensional fan-blade configuration is discretized by 10-node tetrahedral elements with $N_e = 8{,}384$, and corresponding number of the displacement DOFs is $N = 50{,}268$. The material of the blade structure is titanium alloy, i.e., Young's modulus $E = 117\ \mathrm{GPa}$, density $\rho = 4{,}539.5\ \mathrm{kg/m^3}$, and Poisson's ratio $\nu = 0.3$.

To construct the reduced-order representation, a sampling analysis using the full-order representation under the pure centrifugal load condition, in which the number of time steps is 100 at intervals of 0.0001s. The base surface of the blade is clamped.

For POD-ECSW, the training tolerance ϵ_{NNLS} is set to be 10^{-3}. Then, 148 selected elements and corresponding weights are determined by using 30 POD basis vectors with a 98% energy ratio (Eq. (2.23)) to FOM.

Table 4.7 shows a comparison of the natural frequencies. When compared with the results obtained by FOM, POD-ECSW shows good agreement within 0.5% of the average discrepancy. In addition, the online computational time consumed by POD-ECSW is 0.42 s, and that by FOM is 7.5s. Therefore, the computational cost is

significantly improved as it is reduced by 95%.

It is important to create a Campbell diagram to evaluate the resonance under excitations. To do this, dynamic analyses within operating ranges are performed, and this will require a significant amount of computation. In the projection-based MOR framework, once the ROMs are constructed, it will be straightforward to perform the modal analysis at various rotating conditions. This advantage makes it easier to create the Campbell diagram for resonance evaluation. Figure 4.12 shows a Campbell diagram for resonance evaluation. POD-ECSW exhibits a satisfactory correlation with FOM prediction. Specifically, when the rotational speed is increased, the natural frequency of each mode is also increased by the rotational effect. However, there is a difference in its increase rate for each mode. This may be explained by Southwell effect [81], by which coupling between the flapping and lead–lag modes occurs, owing to the difference in their natural frequencies' increase rate among the modes as the blade rotates.

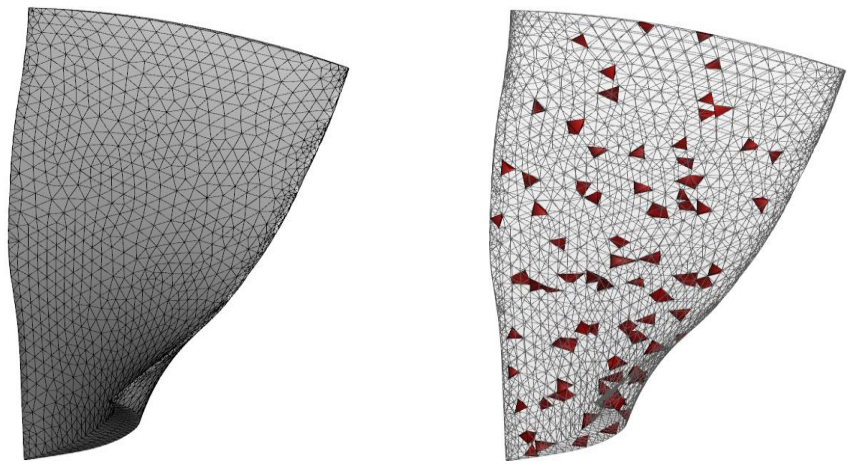

(a) Discretized fan blade **(b) Reduced mesh (148 elements)**

Fig. 4.11 NASA Rotor 67 fan blade for the modal analysis

Table 4.7 Comparison of the natural frequencies in the rotating condition (Hz)

	Mode 1	Mode 2	Mode 3	Mode 4	Mode 5	Avg. discrepancy, %
POD-ECSW	536.8	1240.8	1759.9	2544.3	2822.3	0.5%
Reference (FOM)	535.8	1238.8	1770.1	2523.3	2838.2	-

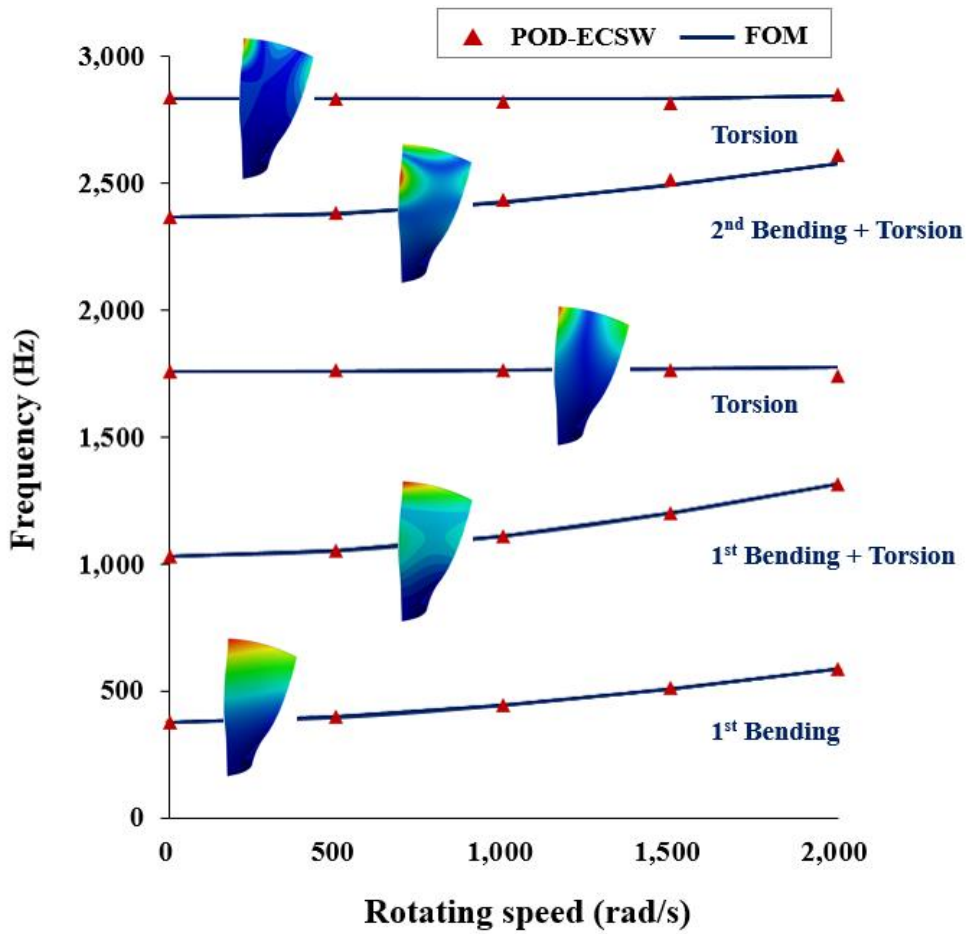

Fig. 4.12 Campbell diagram.

4.3.2 Forced Vibration Analysis

In this subsection, a comparison of the computational performance will be examined among the different MOR frameworks when applied to rotating component forced vibration analysis. The procedure of the forced vibration analysis includes the nonlinear static solution for the evaluation of the stiffness variation by the centrifugal force and time-harmonic solution to obtain the steady-state frequency response. The relevant approaches considered in this study are as follows:

- **FOM**: The pre-stressed stiffness matrix $\mathbf{K}$ is obtained by the nonlinear static analysis. Then, linear frequency response analysis is conducted. This will be a reference representation.
- **POD**: The nonlinear static- and linear frequency analyses are conducted in sequence by solely applying POD-Galerkin projection.
- **POD-ECSW**: The nonlinear static- and linear frequency analyses are conducted by using a small number of selected elements determined via ECSW.

To evaluate the accuracy of the present MOR, two indices representing the relative displacement field and von-Mises stress discrepancies are defined as follows:

$$EI_u(\%) = \frac{\sqrt{\sum_{i=1}^{n_s} \left\| \mathbf{u}_i^{FOM} - \mathbf{u}_i^{ROM} \right\|_2^2}}{\sqrt{\sum_{i=1}^{n_s} \left\| \mathbf{u}_i^{FOM} \right\|_2^2}} \times 100 \tag{4.12}$$

$$EI_\sigma(\%) = \frac{\sqrt{\sum_{i=1}^{n_s} \left\| \sigma_i^{FOM} - \sigma_i^{ROM} \right\|_2^2}}{\sqrt{\sum_{i=1}^{n_s} \left\| \sigma_i^{FOM} \right\|_2^2}} \times 100 \tag{4.13}$$

where n_s denotes the number of imposed frequencies. $\mathbf{u}$ and σ are the complex displacement and the maximum von-Mises stress obtained from the alternating stress, respectively. In addition, to compare the computational efficiency between FOM and ROM, the online speed-up factor S (t^{FOM}/t^{ROM}) is introduced.

The relevant example is the first-stage blade of a 75-MW GT11N gas turbine. The three-dimensional turbine blade configuration is discretized by 10-node tetrahedral elements with $N_e = 376{,}538$, and corresponding number of the displacement DOFs is $N = 1{,}774{,}512$. The material of the blade structure is Alloy In-738LC with a Rayleigh damping mass matrix multiplier of $50s^{-1}$ (i.e., Young's modulus $E = 200.6\ \text{GPa}$, density $\rho = 8{,}420\ \text{kg/m}^3$, and Poisson's ratio $\nu = 0.28$). For the frequency response analysis, a transverse tip harmonic force of 1,000 N is imposed using the frequency band extending from 500 to 4,500 Hz at the interval of 40 Hz.

Regarding the off-line stage, the snapshot matrix $\mathbf{W}_d$ is constructed based on the nonlinear time-transient analysis results. The relevant sampling analysis is performed under the sinusoidal angular velocities of amplitude 3,600 RPM are imposed along the transverse, longitudinal and rotation axes for each. The relevant sinusoidal function oscillates during 5 periods with the frequency of 1,000 Hz. Then, 50 POD basis vectors are extracted, which have a 98% energy ratio to FOM.

For POD-ECSW, the training tolerance ϵ_{NNLS} is set to be 10^{-3}. Then, 605 selected elements and corresponding weights are determined by using 50 POD basis vectors, as shown in Fig. 4.13.

Table 4.8 compares the relative discrepancy and speed-up factor between FOM

and ROMs. Both POD and POD-ECSW achieve a significantly higher accuracy (the average relative discrepancies within 1.78% and 2.19% for EI_u and EI_σ). Moreover, POD-ECSW shows an improved speed-up factor compared to POD. Figure 4.14 shows the variations of the relative discrepancies in terms of the parametrized rotational velocity. In all the cases, the relevant discrepancies are observed to be within 2%. Specifically, the maximum transverse displacement is demonstrated for different rotational velocity, as shown in Fig. 4.15. Except for the slight deviation in the high frequency range, the peak location and corresponding displacement responses of ROMs are identical to those by FOM.

Sections of this chapter have been published in the following relevant journal articles:

Kim, Y., Cho, H., Park, S., and Shin, S.-J., "Advanced Structural Analysis based on Reduced Order Modeling for Gas Turbine Blade," *AIAA Journal*, Vol. 56, No. 8, 2018, pp. 3369–3373.

Kim, Y., Kang, S., Cho, H., and Shin, S.-J., "Improved Nonlinear Analysis of a Propeller Blade based on Hyper-reduction," *AIAA Journal*, Vol. 60, No. 3, 2022, pp. 1909–1922.

Kang, S., **Kim, Y.**, Cho, H., and Shin, S.-J., "Improved Hyper-reduction Approach for the Forced Vibration Analysis of Rotating Components," *Computational Mechanics*, Vol. 69, 2022. pp. 1443-1456.

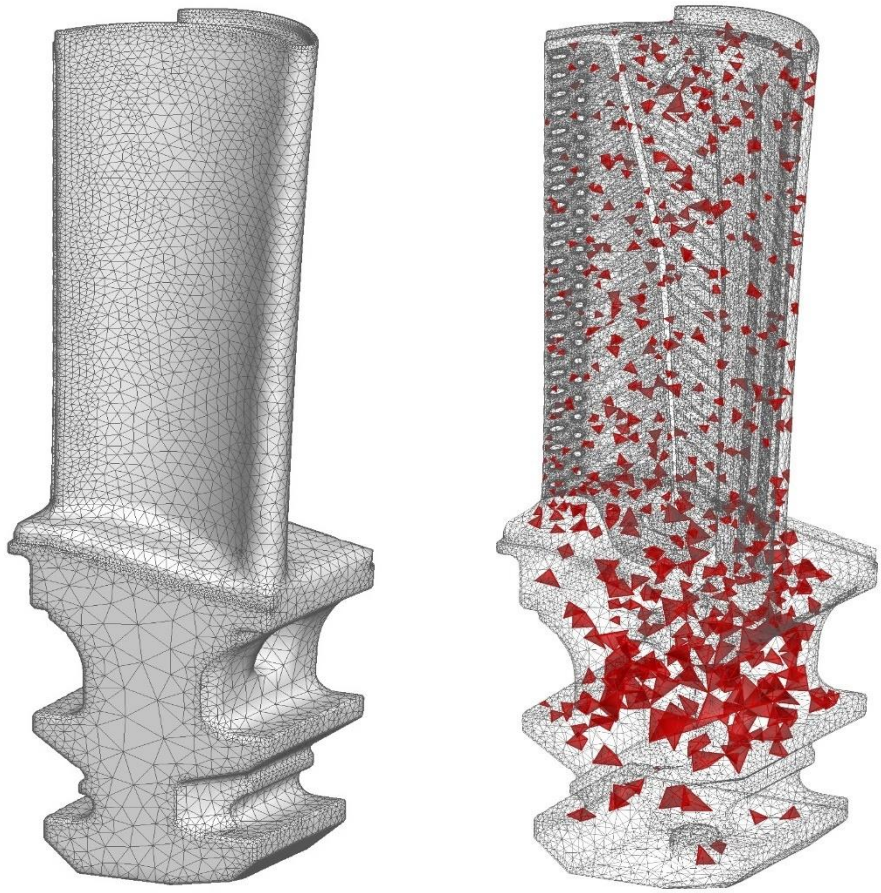

(a) Discretized turbine blade **(b) Reduced mesh (605 elements)**

Fig. 4.13 GT11N turbine blade for the forced vibration analysis

Table 4.8 Comparison of the relative discrepancy and speed-up factor for the GT11N turbine blade ($\boldsymbol{\Omega = 3,600}$ rpm)

	$EI_u(\%)$	$EI_\sigma(\%)$	S
POD	0.10	1.78	234.6
POD-ECSW	0.68	2.19	936.3

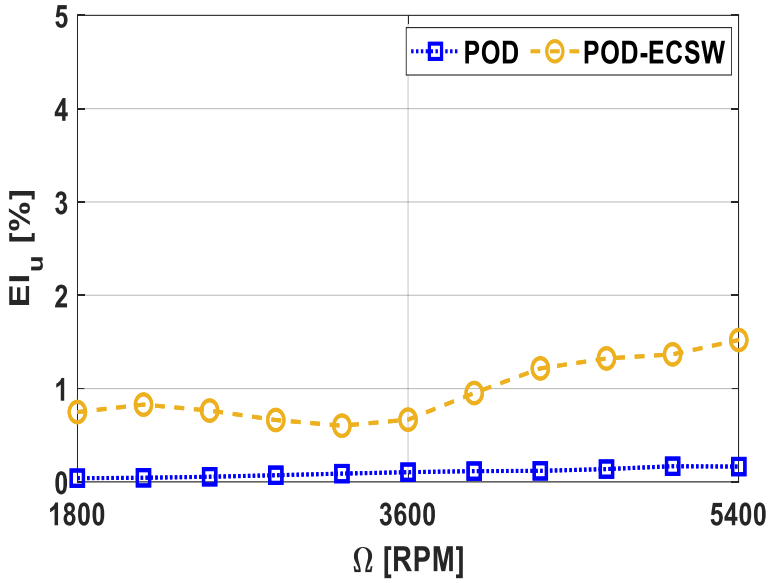

(a) EI_u

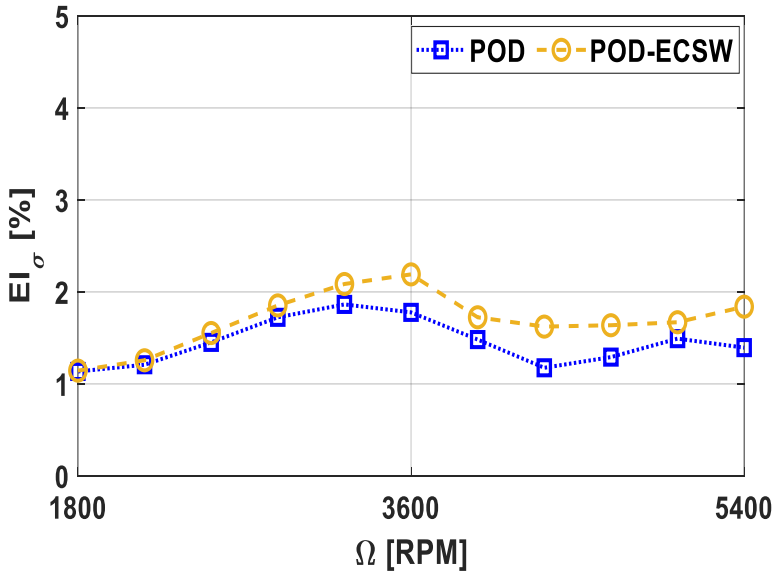

(b) EI_σ

Fig. 4.14 Comparison of the relative discrepancies in terms of Ω

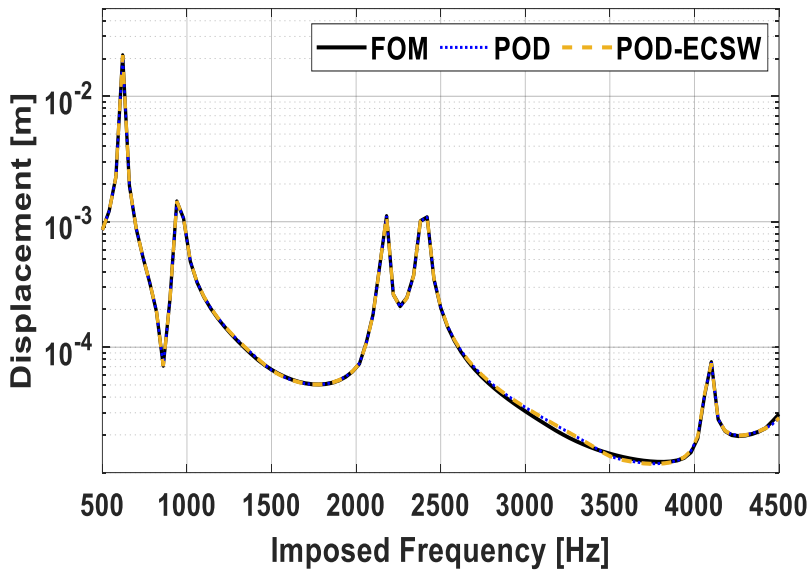

(a) $\Omega = 1,800$ rpm

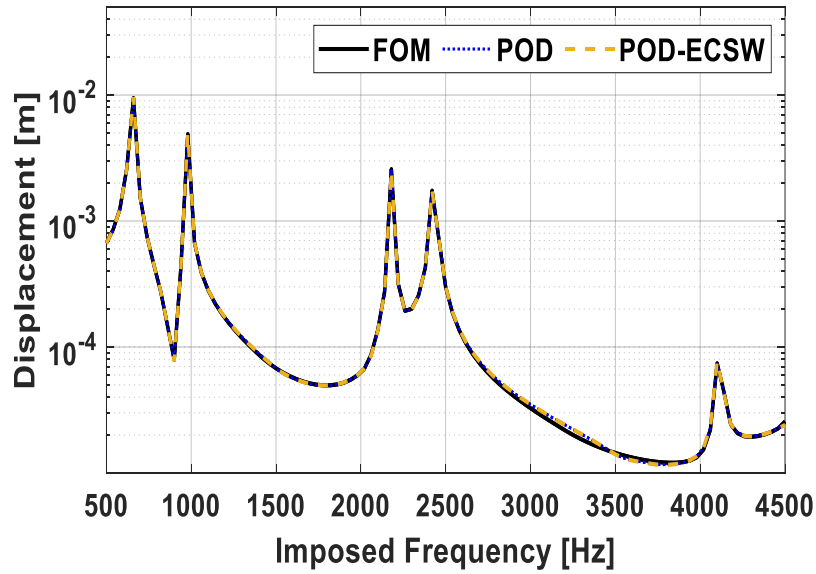

(b) $\Omega = 5,400$ rpm

Fig. 4.15 Maximum transverse displacement amplitude for the different Ω

Chpater 5

Parametric Hyper Reduced-order Model for a Geometrically Imperfect Component

As mentioned in Introduction, if the FE representation varies owing to the geometric imperfection, the reduced-order representation will be expensively reconstructed. In this dissertation, to overcome such limitation, both defect-parametric reduced-order model (DpROM) and hyper-reduction will be used.

DpROM constructs a geometrically nonlinear ROM that is capable of describing parameterized shape defect. In its off-line stage, a set of the shape defects that may occur during manufacturing or operation will be defined as a displacement field with respect to the nominal FE representation. The reduced basis is extracted by using the model-based approach based on the nominal FE formulation and pre-defined defect-displacement subspace alone. Subsequently, the reduced stiffness tensor is constructed by projecting the element-level full-order tensor with the reduced basis.

In the online stage, ROM, which parametrically relies on the defect amplitude, is defined as a polynomial function comprising the reduced stiffness tensors with regard to the reduced coordinate. In the following sections, the relevant formulation and framework of the proposed ROM will be presented.

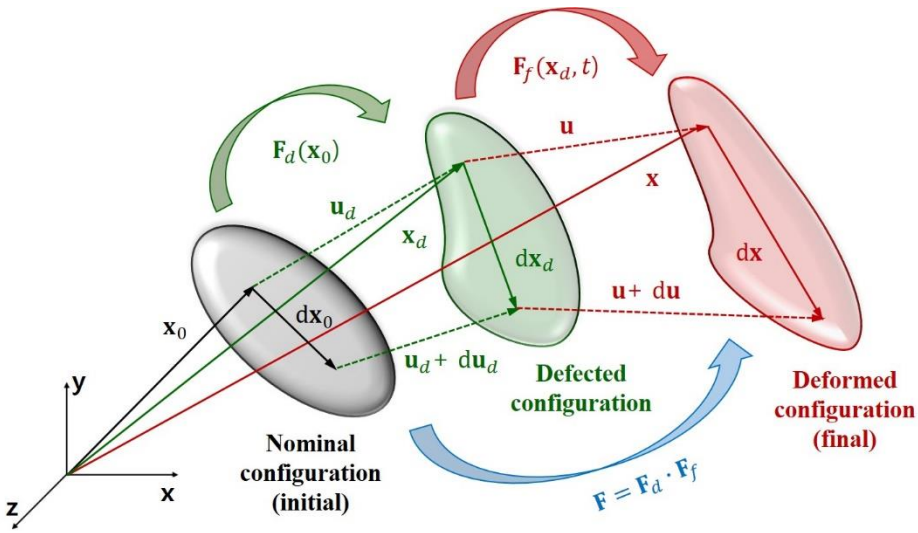

Fig. 5.1 Two-step movement of a continuum body regarding the defected geometry.

5.1 Modified Strain Approximation

In the current DpROM framework, the geometric imperfections are described as a set of the user-defined displacement fields (i.e., an additional assumed displacement), which will be integrated into the conventional strain formulation. This idea was suggested by Budiansky [82] for the post-buckling behavior in the presence of defects. Therefore, the total displacement fields of a structural object may be decomposed into the following two components: a defect-displacement (constant component) and an actual displacement (variable component). Beyond the deformation, a material point of the final coordinate in terms of the nominal (initial) configuration is defined as follows:

$$\mathbf{x} = \mathbf{x}_0 + \mathbf{u}_d + \mathbf{u}, \tag{5.1}$$

where $\mathbf{x}_0 = \{x_0, y_0, z_0\}$, $\mathbf{u}_d = \{u_d, v_d, w_d\}$, and $\mathbf{u} = \{u, v, w\}$ are the nominal

coordinates, and the defect- and actual displacement fields, respectively. Herein, $\mathbf{u}_d$ is a user-defined displacement field that represents the shape defect. The final coordinate $\mathbf{x}$ can be described by going through a two-step movement approach from the nominal coordinate $\mathbf{x}_0$, as shown in Fig. 5.1.

Assuming a continuous mapping, the differential line segments $\mathrm{d}\mathbf{x}_d$ and $\mathrm{d}\mathbf{x}$ in the defected and deformed configuration can be expressed with respect to $\mathrm{d}\mathbf{x}_0$, as follows:

$$\mathrm{d}\mathbf{x}_d = \mathbf{F}_d \mathrm{d}\mathbf{x}_0, \tag{5.2}$$

$$\mathrm{d}\mathbf{x} = \mathbf{F}_f \mathrm{d}\mathbf{x}_d = \mathbf{F}_f \mathbf{F}_d \mathrm{d}\mathbf{x}_0. \tag{5.3}$$

where deformation gradients $\mathbf{F}_d$ and $\mathbf{F}_f$ are rearranged as follows:

$$\mathbf{F}_d = \frac{\partial \mathbf{x}_d}{\partial \mathbf{x}_0} = \mathbf{I} + \frac{\partial \mathbf{u}_d}{\partial \mathbf{x}_0} = \mathbf{I} + \mathbf{H}_d, \tag{5.4}$$

$$\mathbf{F}_f = \frac{\partial \mathbf{x}}{\partial \mathbf{x}_d} = \mathbf{I} + \frac{\partial \mathbf{u}}{\partial \mathbf{x}_d} = \mathbf{I} + \mathbf{H}_f, \tag{5.5}$$

where $\mathbf{F}_d$ and $\mathbf{F}_f$ are the defect-deformation gradient in terms of the nominal coordinates and the final-deformation gradient in terms of the defected coordinates, respectively. $\mathbf{H}_d$ and $\mathbf{H}_f$ are the displacement gradients in the defected and deformed configuration, respectively.

By the chain rule, the displacement gradient with respect to the nominal coordinates is defined as follows:

$$\mathbf{H} = \frac{\partial \mathbf{u}}{\partial \mathbf{x}_0} = \frac{\partial \mathbf{u}}{\partial \mathbf{x}_d}\frac{\partial \mathbf{x}_d}{\partial \mathbf{x}_0} = \mathbf{H}_f \mathbf{F}_d \;\Leftrightarrow\; \mathbf{H}_f = \mathbf{H}\mathbf{F}_d^{-1}. \tag{5.6}$$

Using the relationship between Eqs. (5.2) - (5.6), the stretch between the deformed and defected configurations can be expressed as follows:

$$\begin{aligned} S &= d\mathbf{x}^T d\mathbf{x} - d\mathbf{x}_d{}^T d\mathbf{x}_d \\ &= d\mathbf{x}_0{}^T \mathbf{F}_d^T \left(\mathbf{F}_f^T \mathbf{F}_f - \mathbf{I}\right) \mathbf{F}_d d\mathbf{x}_0 \\ &= d\mathbf{x}_0{}^T \left(\mathbf{H} + \mathbf{H}^T + \mathbf{H}^T\mathbf{H} + \mathbf{H}_d^T\mathbf{H} + \mathbf{H}^T\mathbf{H}_d\right) d\mathbf{x}_0. \end{aligned} \tag{5.7}$$

Considering the strain measure with regard to the defected configuration, the modified Green-Lagrange strain tensor (second-order) is expressed as follows:

$$S = 2\mathrm{d}\mathbf{x}_d^T \mathbf{E}_f \mathrm{d}\mathbf{x}_d = 2\mathrm{d}\mathbf{x}_0^T \mathbf{F}_d^T \mathbf{E}_f \mathbf{F}_d \mathrm{d}\mathbf{x}_0. \tag{5.8}$$

This leads to

$$\begin{aligned} \mathbf{E}_f &= \frac{1}{2}\left(\mathbf{F}_f^T \mathbf{F}_f - \mathbf{I}\right) \\ &= \frac{1}{2}\mathbf{F}_d^{-T}\left(\mathbf{H} + \mathbf{H}^T + \mathbf{H}^T\mathbf{H} + \mathbf{H}_d^T\mathbf{H} + \mathbf{H}^T\mathbf{H}_d\right)\mathbf{F}_d^{-1}. \end{aligned} \tag{5.9}$$

Assuming the shape defects are small $(\text{i.e.}, \|\mathbf{H}_d\| \ll 1)$, an inverse of the defect-deformation gradient $\mathbf{F}_d^{-1}$ of Eq. (5.9) will be expanded via Neumann series [83] as follows:

$$\mathbf{F}_d^{-1} = (\mathbf{I} + \mathbf{H}_d)^{-1} \approx \sum_{n=0}^{N} (-\mathbf{H}_d)^n, \tag{5.10}$$

where N is the order for trimming the Neumann expansion sum.

Considering the first-order Neumann series in Eq. (5.10) (i.e., $\mathbf{F}_d^{-1} = (\mathbf{I} - \mathbf{H}_d)$), and substituting it into Eq. (5.9), the modified Green-Lagrange strain tensor can be written as follows while neglecting term $\mathcal{O}(\mathbf{H}_d{}^2)$:

$$\mathbf{E}_{f,N} = \frac{1}{2}\left(\mathbf{H} + \mathbf{H}^T + \mathbf{H}^T\mathbf{H} + \mathbf{H}_d^T\mathbf{H}^T - \mathbf{H}\mathbf{H}_d - \mathbf{H}_d^T\mathbf{H}^T\mathbf{H} - \mathbf{H}^T\mathbf{H}\mathbf{H}_d\right). \qquad (5.11)$$

5.2 Finite Element Formulation

For the FE-based nonlinear representation using the three-dimensional (3D) continuum element, the modified strain tensor, Eq. (5.11), can be rewritten as follows:

$$\mathbf{E}_{f,N} = \left(\mathbf{G} + \frac{1}{2}\mathbf{A}_1 + \mathbf{A}_2 + \mathbf{A}_3\mathbf{A}_1\right)\bar{\mathbf{B}}\mathbf{u}^e, \tag{5.12}$$

where

$$\mathbf{G} = \begin{bmatrix} 1 & 0 & 0 & 0 & 0 & 0 & 0 & 0 & 0 \\ 0 & 0 & 0 & 0 & 1 & 0 & 0 & 0 & 0 \\ 0 & 0 & 0 & 0 & 0 & 0 & 0 & 0 & 1 \\ 0 & 1 & 0 & 1 & 0 & 0 & 0 & 0 & 0 \\ 0 & 0 & 1 & 0 & 0 & 0 & 1 & 0 & 0 \\ 0 & 0 & 0 & 0 & 0 & 1 & 0 & 1 & 0 \end{bmatrix}, \tag{5.13}$$

$$\mathbf{A}_1 = \begin{bmatrix} u_{,x} & 0 & 0 & v_{,x} & 0 & 0 & w_{,x} & 0 & 0 \\ 0 & u_{,y} & 0 & 0 & v_{,y} & 0 & 0 & w_{,y} & 0 \\ 0 & 0 & u_{,z} & 0 & 0 & v_{,z} & 0 & 0 & w_{,z} \\ u_{,y} & u_{,x} & 0 & v_{,y} & v_{,x} & 0 & w_{,y} & w_{,x} & 0 \\ u_{,z} & 0 & u_{,x} & v_{,z} & 0 & v_{,x} & w_{,z} & 0 & w_{,x} \\ 0 & u_{,z} & u_{,y} & 0 & v_{,z} & v_{,y} & 0 & w_{,z} & w_{,y} \end{bmatrix}, \tag{5.14}$$

$$\mathbf{A}_2 = -1 \times \begin{bmatrix} u_{d,x} & v_{d,x} & w_{d,x} & 0 & 0 & 0 & 0 & 0 & 0 \\ 0 & 0 & 0 & u_{d,y} & v_{d,y} & w_{d,y} & 0 & 0 & 0 \\ 0 & 0 & 0 & 0 & 0 & 0 & u_{d,z} & v_{d,z} & w_{d,z} \\ u_{d,y} & v_{d,y} & w_{d,y} & u_{d,x} & v_{d,x} & w_{d,x} & 0 & 0 & 0 \\ u_{d,z} & v_{d,z} & w_{d,z} & 0 & 0 & 0 & u_{d,x} & v_{d,x} & w_{d,x} \\ 0 & 0 & 0 & u_{d,z} & v_{d,z} & w_{d,z} & u_{d,y} & v_{d,y} & w_{d,y} \end{bmatrix}, \tag{5.15}$$

$$\mathbf{A}_3 = -\frac{1}{2} \times \begin{bmatrix} 2u_{d,x} & 0 & 0 & v_{d,x} & w_{d,x} & 0 \\ 0 & 2v_{d,y} & 0 & u_{d,y} & 0 & w_{d,y} \\ 0 & 0 & 2w_{d,z} & 0 & u_{d,z} & v_{d,z} \\ 2u_{d,y} & 2v_{d,x} & 0 & u_{d,x} + v_{d,y} & w_{d,y} & w_{d,x} \\ 2u_{d,z} & 0 & 2w_{d,x} & v_{d,z} & u_{d,x} + w_{d,z} & v_{d,x} \\ 0 & 2v_{d,z} & 2w_{d,y} & u_{d,z} & u_{d,y} & v_{d,y} + w_{d,z} \end{bmatrix}, \tag{5.16}$$

where $\bar{\mathbf{B}} \in \mathbb{R}^{9\times n_e}$ and $\mathbf{u}^e \in \mathbb{R}^{n_e}$ are the shape function derivative matrix and elemental deformed-displacement vector of the 3D continuum finite element in n_e DOFs, respectively. $\mathbf{G} \in \mathbb{R}^{6\times 9}$ is the constant localization matrix. $\mathbf{A}_1$, $\mathbf{A}_2$, and $\mathbf{A}_3 \in \mathbb{R}^{6\times 9}$ are the displacement gradient matrices corresponding to the nominal configuration (e.g., $u_{,x} = \partial u/\partial x_0$ and $w_{d,y} = \partial w_d/\partial y_0$, by using Voigt notation), respectively.

While considering Eq. (5.16), the strain variation in the virtual work expression can be expressed as follows:

$$\begin{aligned} \delta\mathbf{E}_{f,N} &= (\mathbf{G} + \mathbf{A}_1 + \mathbf{A}_2 + 2\mathbf{A}_3\mathbf{A}_1)\bar{\mathbf{B}}\delta\mathbf{u}^e \\ &= \mathbf{B}\,\delta\mathbf{u}^e, \end{aligned} \tag{5.17}$$

where $\mathbf{B}$ is the strain-displacement matrix.

The element-level internal force from the virtual work of the FE-based representation can be written as follows:

$$\mathbf{f}_{int}^e = \int_{V_d^e} \mathbf{B}^T\mathbf{C}\mathbf{E}_{f,N}\mathrm{d}V_d^e, \tag{5.18}$$

where $\mathbf{C} \in \mathbb{R}^{6\times 6}$ is the constitutive matrix of the corresponding linear elastic

material and V_d^e is the element-level volume in the defected configuration.

By substituting Eqs. (5.12) and (5.17) into Eq. (5.18), the element-level internal force can be explicitly written as follows:

$$\begin{aligned}\mathbf{f}_{int}^{e} = \int_{V_d^e} \overline{\mathbf{B}}^{\mathrm{T}}(\mathbf{G} + \mathbf{A}_1 + \mathbf{A}_2 + 2\mathbf{A}_3\mathbf{A}_1)^{\mathrm{T}}\,\mathbf{C} \\ \left(\mathbf{G} + \frac{1}{2}\mathbf{A}_1 + \mathbf{A}_2 + \mathbf{A}_3\mathbf{A}_1\right)\overline{\mathbf{B}}\mathbf{u}^{e}\mathrm{d}V_d^e,\end{aligned} \tag{5.19}$$

Herein, to explicitly compute the stiffness coefficients of the internal force, the displacement gradient matrices can be rewritten as follows:

$$\mathbf{A}_1 = \mathbf{L}_1 \cdot (\overline{\mathbf{B}}\mathbf{u}^{e}), \tag{5.20}$$

$$\mathbf{A}_2 = \mathbf{L}_2 \cdot (\overline{\mathbf{B}}\mathbf{u}_d^{e}), \tag{5.21}$$

$$\mathbf{A}_3\mathbf{A}_1 = (\mathbf{L}_3 \cdot (\overline{\mathbf{B}}\mathbf{u}_d^{e})) \cdot (\overline{\mathbf{B}}\mathbf{u}^{e}), \tag{5.22}$$

where $\mathbf{L}_1, \mathbf{L}_2 \in \mathbb{R}^{6\times9\times9}$ and $\mathbf{L}_3 \in \mathbb{R}^{6\times9\times9\times9}$ are the constant localization matrices, whose detailed expression is provided in Appendix A.

Equation (5.19) can be divided into contributions that represent the linear, quadratic, and cubic terms for the displacement $\mathbf{u}^e$, as follows:

$$\mathbf{f}_{linear}^{e} = \int_{V_d^e} \overline{\mathbf{B}}^{T}\left(\mathbf{G}^{T}\mathbf{C}\mathbf{G} + \mathbf{G}^{T}\mathbf{C}\mathbf{A}_2 + \mathbf{A}_2{}^{T}\mathbf{C}\mathbf{G} + \mathbf{A}_2{}^{T}\mathbf{C}\mathbf{A}_2\right)\overline{\mathbf{B}}\mathbf{u}^{e}\mathrm{d}V_d^e, \tag{5.23}$$

$$\begin{aligned}\mathbf{f}_{quadratic}^{e} = \int_{V_d^e} \overline{\mathbf{B}}^{T}\Big(&\frac{1}{2}\mathbf{G}^{T}\mathbf{C}\mathbf{A}_1 + \mathbf{A}_1{}^{T}\mathbf{C}\mathbf{G} + \frac{1}{2}\mathbf{A}_2{}^{T}\mathbf{C}\mathbf{A}_1 + \mathbf{A}_1{}^{T}\mathbf{C}\mathbf{A}_2 \\ &+ 2\mathbf{A}_1{}^{T}\mathbf{A}_3{}^{T}\mathbf{C}\mathbf{G} + \mathbf{G}^{T}\mathbf{C}\mathbf{A}_3\mathbf{A}_1 + 2\mathbf{A}_1{}^{T}\mathbf{A}_3{}^{T}\mathbf{C}\mathbf{A}_2 \\ &+ \mathbf{A}_2{}^{T}\mathbf{C}\mathbf{A}_3\mathbf{A}_1\Big)\overline{\mathbf{B}}\mathbf{u}^{e}\mathrm{d}V_d^e,\end{aligned} \tag{5.24}$$

$$\mathbf{f}_{cubic}^{e} = \int_{V_d^e} \overline{\mathbf{B}}^T \left(\frac{1}{2} \mathbf{A}_1{}^T \mathbf{C} \mathbf{A}_1 + 2 \mathbf{A}_1{}^T \mathbf{A}_3{}^T \mathbf{C} \mathbf{A}_3 \mathbf{A}_1 + \mathbf{A}_1{}^T \mathbf{A}_3{}^T \mathbf{C} \mathbf{A}_1 + \mathbf{A}_1{}^T \mathbf{C} \mathbf{A}_3 \mathbf{A}_1 \right) \overline{\mathbf{B}} \mathbf{u}^e \mathrm{d}V_d^e. \tag{5.25}$$

These full-order terms will be expressed in the form of the following tensor relationships:

$$\mathbf{f}_{linear}^{e} = {}_2\mathbf{K}^e(\mathbf{u}_d^e) \cdot \mathbf{u}^e, \tag{5.26}$$

$$\mathbf{f}_{quadratic}^{e} = {}_3\mathbf{K}^e(\mathbf{u}_d^e) : (\mathbf{u}^e \otimes \mathbf{u}^e), \tag{5.27}$$

$$\mathbf{f}_{cubic}^{e} = {}_4\mathbf{K}^e(\mathbf{u}_d^e) \vdots (\mathbf{u}^e \otimes \mathbf{u}^e \otimes \mathbf{u}^e), \tag{5.28}$$

where

$${}_2\mathbf{K}^e(\mathbf{u}_d^e) = {}_{2n}\mathbf{K}^e + {}_{3d}\mathbf{K}^e \cdot \mathbf{u}_d^e + {}_{4dd}\mathbf{K}^e : (\mathbf{u}_d^e \otimes \mathbf{u}_d^e), \tag{5.29}$$

$${}_3\mathbf{K}^e(\mathbf{u}_d^e) = {}_{3n}\mathbf{K}^e + {}_{4d}\mathbf{K}^e \cdot \mathbf{u}_d^e + {}_{5dd}\mathbf{K}^e : (\mathbf{u}_d^e \otimes \mathbf{u}_d^e), \tag{5.30}$$

$${}_4\mathbf{K}^e(\mathbf{u}_d^e) = {}_{4n}\mathbf{K}^e + {}_{5d}\mathbf{K}^e \cdot \mathbf{u}_d^e + {}_{6dd}\mathbf{K}^e : (\mathbf{u}_d^e \otimes \mathbf{u}_d^e), \tag{5.31}$$

where the left-subscript of each tensor is its order. The letters "n" and "d" represent the tensor associated with only the nominal and defected geometry, respectively. Furthermore, "dd" indicates the higher tensor operand that is multiplied with the elemental defect-displacement vector $\mathbf{u}_d^e$ twice.

5.3 Reduced Tensors and Nonlinear Terms

To compute the reduced stiffness tensors, a suitable reduced basis $\mathbf{V} \in \mathbb{R}^{N\times m}$ $(m \ll N)$ and a set of displacement vectors $\mathbf{U} \in \mathbb{R}^{N\times m_d}$ that represent m_d predefined shape defects are designated. Then, elemental displacements $\mathbf{u}^e$ and $\mathbf{u}_d^e$ are approximated in a weighted linear combination of the set of basis vectors as follows:

$$\mathbf{u}^e \approx \mathbf{V}^e\boldsymbol{\eta}, \tag{5.32}$$

$$\mathbf{u}_d^e \approx \mathbf{U}^e\boldsymbol{\xi}, \tag{5.33}$$

where $\boldsymbol{\eta} \in \mathbb{R}^m$ and $\boldsymbol{\xi} \in \mathbb{R}^{m_d}$ are the reduced coordinate vector and defect amplitude vector, respectively. $\mathbf{V}^e \in \mathbb{R}^{n_e\times m}$ and $\mathbf{U}^e \in \mathbb{R}^{n_e\times m_d}$ are the element-level contributions of $\mathbf{V}$ and $\mathbf{U}$, respectively.

A reduced basis comprises three basis vectors via the following model-driven approaches: free vibration modes $\boldsymbol{\Phi}$, modal derivatives $\boldsymbol{\Theta}$, and defect sensitivities $\boldsymbol{\Xi}$ (i.e., $\mathbf{V} = [\boldsymbol{\Phi}, \boldsymbol{\Theta}, \boldsymbol{\Xi}]$), which can be directly obtained from the nominal FE representation.

Recalling Eqs. (2.7) and (2.14), the free vibration modes $\boldsymbol{\Phi}$ and modal derivatives $\boldsymbol{\Theta}$ are computed as follows:

$$\left(\mathbf{K}|_{eq} - \omega_i^2\mathbf{M}\right)\boldsymbol{\phi}_i = \mathbf{0}, \tag{5.34}$$

$$\boldsymbol{\theta}_{ij} = \left.\frac{\partial\boldsymbol{\phi}_i}{\partial\boldsymbol{\eta}_j}\right|_{eq} = -\mathbf{K}|_{eq}^{-1}\left.\frac{\partial\mathbf{K}_T\left(\boldsymbol{\phi}_j\boldsymbol{\eta}_j, 0\right)}{\partial\boldsymbol{\eta}_j}\right|_{eq}\boldsymbol{\phi}_i, \tag{5.35}$$

where

$$\left.\frac{\partial \mathbf{K}_T\left(\boldsymbol{\phi}_j \boldsymbol{\eta}_j, 0\right)}{\partial \boldsymbol{\eta}_j}\right|_{eq} = \int_{V_n} \overline{\mathbf{B}}^T \left(\mathbf{G}^T \mathbf{C} \mathbf{A}_1 + 2{\mathbf{A}_1}^T \mathbf{C} \mathbf{G}\right) \overline{\mathbf{B}} \mathrm{d}V_n, \tag{5.36}$$

where $\mathbf{K}|_{eq}$ represents tangent stiffness matrix $\mathbf{K}_T(\mathbf{u}, \mathbf{u}_d)$ at the equilibrium position $(\mathbf{u} = 0, \mathbf{u}_d = 0)$ ω_i and $\boldsymbol{\phi}_i$ are the i^{th} eigenvalue and its associated eigenvector, respectively. Moreover, the contribution of the spin-softening effect is considered for the rotating component (i.e., $\mathbf{K}|_{eq} = \mathbf{K}_T(0,0) - \mathbf{K}_{sp}$).

Analogous to the modal derivatives, the defect sensitivities $\boldsymbol{\Xi}$ can be obtained by differentiating the free vibration modes with respect to the defect amplitude, and are expressed as follows:

$$\boldsymbol{\Xi}_{ij} = \left.\frac{\partial \boldsymbol{\phi}_i}{\partial \boldsymbol{\xi}_j}\right|_{eq} = -\mathbf{K}|_{eq}^{-1} \left.\frac{\partial \mathbf{K}_T\left(0, \mathbf{U}_j \boldsymbol{\xi}_j\right)}{\partial \boldsymbol{\xi}_j}\right|_{eq} \boldsymbol{\phi}_i, \tag{5.37}$$

where

$$\left.\frac{\partial \mathbf{K}_T\left(0, \mathbf{U}_j \boldsymbol{\xi}_j\right)}{\partial \boldsymbol{\xi}_j}\right|_{eq} = \int_{V_n} \overline{\mathbf{B}}^T \left(\mathbf{G}^T \mathbf{C} \mathbf{A}_2 + {\mathbf{A}_2}^T \mathbf{C} \mathbf{G}\right) \overline{\mathbf{B}} \mathrm{d}V_n. \tag{5.38}$$

When a set of m_Φ free vibration modes and m_d shape defects are selected, $m_\Phi(m_\Phi + 1)/2$ modal derivatives and $m_d m_\Phi$ defect sensitivities are obtained. Consequently, m vectors of the reduced basis $\mathbf{V}$ correspond to $(3/2 + m_\Phi/2 + m_d)\, m_\Phi$ basis vectors. in the form of the following tensor relationships:

By substituting Eqs. (5.32) and (5.33) into (5.23) - (5.25), the elemental reduced tensors can be obtained along with Einstein's notation:

$${}_{2n}Q_{IJ}^e = \int_{V_d^e} \Gamma_{iI} G_{ji} C_{jk} G_{kl} \Gamma_{kJ} \mathrm{d}V_d^e, \tag{5.39}$$

$$ {}_{3n}Q^e_{IJK} = \int_{V_d^e} \Gamma_{iI}\left(\frac{1}{2}G_{ji}C_{jk}L_{1kla}\Gamma_{aK} + L_{1jia}\Gamma_{aK}C_{jk}G_{kl}\right)\Gamma_{lJ}\mathrm{d}V_d^e\,, \tag{5.40} $$

$$ {}_{3d}Q^e_{IJ\underline{K}} = \int_{V_d^e} \Gamma_{iI}\left(G_{ji}C_{jk}L_{2kla}\Upsilon_{aK} + L_{2jia}\Upsilon_{aK}C_{jk}G_{kl}\right)\Gamma_{lJ}\mathrm{d}V_d^e\,, \tag{5.41} $$

$$ {}_{4n}Q^e_{IJKL} = \frac{1}{2}\int_{V_d^e} \Gamma_{iI}L_{1jia}\Gamma_{aK}C_{jk}L_{1klb}\Gamma_{bL}\Gamma_{lJ}\mathrm{d}V_d^e\,, \tag{5.42} $$

$$ {}_{4d}Q^e_{IJK\underline{L}} = \int_{V_d^e} \Gamma_{iI}\begin{pmatrix}\frac{1}{2}L_{2jla}\Upsilon_{aL}C_{jk}L_{1klb}\Gamma_{bK}\\ +L_{1jia}\Gamma_{aK}C_{jk}L_{2klb}\Upsilon_{bL}\\ +2L_{3jiab}\Upsilon_{bL}\Gamma_{aK}C_{jk}G_{kl}\\ +G_{ji}C_{jk}L_{3klab}\Upsilon_{bL}\Gamma_{aK}\end{pmatrix}\Gamma_{lJ}\mathrm{d}V_d^e\,, \tag{5.43} $$

$$ {}_{4dd}Q^e_{IJ\underline{KL}} = \int_{V_d^e} \Gamma_{iI}L_{2Jla}\Upsilon_{aK}C_{jk}L_{2jia}\Upsilon_{bL}\Gamma_{lJ}\mathrm{d}V_d^e, \tag{5.44} $$

$$ {}_{5d}Q^e_{IJKL\underline{M}} = \int_{V_d^e} \Gamma_{iI}\begin{pmatrix}\frac{1}{2}L_{1jla}\Gamma_{aK}C_{jk}L_{3klbc}\Upsilon_{cM}\Gamma_{bL}\\ +L_{3jiab}\Upsilon_{bM}\Gamma_{aK}C_{jk}L_{1klc}\Gamma_{lL}\end{pmatrix}\Gamma_{lJ}\mathrm{d}V_d^e\,, \tag{5.45} $$

$$ {}_{5dd}Q^e_{IJK\underline{LM}} = \int_{V_d^e} \Gamma_{iI}\begin{pmatrix}2L_{3jiab}\Upsilon_{bL}\Gamma_{aK}C_{jk}L_{2klc}\Upsilon_{cM}\\ +L_{2jla}\Upsilon_{aL}C_{jk}L_{3klbc}\Upsilon_{cM}\Gamma_{bK}\end{pmatrix}\Gamma_{lJ}\mathrm{d}V_d^e\,, \tag{5.46} $$

$$ {}_{6dd}Q^e_{IJKL\underline{MN}} = 2\int_{V_d^e} \Gamma_{iI}L_{3jiab}\Upsilon_{bM}\Gamma_{aL}C_{jk}L_{3klcd}\Upsilon_{dN}\Gamma_{cK}\Gamma_{lJ}\mathrm{d}V_d^e\,, \tag{5.47} $$

where $\boldsymbol{\Gamma} = \bar{\mathbf{B}}\mathbf{V}^e$ and $\boldsymbol{\Upsilon} = \bar{\mathbf{B}}\mathbf{U}^e$ denote the projections of the shape function derivative matrix over the element-level bases. The right-subscript of each tensor is its dimensions. Accordingly, the capital letter represents *m* size (for the underlined one, m_d size), e.g., ${}_{6dd}\mathrm{Q}^e \in \mathbb{R}^{m\times m\times m\times m\times m_d\times m_d}$.

The global reduced tensor for each contribution can be obtained as the summation

over all element-level tensors:

$$ {}_{*}\mathbf{Q} = \sum_{e=1}^{N_e} {}_{*}\mathbf{Q}^{e}, \quad *= 2\mathrm{n}, 3\mathrm{n}, \ldots, 6\mathrm{dd}. \tag{5.48} $$

Herein, $*\mathbf{Q}e$ is computed over the nominal volume. If the volume changes due to defects, an approximated volume integration is considered to include the defect contribution [57].

Consequently, the reduced nonlinear internal force is defined as a polynomial representation comprising the global reduced tensor:

$$ \hat{\mathbf{f}}_{int} = \underbrace{{}_{2}\mathbf{Q}(\xi) \cdot \boldsymbol{\eta}}_{linear} + \underbrace{{}_{3}\mathbf{Q}(\xi) : (\boldsymbol{\eta} \otimes \boldsymbol{\eta})}_{quadratic} + \underbrace{{}_{4}\mathbf{Q}(\xi) \vdots (\boldsymbol{\eta} \otimes \boldsymbol{\eta} \otimes \boldsymbol{\eta})}_{cubic}, \tag{5.49} $$

where

$$ {}_{2}\mathbf{Q}(\xi) = {}_{2n}\mathbf{Q} + {}_{3d}\mathbf{Q} \cdot \boldsymbol{\xi} + {}_{4dd}\mathbf{Q} : (\boldsymbol{\xi} \otimes \boldsymbol{\xi}), \tag{5.50} $$

$$ {}_{3}\mathbf{Q}(\xi) = {}_{3n}\mathbf{Q} + {}_{4d}\mathbf{Q} \cdot \boldsymbol{\xi} + {}_{5dd}\mathbf{Q} : (\boldsymbol{\xi} \otimes \boldsymbol{\xi}), \tag{5.51} $$

$$ {}_{4}\mathbf{Q}(\xi) = {}_{4n}\mathbf{Q} + {}_{5d}\mathbf{Q} \cdot \boldsymbol{\xi} + {}_{6dd}\mathbf{Q} : (\boldsymbol{\xi} \otimes \boldsymbol{\xi}), \tag{5.52} $$

Herein, spin-softening matrix $\mathbf{K}_{sp}$ is added to ${}_{2n}\mathbf{Q}$ for the rotating component.

Similar to Eq. (5.49), the reduced tangent stiffness matrix is obtained as follows:

$$ \widehat{\mathbf{K}}_T = \frac{\partial \hat{\mathbf{f}}_{int}}{\partial \boldsymbol{\eta}} = {}_{2}\mathbf{Q}(\xi) + 2\,{}_{3}\mathbf{Q}(\xi) \cdot \boldsymbol{\eta} + 3\,{}_{4}\mathbf{Q}(\xi) : (\boldsymbol{\eta} \otimes \boldsymbol{\eta}). \tag{5.53} $$

It is worth noting that fast online computation can be achieved because the resulting reduced nonlinear terms (Eqs. (5.49) and (5.53)) have the same dimension as the reduced basis owing to the tensorial formulation. However, for a larger

dimensional nonlinear representation, reducing the high-order tensors up to the sixth-order will require extensive computational time and resources during the off-line stage. Mitigation of such computational load can be achieved via the hyper-reduction method.

5.4 Hyper-reduced Tensors and Nonlinear Terms

The hyper-reduction approach constructs the nonlinear terms only at a few optimally selected nodes or elements, which approximates the large number of nonlinear terms to reduce their dimension. Among the hyper-reduction methods, ECSW is considered suitable for FE-based structural applications, considering it directly approximates the reduced nonlinear terms while preserving the symmetric property [48]. Therefore, this thesis proposes the DpROM framework, including the ECSW method. The set of reduced high-order tensors are obtained by using only a small number of selected elements determined via ECSW. Consequently, the off-line expense for Eqs. (5.39) – (5.48) decreases substantially. The expression and computational procedure for the proposed DpROM are presented in this section.

Based on QM-based ECSW (Section 3.4), the global reduced tensor for each contribution, Eq. (5.48), can be approximated as the summation over the selected elements only.

$$ {}_{*}\mathbf{Q} \approx {}_{*}\mathbf{Q}_h = \sum_{e \in \tilde{\boldsymbol{E}}} W_e \left({}_{*}\mathbf{Q}^e \right), \quad *= \text{2n, 3n, ... ,6dd.} \tag{5.54} $$

where the letter "*h*" represents the hyper-reduced tensor via ECSW and W_e is the weight of each selected element e used to provide the optimal approximation of the global reduced tensor.

Using the hyper-reduced tensors, the hyper-reduced nonlinear terms are obtained as follows:

$$\hat{\mathbf{f}}_{int,h} = {}_2\mathbf{Q}_h(\xi)\cdot\boldsymbol{\eta} + {}_3\mathbf{Q}_h(\xi):(\boldsymbol{\eta}\otimes\boldsymbol{\eta}) + {}_4\mathbf{Q}_h(\xi)\vdots(\boldsymbol{\eta}\otimes\boldsymbol{\eta}\otimes\boldsymbol{\eta}), \tag{5.55}$$

$$\widehat{\mathbf{K}}_{t,h} = \frac{\partial\hat{\mathbf{f}}_{int,h}}{\partial\boldsymbol{\eta}} = {}_2\mathbf{Q}_h(\xi) + 2\,{}_3\mathbf{Q}_h(\xi)\cdot\boldsymbol{\eta} + 3\,{}_4\mathbf{Q}_h(\xi)(\boldsymbol{\eta}\otimes\boldsymbol{\eta}). \tag{5.56}$$

Figure 5.2 shows the proposed computational algorithm of the proposed DpROM framework, including the ECSW method. In the off-line stage, the nominal full-order representation in Eq. (2.1) and the defect field are specified first, and then the relevant reduced basis is extracted. Next, the hyper-reduction approach, i.e., ECSW, optimally selects the elements and their weights. Herein, the QM approach is employed to mitigate expensive off-line computations on the full nonlinear FE representation required for the ECSW training vector (the reduced internal force, Eq. (3.16)). Then, the hyper-reduced-order tensors ${}_*\mathbf{Q}_h$, which linearly contribute to the reduced internal force, are separately computed based on the selected elements and corresponding weights. Such QM-based ECSW would significantly reduce the off-line computational cost associated with handling the high-dimensional tensors required to build the existing DpROM.

Once the reduced basis $\mathbf{V}$ and hyper-reduced tensors ${}_*\mathbf{Q}_h$ are pre-computed in the off-line stage, the defect-parametric hyper-reduced-order representation is cheaply defined in polynomial form in the online stage. Then, the repeated static and dynamic simulations may be rapidly performed for the different defect amplitudes without going through the off-line stage process.

The following is worth noting in the proposed approach:

- The dimension of the resulting ROM and the existing DpROM is m (the size of the reduced basis). Thus, the online computational cost will be approximately the same for both approaches. However, the proposed DpROM will reduce the overall cost compared with the existing one via its low-cost off-line stage process.
- The reduced basis is selected conservatively, including $m_\Phi(m_\Phi+1)/2$ modal derivatives and $m_d m_\Phi$ defect sensitivities related to all m_Φ free vibration modes up to the higher-order. In other words, the size of the reduced basis $\mathbf{V}$ features a quadratic growth with respect to the free vibration modes. Considering the large amount of reduced basis vectors, this will affect both the off-line and online expense. To reduce the number of bases by pre-selecting only a few modal derivatives, several approaches [65, 85, 86] can be employed.
- If the defect parameter changes, the reduced mass $\widehat{\mathbf{M}}_d$ and damping $\widehat{\mathbf{C}}_d$ matrices can be computed over the defected configuration during the online stage. Additionally, for the rotating component, the centrifugal force vector and spin-softening matrix will also be considered based on the defected configuration. However, the computational cost of such terms may be small in the online execution, and hence, will be negligible.
- The proposed DpROM is built using the tensorial formulation based on a linear elastic material (i.e., a constant constitutive matrix $\mathbf{C}$). In case of a nonlinear elastic material, the higher-order stiffness tensors should be reformulated along with the tensorial expansion of the corresponding material property expression.

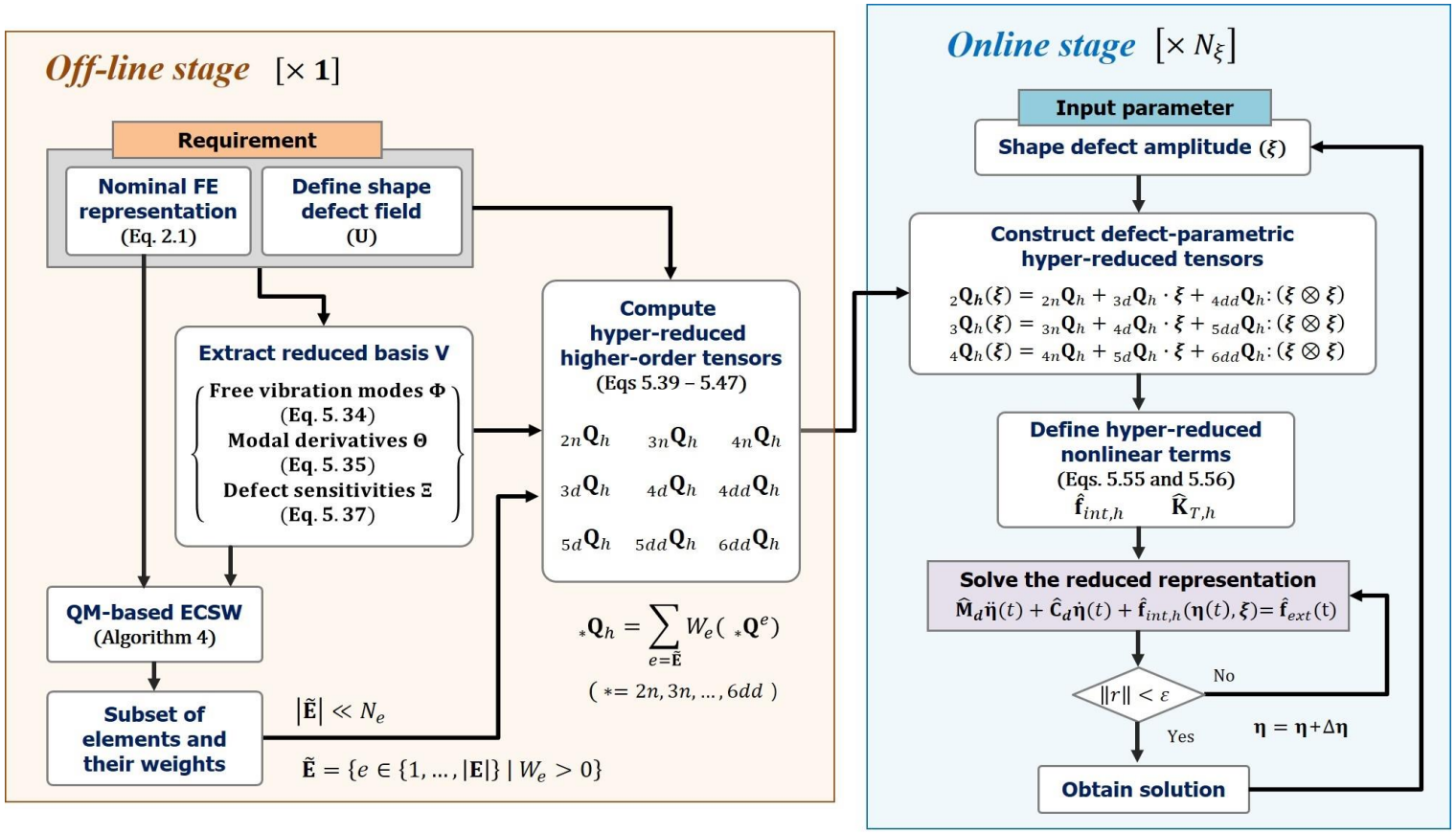

Fig. 5.2 Computational algorithm of the proposed DpROM framework in the off-line and online stages.

5.5 Numerical Results

5.5.1 Setup

Herein, the validity of the proposed DpROM framework will be evaluated by comparing the computational performance of the five different approaches when applied to the geometrically nonlinear simulation, including the shape defect. The relevant representations considered in this dissertation are as follows:

- **FOM-d**: The FOM with a shape defect involved by shifting the nominal FE discretization node locations. This will be a reference representation.
- **ROM-d**: The ROM in tensorial form is obtained via FOM-d. Its reduced basis comprises free vibration modes and modal derivatives computed over the defected configuration.
- **ROM-n**: The ROM in tensorial form is obtained via the nominal FE representation (i.e., no shape defect). Its reduced basis comprises free vibration modes and modal derivatives computed over the nominal configuration.
- **DpROM**: The DpROM in tensorial form is obtained via the nominal FE representation and the set of pre-defined displacement fields. Its reduced basis comprises free vibration modes, modal derivatives, and defect sensitivities computed over the nominal configuration. The reduced tensors are up to the sixth-order (Eq. (5.48)). This was previously proposed by [57].
- **DpHROM**: The proposed DpROM, proposed for the first time in this dissertation, based on hyper-reduced tensors, comprises up to the sixth-order

(Eq. (5.54)) obtained via QM-based ECSW. Its reduced basis will be identical to that of DpROM.

The aforementioned ROM frameworks are developed and implemented based on the open-source MATLAB package "*YetAnotherFEcode*" [87], which is a generic FE solver. All simulations are performed in MATLAB 2022a (compatible with MATLAB Tensor Toolbox [88]), using a single core Intel(R) i7-11700K @3.60 GHz and 128-GB RAM.

To evaluate the accuracy of the ROM, an index representing the relative displacement field discrepancy is introduced as follows:

$$EI(\%) = \frac{\sqrt{\sum_{i=1}^{n_s} \left\| \mathbf{u}_i^{FOM} - \mathbf{u}_i^{ROM} \right\|_2^2}}{\sqrt{\sum_{i=1}^{n_s} \left\| \mathbf{u}_i^{FOM} \right\|_2^2}} \times 100, \tag{5.57}$$

where $\mathbf{u}_i$ is the displacement vector for the i^{th} step of FOM-d or the ROMs, i.e., ROM-n ROM-d, DpROM, and DpHROM. n_s is the number of the time steps (for the time-transient analysis) or the number of the imposed frequencies (for the frequency response analysis). To compare the computational efficiency between FOM and ROM, the online speed-up factor S and the total speed-up factor S_{tot} are respectively defined as follows:

$$S = \frac{t^{FOM}}{t^{ROM}}, \qquad S_{tot} = \frac{n_{on} t^{FOM}}{n_{off} t_{off} + n_{on} t^{ROM}}, \tag{5.58}$$

where t^{FOM}, t^{ROM}, and t_{off} are the online computational time consumed for FOM-d and ROM, and the off-line stage ($t_{off} = 0$ for FOM-d), respectively. In

particular, t_{off} comprises the sum of the reduced basis extraction time and the reduced tensor computation time (for DpHROM, the element selection time is also added). n_{on} is the number of the online simulations and n_{off} refers to the number of the off-line terms constructed.

In the following numerical examples, the generalized-α method is used to perform the nonlinear time-transient analysis. The tolerance concerning the nonlinear force residual was set as $\epsilon \leq 10^{-6}$ for the converged solutions. For the proposed approach, the positive tolerance is set as the range $10^{-4} \leq \epsilon_{nnls} \leq 10^{-2}$, which was suggested in previous studies [48, 89] to select the set of elements $\tilde{\mathbf{E}}$ in QM-based ECSW.

5.5.2 Three-dimensional slender beam

The first example is a 3D slender beam clamped at both ends, similar to the one in [56]. The beam configuration, having length $l_x = 2m$, width $b_y = 0.2m$, and thickness $t_z = 0.05m$, is discretized into 20-node hexahedral elements with $N_e = 375$, and the corresponding number of the displacement DOFs is $N = 6,636$. A time varying force is applied to the central node. Furthermore, the imposed frequency ω is chosen as the average of the first and second natural frequencies of the undamped linear component to investigate the geometrically nonlinear behavior involving large displacements. Rayleigh damping is used as the structural damping determined from a modal damping factor of 0.5 % for the first two natural frequencies.

The single shape defect field $\mathbf{U} = [\mathbf{u}_d, \mathbf{v}_d, \mathbf{w}_d]^T$ is pre-defined as shifting the

vertical (z-direction) nominal FE discretization node location, given as follows:

$$\mathbf{w}_d(x,\xi) = \xi t_z \sin\left(\frac{\pi}{l_x}x\right), \tag{5.59}$$

and $\mathbf{u}_d = \mathbf{v}_d = 0$. Such displacement field represents the shallow-arch defect, and the defect amplitude $\xi = 1$ corresponds to the maximum displacement of $t_z\, m$ for $\mathbf{U}$. The relevant analysis condition is shown in Fig. 5.3.

Regarding the off-line stage, the reduced basis comprises the first five free vibration modes ($m_\Phi = 5$) and the corresponding modal derivatives $m_\Theta = m_\Phi(m_\Phi + 1)/2 = 15$, for a total of 20 reduced basis vectors. For DpROM and DpHROM, five defect sensitivities (derivatives of five free vibration modes with respect to the single shape defect) are additionally included for a total of 25 reduced basis vectors.

For DpHROM, the training dataset (i.e., time-varying displacement result) is obtained using the QM-based approach for over 200 time steps with a uniform timestep size of $\Delta t = T_0/50$. Herein, T_0 is the period of the harmonic force (i.e., $T_0 = 2\pi/\omega$). Then, 103 selected elements and associated weights are determined by the sparse NNLS with a tolerance of $\epsilon_{nnls} = 10^{-3}$, as shown in Fig. 5.4.

After the reduced tensors are constructed for each ROM in the off-line stage, a time-transient online simulation is performed for up to 1,000 time steps. The relevant simulation is carried out for each defect amplitude $\xi = \{0,\ 0.25, 0.5, 0.75, 1\}$, i.e., simulations for a total of five cases.

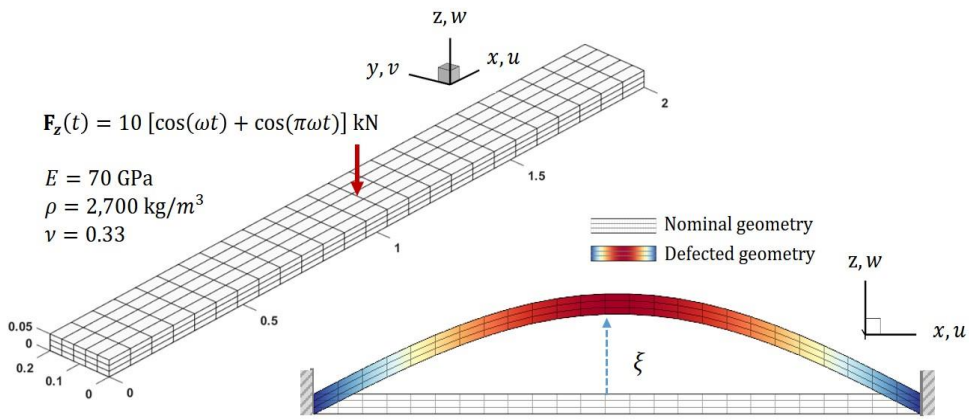

Fig. 5.3 Analysis condition of the 3D slender beam.

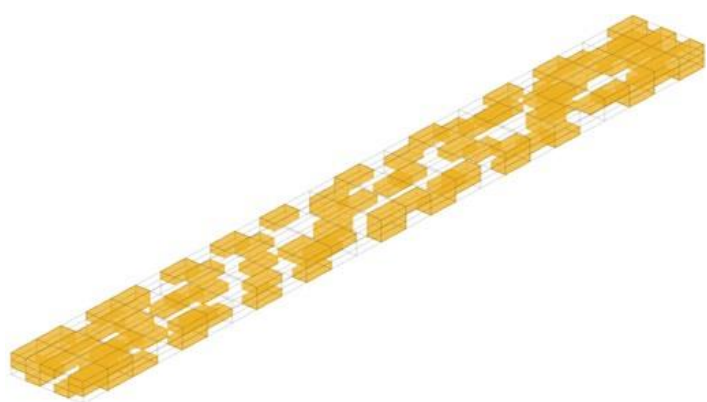

Fig. 5.4 Reduced number of meshes for the 3D slender beam (103 selected elements).

First, the vertical displacement history at a certain node is selected to evaluate the accuracy of the ROM. Fig. 5.5 compares the displacement history at that node and shows the maximal displacement between the FOM and ROM predictions. ROM-d, DpROM, and DpHROM are found to be in good agreement when compared to FOM-d. However, ROM-n yields an inaccurate solution owing to the defect. Then, the relative discrepancy is investigated. The relevant comparison is shown in Fig. 5.6. For all the cases, ROM-d, DpROM, and DpHROM achieve a significantly higher accuracy (the average relative discrepancy is within 2%). Conversely, ROM-n exhibits an unacceptable discrepancy even for a small defect amplitude. In addition, Fig. 5.7 illustrates a comparison of the von-Mises stress field at the time of maximum displacement (for a defect amplitude of $\xi = 1$). Both DpROM and DpHROM show good agreement when compared with the FOM-d prediction.

Next, to assess the accuracy and robustness of the proposed approach, the sensitivity analysis is performed with respect to a few numerical parameters.

Figure 5.8 compares the model accuracy in terms of the number of reduced basis vectors (for a defect amplitude of $\xi = 1$). In all ROMs except for ROM-n, it is observed that the accuracy tended to increase with the number of free vibration modes. When the number of free vibration modes is constant, DpHROM including defect sensitivities shows better accuracy than DpHROM without defect sensitivities. Specifically, when more than five free vibration modes and associated defect sensitivities are used, both DpROM and DpHROM build a robust reduced-order representation. Moreover, the QM-based ECSW of the proposed approach is

examined according to the choice of tolerance ϵ_{nnls}. Table 5.1 provides information regarding the number of selected elements and the corresponding relative discrepancy in terms of tolerance ϵ_{nnls}. As the tolerance ϵ_{nnls} decreases, a larger number of elements are selected, resulting in better accuracy. In particular, when the number of reduced basis is constant, even if the tolerance ϵ_{nnls} is smaller than 10^{-3}, a satisfactory accuracy is achieved with a relative discrepancy of approximately 2%. When considering the above two comparison results, the proposed approach achieves both improved accuracy and computational efficiency by selecting a proper reduced basis and tolerance ϵ_{nnls}.

The influence of the defect amplitude on accuracy is also investigated, as shown in Fig. 5.9. As the defect amplitude increases above unity, the accuracy of both DpROM and DpHROM tend to decrease. Such inaccuracy may be due to a deviation due to the small shape defect assumption ($\|\mathbf{H}_d\| \ll 1$). Therefore, quantitative bounds for the small defect hypothesis need to be further investigated. Finally, the computational cost based on the speed-up factor S and S_{tot}, Eq. (5.58), is investigated. Table 5.2 summarizes the corresponding comparison.

The online speed-up factor S is found to be remarkably high considering that the online time required for time integration depends only on the reduced basis dimension owing to the explicit tensorial form. In particular, ROM-d demonstrates an improved speed-up factor compared to DpHROM, which includes additional basis vectors, the defect sensitivities, and the reduced basis. However, considering the total speed-up factor S_{tot} including the off-line time, both DpROM and

DpHROM yield a higher computational efficiency as the off-line cost for the reduced tensors is required once. Conversely, ROM-d requires a repeated off-line cost whenever the defect amplitude changes, as shown in Fig. 5.10.

Additionally, it is worth noting that DpHROM achieves a significant reduction in terms of the off-line cost compared to both ROM-d and DpROM owing to the application of ECSW, which computes the reduced higher-order tensors by using only selected elements, as shown in Fig. 5.11. Furthermore, DpHROM is more computationally efficient for a larger-dimensional representation.

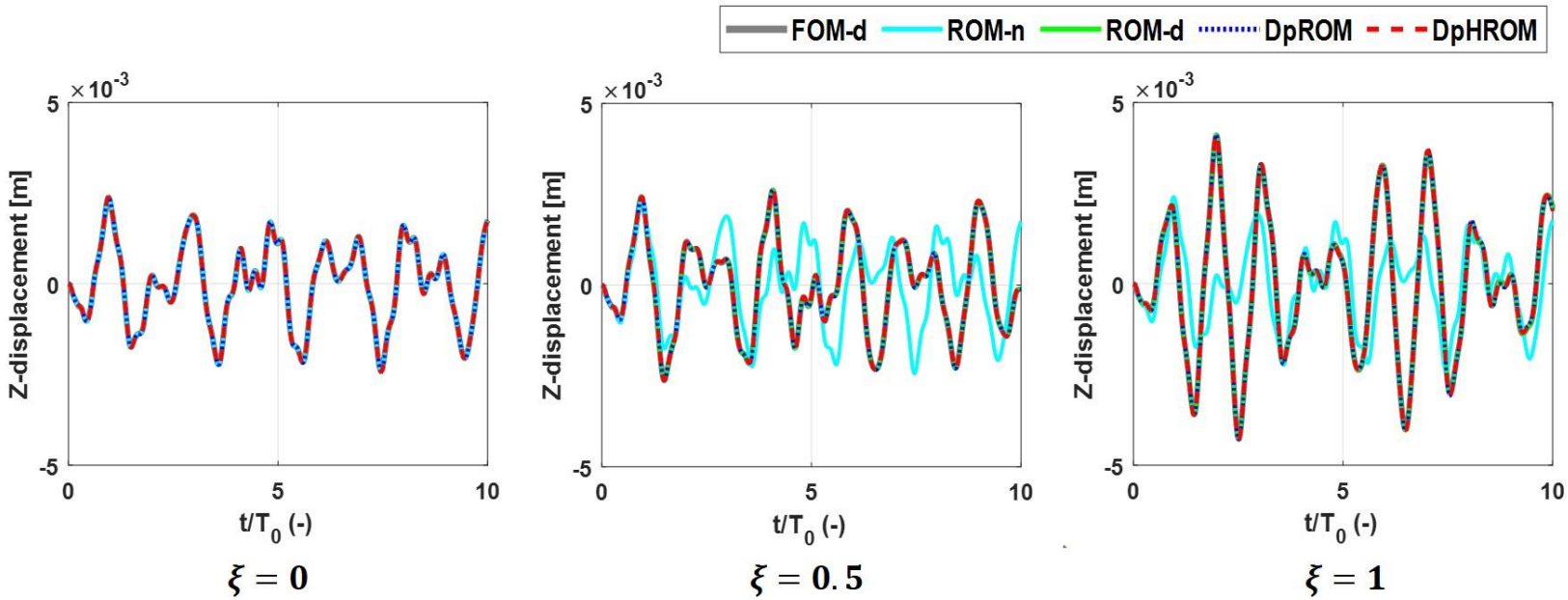

Fig. 5.5 Comparison of the displacement history at the maximal displacement location for the 3D slender beam.

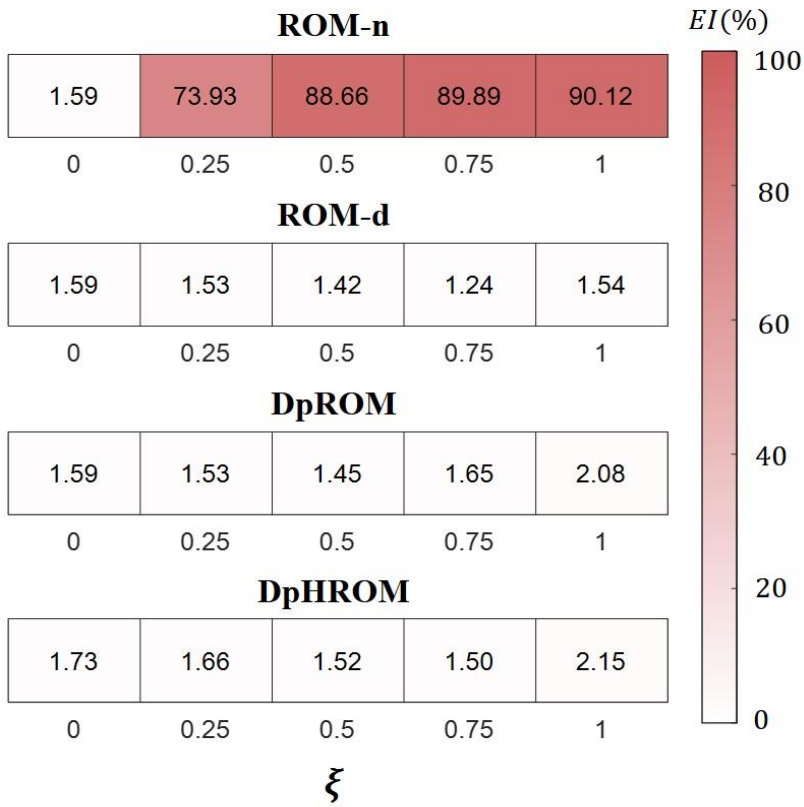

Fig. 5.6 Comparison of the relative discrepancy for the 3D slender beam.

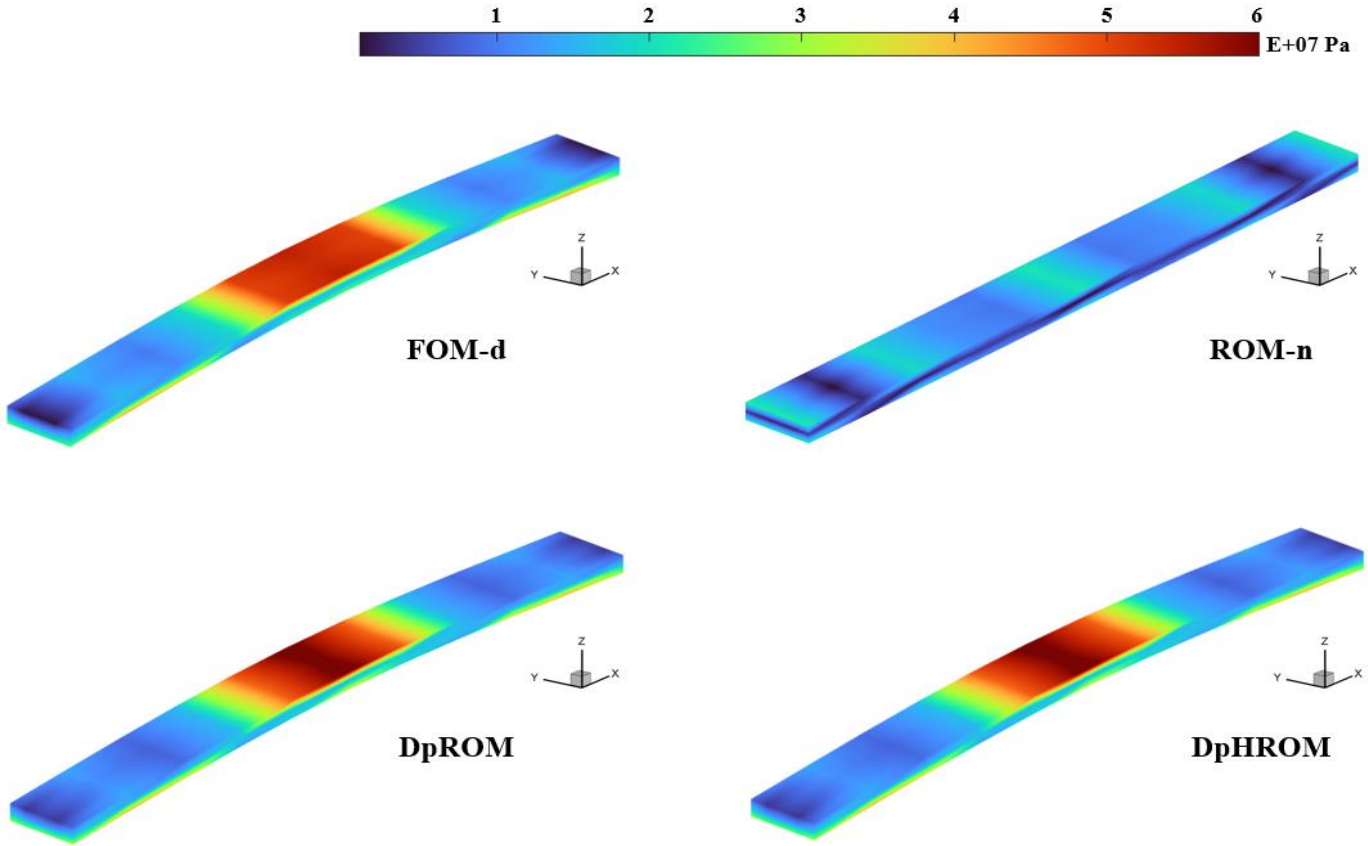

Fig. 5.7 von-Mises stress comparison at the time of the maximum displacement.

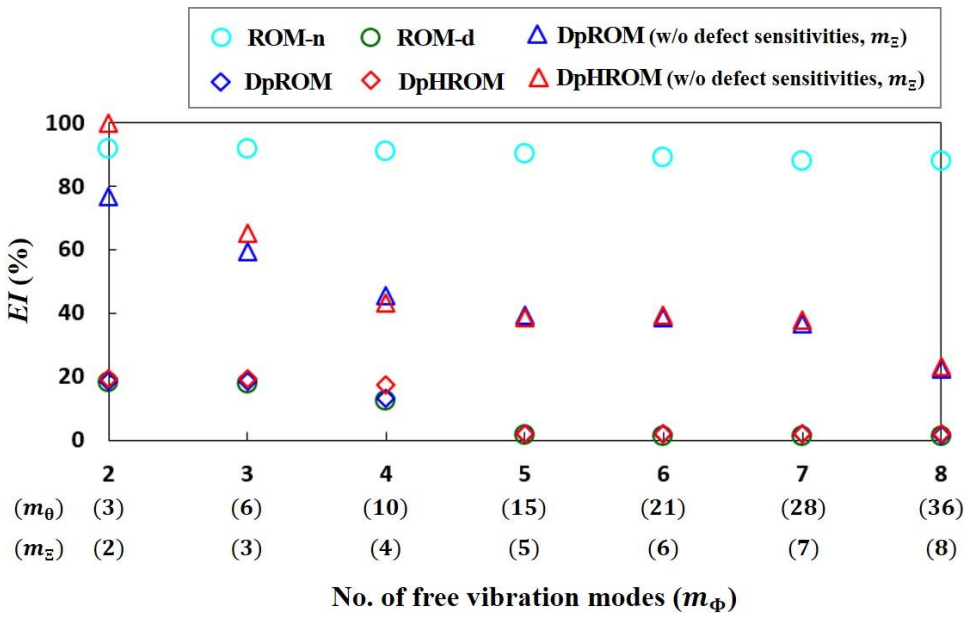

Fig. 5.8 Relative discrepancy comparison in terms of the number of the reduced basis vectors.

Table 5.1 Comparison between the selected elements and the relative discrepancy in terms of the tolerance ϵ_{nnls}.

ϵ_{nnls}	10^{-1}	10^{-2}	10^{-3}	10^{-4}	10^{-5}
$\lvert\tilde{\mathbf{E}}\rvert$	37	77	103	142	178
EI (%)	100.45	35.25	2.15	1.85	1.66

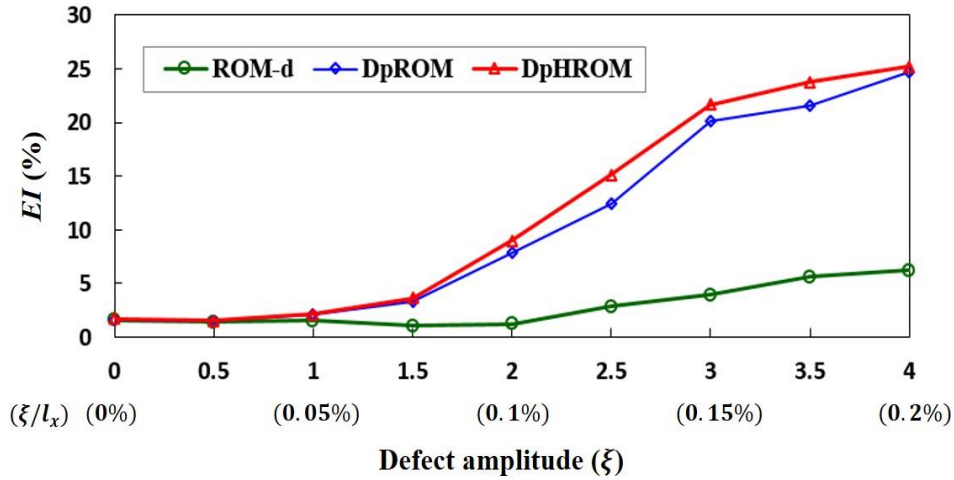

Fig. 5.9 Relative discrepancy comparison in terms of the defect amplitude ($\boldsymbol{\xi/l_x}$ indicates the shape defect to beam length ratio).

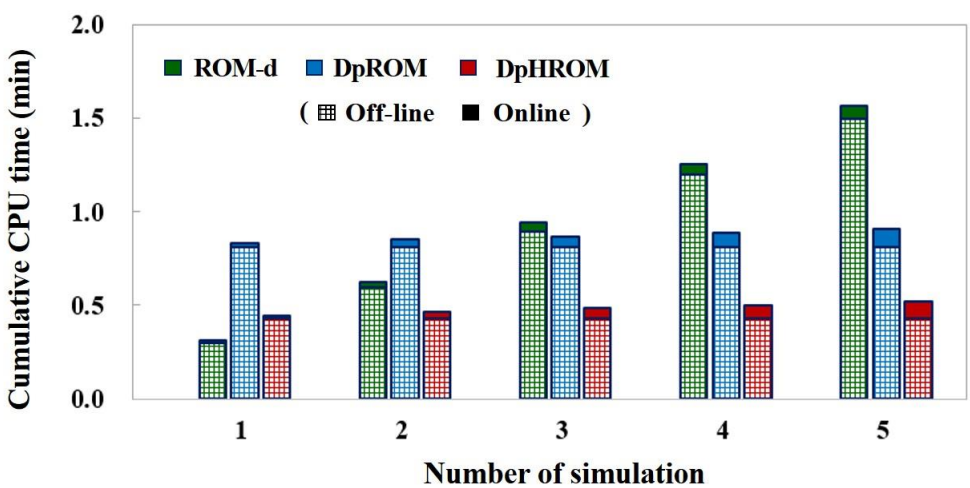

Fig. 5.10 Computational time comparison among ROMs.

Table 5.2 Computational expense between FOM and ROMs for the 3D slender beam

Model	Off-line [s]			Online [s]	n_{off}	n_{on}	Total time [s]	S	S_{tot}
	Reduced basis	QM-ECSW	Tensors						
FOM-d	-	-	-	791	-	5	3,955	-	-
ROM-d	5.1	-	12.8	2.9	5	5	94.1	909.2	42.1
DpROM	6.5	-	48.8	3.6	1	5	54.3	719.1	72.9
DpHROM	6.5	35.25	12.3	3.6	1	5	31.2	719.1	127

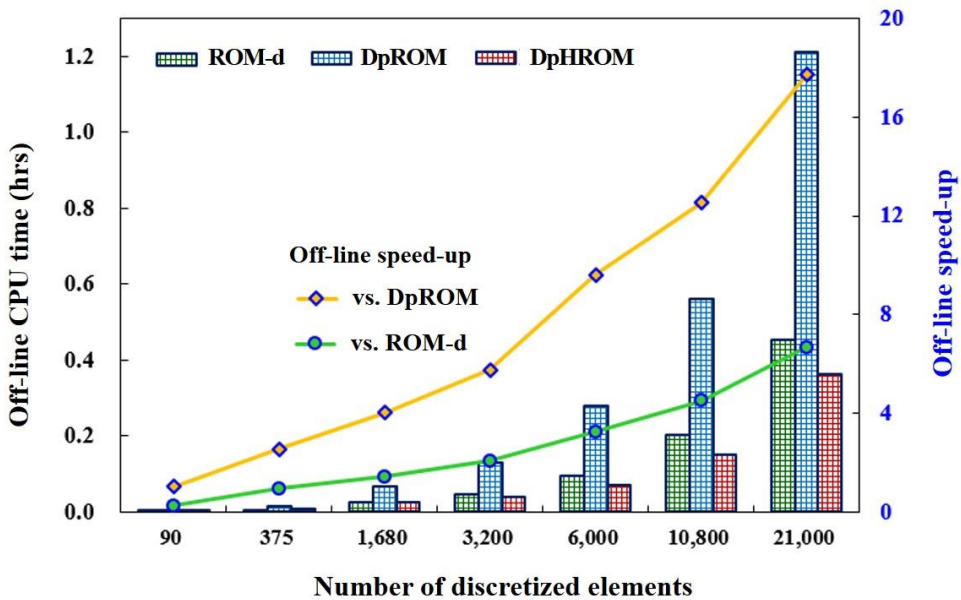

Fig. 5.11 Off-line cost in terms of the number of discretized elements.

5.5.3 54H60 propeller blade

Turbomachinery rotating blades may exhibit geometric imperfections owing to the presence of the manufacturing defect or potential damage during operation (e.g., resonant vibration or bird strikes). Therefore, a numerical study is conducted to validate whether the proposed DpROM is capable of considering the influence of probable shape imperfections on a rotating blade. A 54H60 propeller blade of a C-130H transport aircraft, which has a slender and twisted-surfaced configuration with a high aspect ratio, is taken as an example. The relevant configuration and analysis condition are shown in Fig. 5.12. The blade configuration is discretized using 24,151 quadratic tetrahedral elements with 133,857 DOFs. The inner surface of the blade hub is clamped, and the harmonic excitation is applied to all nodes of the tip surface, at a constant rotational speed of 1,050 rpm. Herein, the imposed frequency ω is chosen as the first natural frequency to induce a high degree of geometric nonlinearity. The material properties corresponds to 7,000 series aluminum alloys with a Rayleigh damping mass matrix multiplier of 50 s^{-1}.

The defect-displacement field is pre-defined as the linear superposition of two shape defects: twist and bending, i.e., $\mathbf{U} = [\mathbf{U}_1, \mathbf{U}_2]$ with their amplitude parameter vectors $\boldsymbol{\xi} = [\boldsymbol{\xi}_1, \boldsymbol{\xi}_2]^T$. The first twist-shape defect $\mathbf{U}_1 = [\mathbf{u}_{d1}, \mathbf{v}_{d1}, \mathbf{w}_{d1}]^T$ (Fig. 5.13-a) is defined as follows:

$$u_{d1}(x, y, z, \xi_1) = \xi_1 r \sin\left(\arctan(x, z) + \theta_t \left(\frac{y - \tilde{y}}{L - \tilde{y}}\right)\right), \tag{5.60}$$

$$w_{d1}(x, y, z, \xi_1) = \xi_1 r \cos\left(\arctan(x, z) + \theta_t\left(\frac{y - \tilde{y}}{L - \tilde{y}}\right)\right), \tag{5.61}$$

where $\tilde{y} \leq y \leq L$ and $v_{d1} = 0$. r and θ_t are the nodal positions converted to polar coordinates representing the radial distance from the rotation axis and pre-twist angle (set to be 1°), respectively. $\tilde{y}$ is y-coordinate corresponding to the beginning of the twist-defect at 40% in the span-wise position from the propeller blade hub.

The second bending-shape defect $\mathbf{U}_2 = [\mathbf{u}_{d2}, \mathbf{v}_{d2}, \mathbf{w}_{d2}]^T$ (Fig. 5.13-b) is given as follows:

$$w_{d2}(y, \xi_2) = \xi_2 0.01c\left(\frac{y - \tilde{y}}{L}\right), \tag{5.62}$$

and $u_{d2} = v_{d2} = 0$.

For all ROMs, the reduced basis is selected by the first seven free vibration modes and the corresponding 28 modal derivatives for a total of 36 reduced basis vectors. However, in for DpROM and DpHROM, 14 defect sensitivities (derivatives of the seven free vibration modes with respect to each shape defect) are additionally included for a total of 49 reduced basis vectors.

For DpHROM, the QM-based training dataset is generated for up to 0.2 s (200 time steps with Δt = 0.001), and a set of selected elements $\tilde{\mathbf{E}}$ is obtained by the sparse NNLS with a tolerance of $\epsilon_{nnls} = 10^{-4}$, as shown in Fig. 5.14.

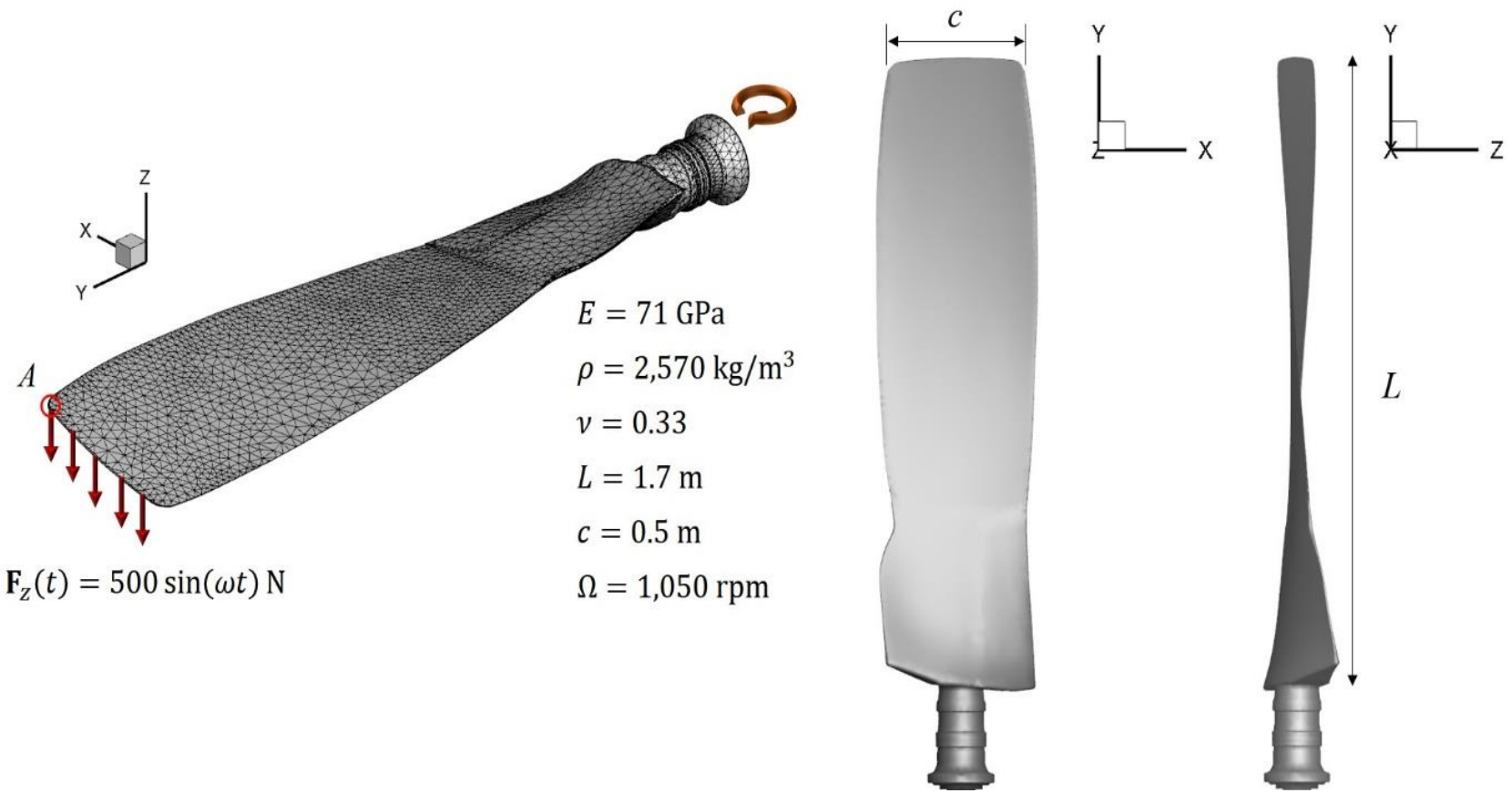

Fig. 5.12 Configuration and analysis condition for the 54H60 propeller blade.

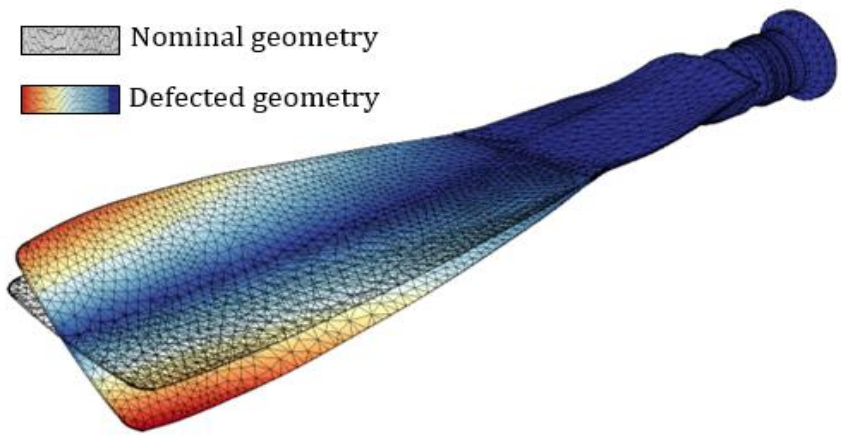

(a) First defect, U_1: twist

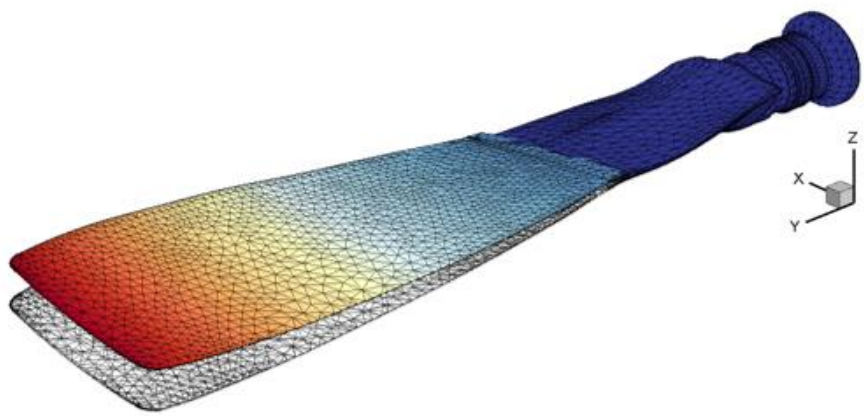

(b) Second defect, U_2: bending

Fig. 5.13 Shape defects for the 54H60 propeller blade

(the color map indicates the total displacement).

Fig. 5.14 Reduced number of meshes for the 54H60 propeller blade (166 selected elements)**.**

In this example, an on-line simulation will be executed in both the time- and frequency domains. First, a nonlinear time-transient simulation was conducted for up to 1 s (1,000 time steps). The simulation was carried out for each defect amplitude selected by combining $\xi_1 = \{-3,\ -1.5, 0, 1.5\ 3\}$ and $\xi_2 = \{-1,\ -0.5, 0, 0.5\ 1\}$, i.e., the simulation is conducted for a total 25 cases.

The total deformation history at the blade-tip surface is evaluated to assess the ROM accuracy. The total deformation was defined as follows:

$$\mathbf{u}_i^{tot} = \sqrt{\left(\mathbf{u}_{x,i}\right)^2 + \left(\mathbf{u}_{y,i}\right)^2 + \left(\mathbf{u}_{z,i}\right)^2}, \qquad i \in \mathbf{N}_{tip}, \tag{5.63}$$

where $\mathbf{N}_{tip}$ and $\mathbf{u}_{x,i}$ are the list of nodes on the tip surface and displacement component in the x-direction at the i^{th} node (same for $\mathbf{u}_{y,i}$ and $\mathbf{u}_{z,i}$), respectively.

Figure 5.15 compares the total deformation history for the different defect conditions. Both DpROM and DpHROM exhibit a satisfactory correlation with the FOM-d prediction. In addition, the relative discrepancy EI is considered. As shown in Fig. 5.16, both DpROM and DpHROM yield a high accurate solution for all cases (average relative discrepancy is within 5%). However, ROM-n shows a reduced displacement accuracy when the defect amplitude increased. In particular, the relative discrepancy increases as the amplitude of the bending-defect ξ_2 increases, whose direction corresponded to the first (bending) mode of the propeller blade. Furthermore, to evaluate the discrepancy at Point A (trailing edge at the blade tip) where the dominant shape defect occurs, the local error $\epsilon_u(t)$ is computed by $\left\|\mathbf{u}_A^{FOM} - \mathbf{u}_A^{ROM}\right\|$. Figure 5.17 shows a comparison of the local error history at Point

A. As shown in the figure, DpHROM exhibits a good accuracy, similar to ROM-d and DpROM.

Next, a frequency response analysis is conducted to obtain the steady-state displacement within a specific frequency range. The rotating component is subjected to the sinusoidal load in the resonant condition, resulting in high cycle fatigue. Therefore, the frequency response analysis was useful for predicting its vibration characteristics. The relevant procedure for the rotating component is realized by conducting nonlinear static- and linear frequency response analyses in sequence. In particular, the stiffness variation, that is, the stress-stiffening and spin-softening effect, is evaluated from the nonlinear static solution owing to the centrifugal force. For the linear frequency response analysis, a transverse tip harmonic force of 500 N is imposed using the frequency band ranging from 0–200 Hz at 1-Hz intervals.

The online simulation is executed for 50 defect cases to examine the performance of the ROM within broad parametric variations. The set of defect parameter vectors $\boldsymbol{\xi} = [\xi_1, \xi_2]^T$ are chosen randomly from $\xi_{1,2} \in [0, 1]$, which is generated using the Latin hypercube sampling method [90], as shown in Fig. 5.18-a. The reduced basis and reduced tensors are similar to those used in the time-transient simulation, without going through the off-line stage. Fig. 5.18-b shows the relative discrepancy EI of the displacement field between FOM and ROMs. In all cases, the relevant discrepancies are observed to be within 2 %, except for ROM-n. In particular, the maximum transverse displacement is demonstrated for the different cases, as shown in Fig. 5.19. Depending on the defect parameter, slight deviations are observed owing to the peak

location and corresponding displacement responses, thereby indicating that the shape defect for the rotating component will vary based on the underlying system (i.e., $\mathbf{K}_T$, $\mathbf{M}_d$, and $\mathbf{C}_d$) and the centrifugal force, which will affect their vibration characteristics. Additionally, the maximum von-Mises stress obtained from the alternating stress, which plays an important role for the fatigue prediction of the turbomachinery component, is investigated. Figure 5.20 illustrates a comparison of von-Mises stress field at 150 Hz, where large structural oscillation occurs for Case #31. DpHROM is observed to be in good agreement when compared with the FOM-d prediction. Moreover, as shown in Table 5.3, DpHROM yields an accurate solution at the peak stress location, similar to ROM-d and DpROM (with a relative discrepancy within 3%).

Finally, the computational cost during the off-line and online stages is compared to evaluate the computational efficiency, as summarized in Table 5.4. Among the ROMs, DpROM shows the largest off-line time considering it performs the time-consuming computation of reduced high-order tensors using the entire FE discretization. Therefore, parallel computing might be considered for such larger dimensional off-line DpROM computations, as shown in [56]. Conversely, DpHROM exhibits a significant improvement in terms of the off-line time (34 times faster than DpROM). Figure 5.21 compares the total speed-up factor, including the off-line cost, among the ROMs. Unlike ROM-d, DpHROM off-line time is required once at the beginning of the computation. Then, the online time is accumulated for the total computational cost. Therefore, the total computational cost in the proposed

DpHROM framework is expected to improve as similar computations (n_{on}) are repeated. In particular, DpHROM, which has a noticeably larger total speed-up factor compared to other ROMs, will be significantly efficient for large-size dynamic simulation with broad defect-parametric variations.

Sections of this chapter have been published in the following relevant journal articles:

Kim, Y., Kang, S., Song, D., Cho, H., and Shin, S.-J., "Efficient Nonlinear Dynamic Analysis of a Rotating Blade with Shape Defects," GPPS paper 2022-0139, September. 2022.

Kim, Y., Kang, S., Cho, H., Kim, H., and Shin, S.-J., "Parametric Reduced-order Modeling Enhancement for a Geometrically Imperfect Component via Hyper-reduction," *Computer Methods in Applied Mechanics and Engineering*, published online, October. 2022.

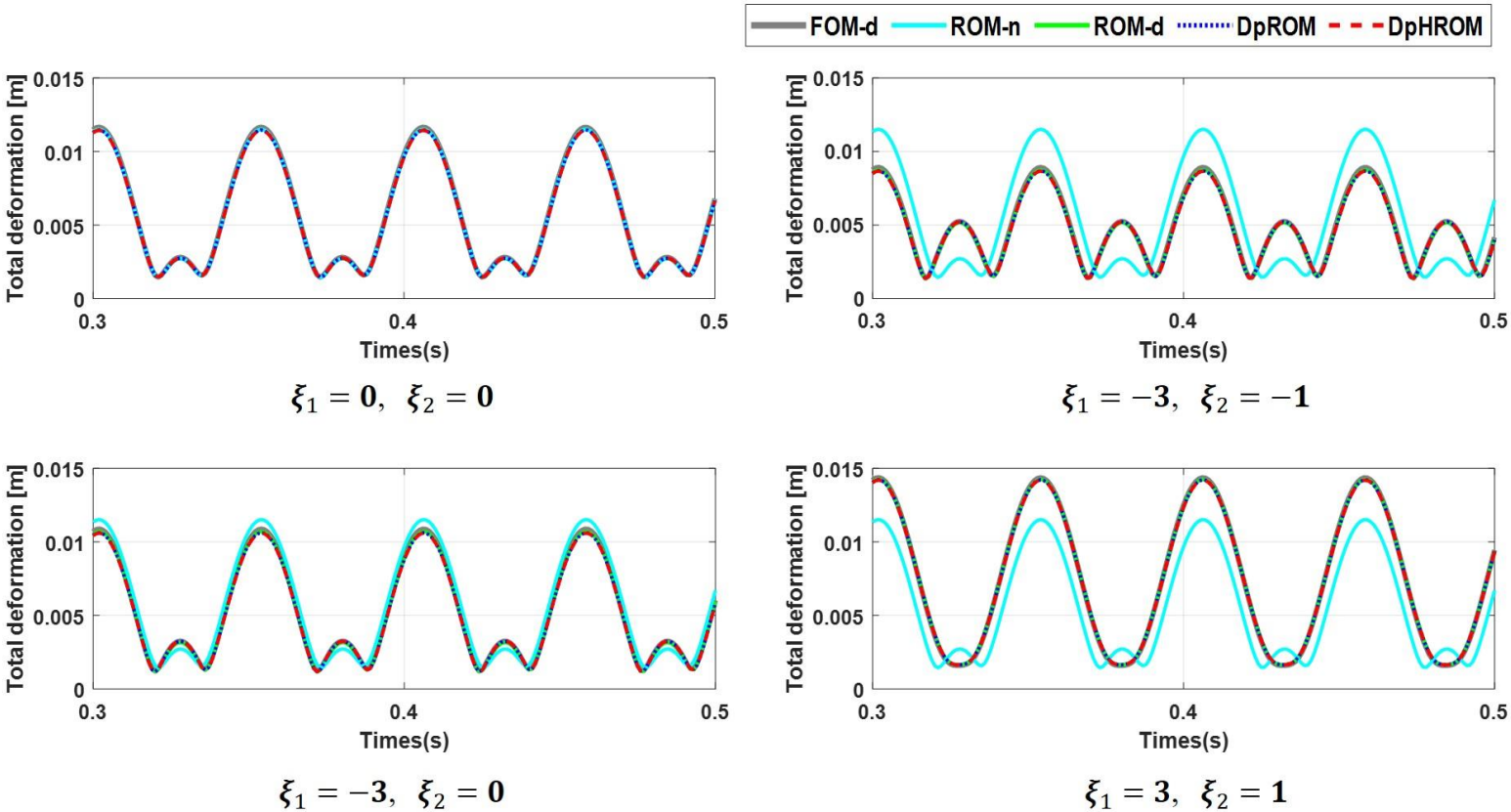

Fig. 5.15 Total deformation comparison for the different defect conditions.

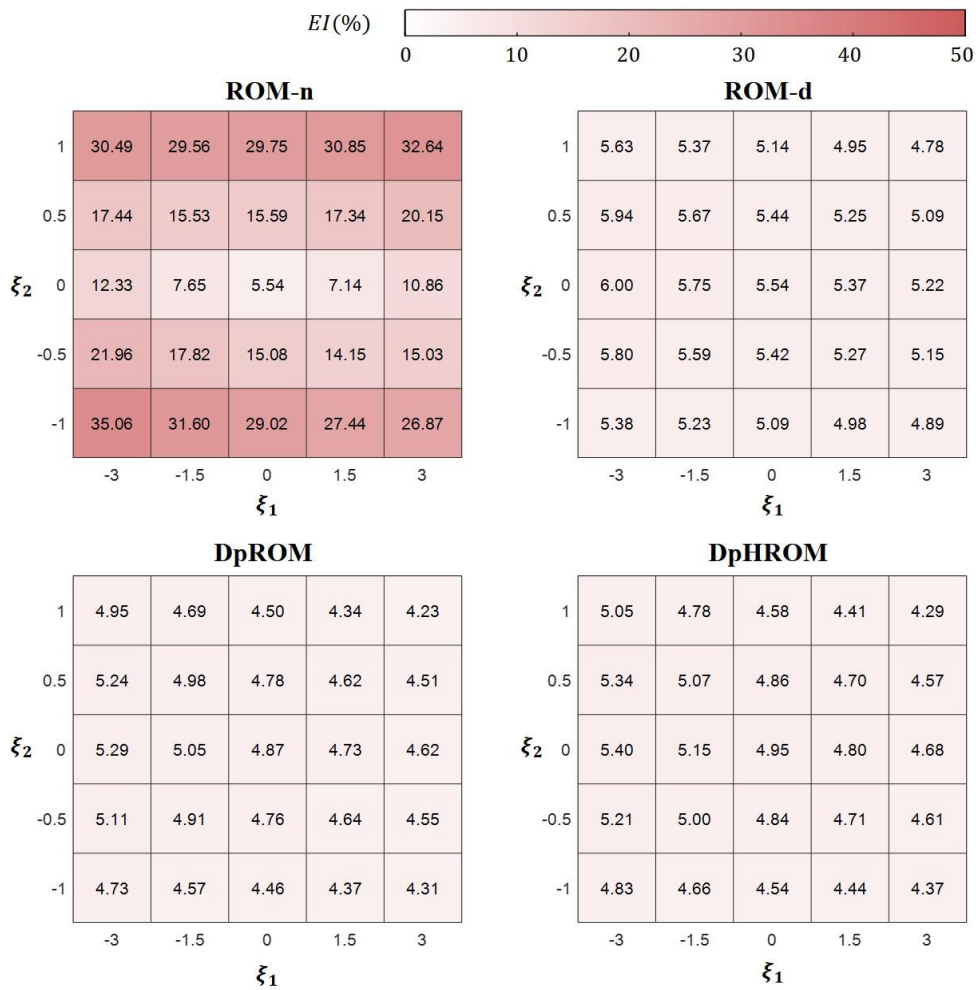

Fig. 5.16 Relative discrepancy comparison for the 54H60 propeller blade.

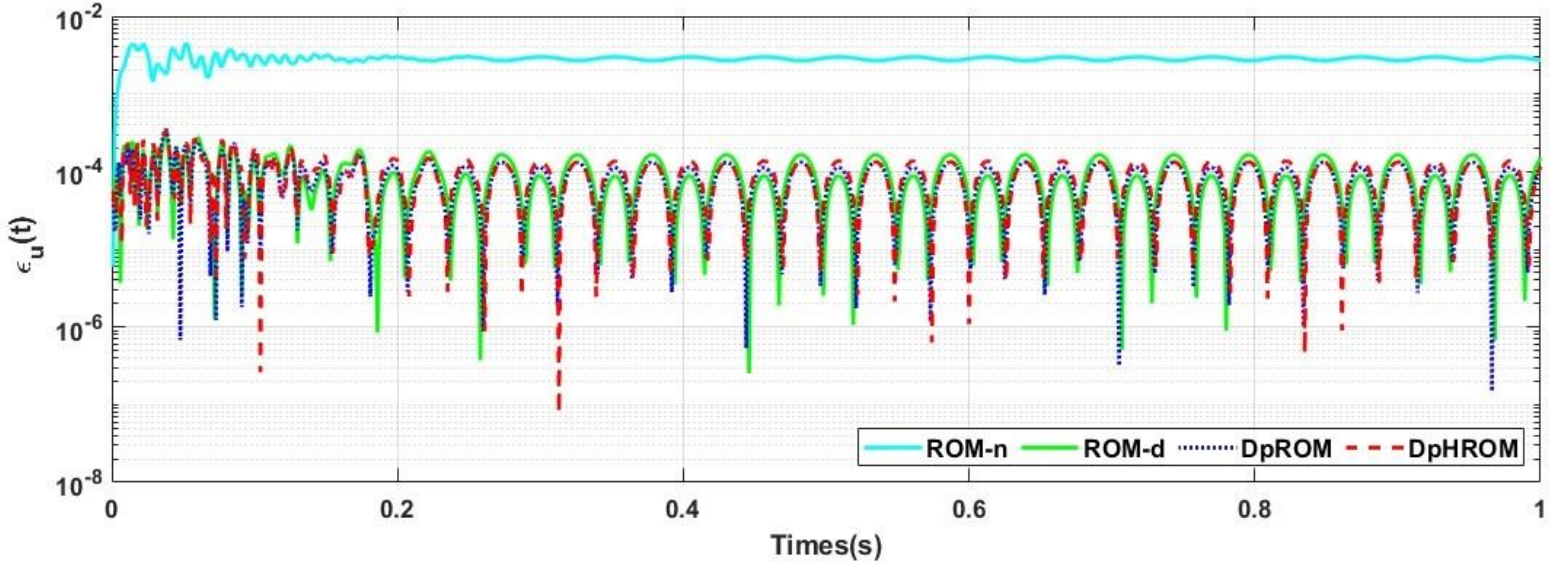

Fig. 5.17 Displacement field difference between FOM and ROM prediction

($\boldsymbol{\xi_1 = 3}$ and $\boldsymbol{\xi_2 = 1}$).

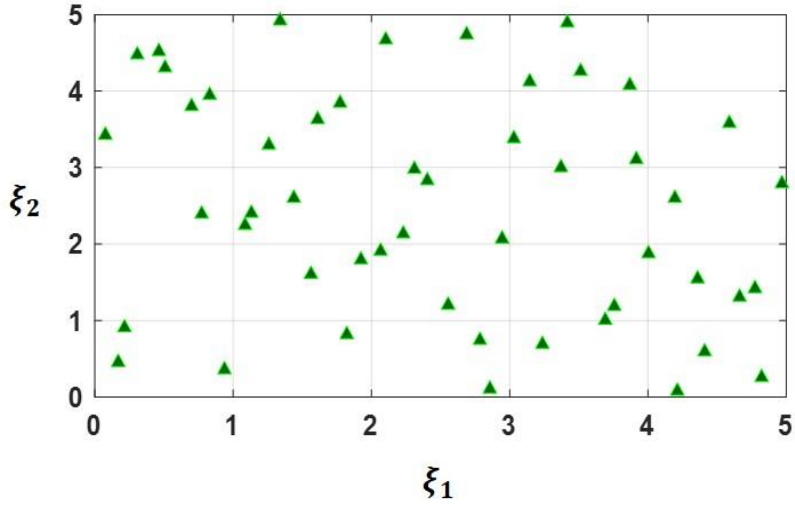

(a) Fifty sets of the defect parameters

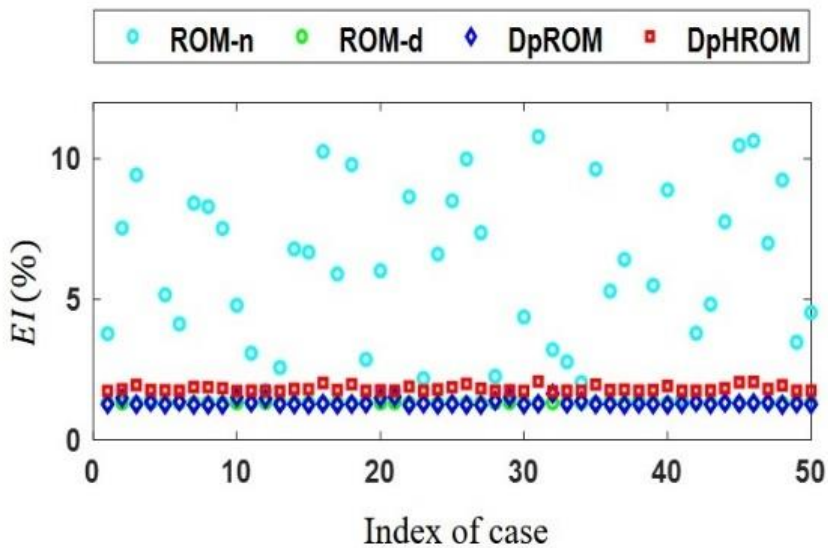

(b) Relative discrepancy

Fig. 5.18 Frequency response simulation for the 54H60 propeller blade within the parametric variation.

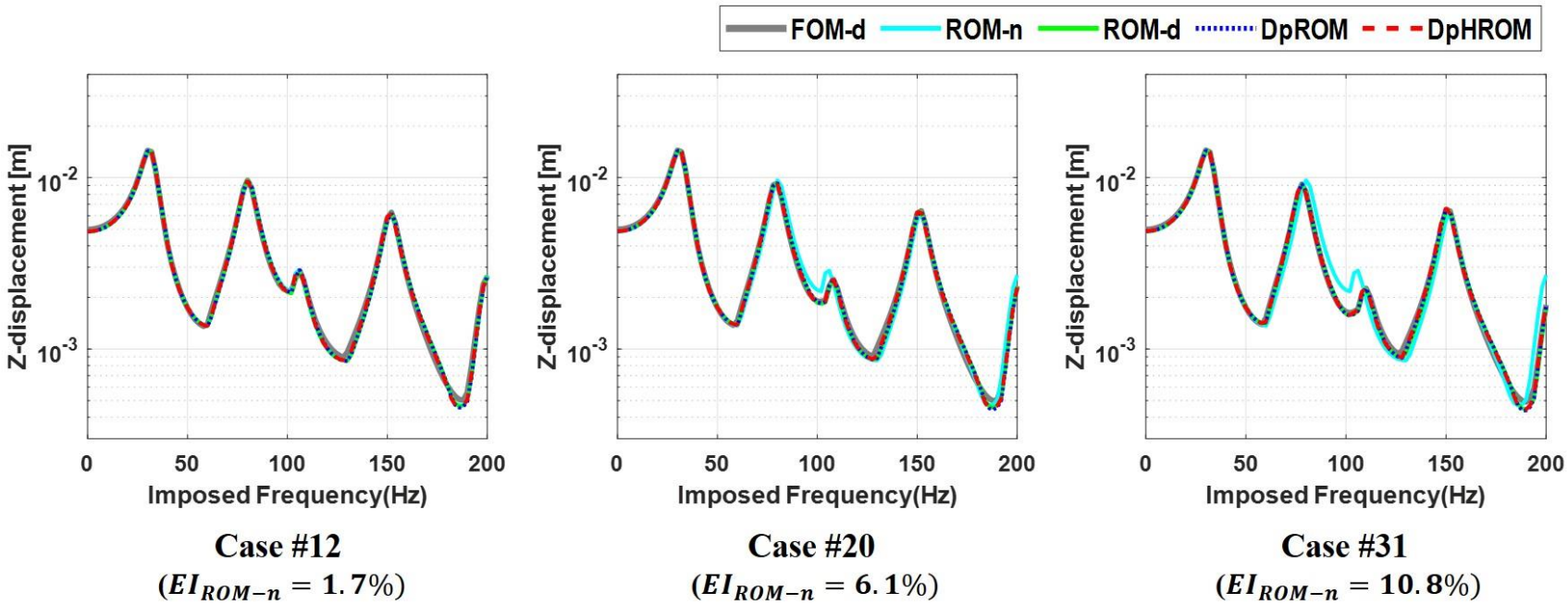

Fig. 5.19 Maximum transverse displacement amplitude for the different cases.

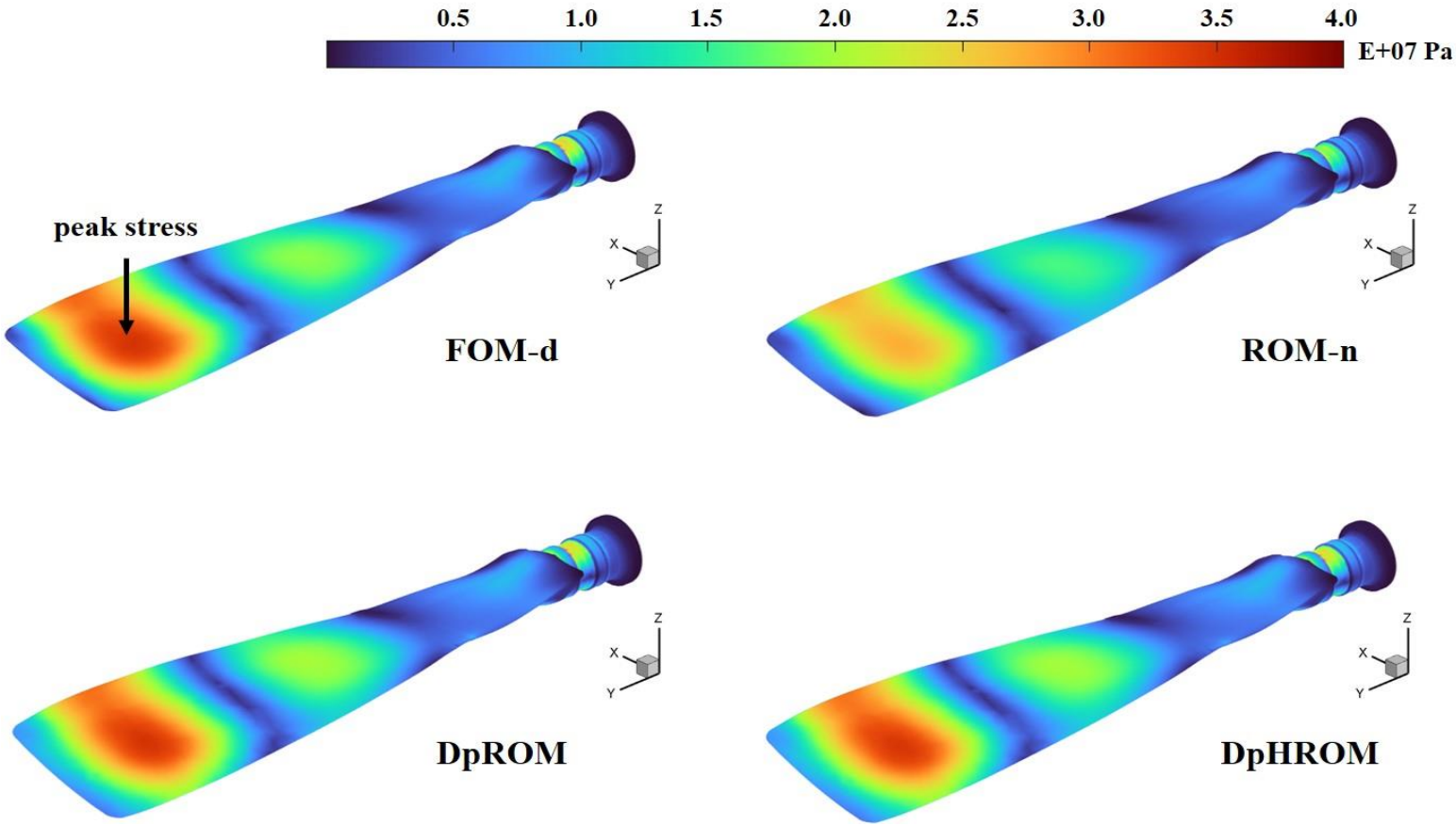

Fig. 5.20 von-Mises stress comparison (150 Hz, Case #31)**.**

Table 5.3 Relative discrepancy comparison at the peak von-Mises stress location (150 Hz, Case #31).

	ROM-n	ROM-d	DpROM	DpHROM
EI (%)	19.51	2.65	2.72	2.88

Table 5.4 Computational cost for the off-line and online stages for the 54H60 propeller blade

	Model	FOM-d	ROM-d	DpROM	DpHROM
Off-line [min]	Reduced basis	-	5.5	6.2	6.2
	QM-ECSW	-	-	-	4.4
	Tensors	-	21.9	587.8	6.9
Online [min] * *for a single execution*	Time-transient	310.7	0.19	0.34	0.34
	Frequency response	20.3	0.07	0.09	0.09

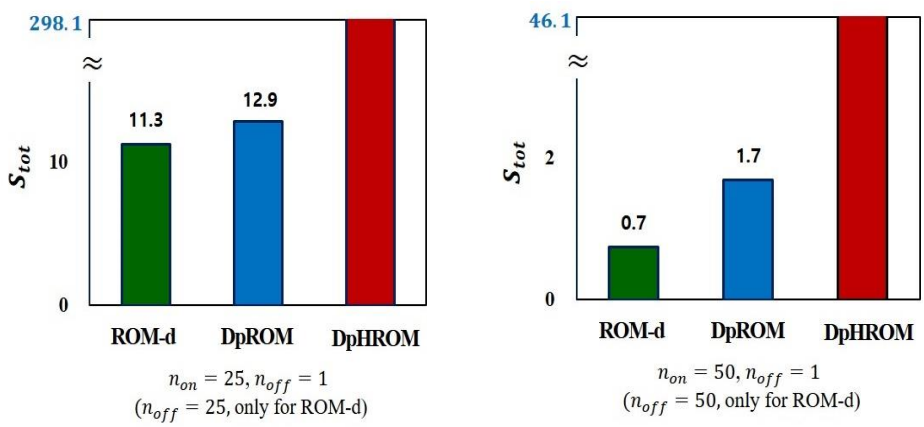

(a) Time-transient **(b) Frequency response**

Fig. 5.21 Total speed-up factor comparison among ROMs.

Chpater 6

Conclusion

In this dissertation, a projection-based MOR framework including hyper-reduction is developed for representing the geometrically nonlinear characteristics. In the presented framework, a geometrically nonlinear full-order representation, including the rotation effect, is developed to obtain the solutions required to build a reduced-order representation.

To systematically evaluate the hyper-reduction-based ROMs, POD-based MOR framework that includes hyper-reduction approaches, i.e., POD, POD-DEIM, POD-GNAT, and POD-ECSW, are compared in terms of accuracy, robustness, and computational efficiency. The following results are obtained:

- POD-DEIM approach might not maintain the symmetry of the approximate tangent matrix, which could lead to numerical divergence.
- Compared to the POD-DEIM, the POD-GNAT and POD-ECSW approaches exhibit better convergence characteristics owing to the minimized global residual error and preservation of the symmetric property, respectively, thereby enabling accurate predictions of the nonlinear formulations.
- The POD-ECSW approach achieves a high level of accuracy for parametric problems, with a less than 2% average relative error
- POD-ECSW shows the best computational improvement when compared to

FOM, POD-DEIM, and POD-GNAT (CPU times were 20.7, 1.9 and 1.4 times faster, respectively).

Consequently, ECSW approach provides the most robust reduced-order representation for the geometrically nonlinear formulations, including the broad parametric variation. It exhibits a higher computational efficiency than other hyper-reduction-based ROMs. Moreover, because of the smaller number of reduced basis used, ECSW is more advantageous in terms of computational efficiency. This dominated the construction of reduced-order representation during the online stage.

Based on the comparison results of the hyper-reduction approaches, a DpROM framework including hyper-reduction, named as DpHROM, is proposed to represent the geometric imperfection of solid components. ECSW approach is employed to reduce the computational expense in the existing DpROM. The relevant reduced-order tensors are obtained based on only a few selected elements. Herein, the QM-based reduction approach is applied to efficiently obtain the full-order solution required for ECSW execution. Two examples, a 3D slender beam and 54H60 propeller blade, are investigated to verify the accuracy and computational efficiency of the proposed framework. Based on the results, the following conclusions are drawn:

- DpROM approach combined with hyper-reduction can successfully conduct the parametric handling of the prescribed shape defect and geometrically nonlinear formulation.
- The proposed approach achieves a satisfactory accuracy while significantly

reducing the online computational time (with an average relative displacement field discrepancy smaller than 5%)

- In conjunction with QM-based ECSW, the proposed approach significantly decreases the off-line expense compared to the existing approach (the CPU time decreased by a factor of 34).
- In terms of speed-up performance, the proposed approach demonstrates an advantage for larger-dimensional representations.

Accordingly, the proposed DpHROM framework provides reliable accuracy for geometric nonlinearity within broad defect-parametric variations. Also, it exhibits an improved computational efficiency when compared to currently available ROMs. Such computational improvement can be advantageous for the uncertainty quantification of shape design optimization, involving a large number of FE discretization.

In future work, a technique to optimally select the reduced basis will be investigated to pre-select only a small number of reduced basis vectors. Moreover, the proposed approach could be applicable to more complex configurations, such as mistuned or damaged turbomachinery components.

Appendix A

Expression of the matrices $\mathbf{L_1}$, $\mathbf{L_2}$, and $\mathbf{L_3}$

The constant localization matrices $\mathbf{L}_1$, $\mathbf{L}_2$, and $\mathbf{L}_3$ are defined as follows:

$$L_1 = \begin{bmatrix} L_{111}=1, & L_{421}=1, & L_{531}=1, & L_{412}=1, & L_{222}=1, & L_{632}=1, & L_{513}=1, & L_{623}=1, & L_{333}=1, \\ L_{144}=1, & L_{454}=1, & L_{564}=1, & L_{445}=1, & L_{255}=1, & L_{665}=1, & L_{546}=1, & L_{656}=1, & L_{366}=1, \\ L_{177}=1, & L_{487}=1, & L_{597}=1, & L_{478}=1, & L_{288}=1, & L_{698}=1, & L_{579}=1, & L_{689}=1, & L_{399}=1, \end{bmatrix} \quad \text{(A.1)}$$

$$L_2 = -1 \times \begin{bmatrix} L_{111}=1, & L_{441}=1, & L_{571}=1, & L_{412}=1, & L_{242}=1, & L_{672}=1, & L_{513}=1, & L_{643}=1, & L_{373}=1, \\ L_{124}=1, & L_{454}=1, & L_{584}=1, & L_{425}=1, & L_{255}=1, & L_{685}=1, & L_{526}=1, & L_{656}=1, & L_{386}=1, \\ L_{137}=1, & L_{467}=1, & L_{597}=1, & L_{438}=1, & L_{268}=1, & L_{698}=1, & L_{539}=1, & L_{669}=1, & L_{399}=1, \end{bmatrix} \quad \text{(A.2)}$$

$$L_3 = -\frac{1}{2} \times \begin{bmatrix} L_{1111}=2, & L_{4211}=1, & L_{5311}=1, & L_{4121}=1, & L_{5131}=1, & L_{1441}=2, & L_{4541}=1, & L_{5641}=1, & L_{4451}=1, \\ L_{5461}=1, & L_{1771}=2, & L_{4871}=1, & L_{5971}=1, & L_{4781}=1, & L_{5791}=1, & L_{4112}=2, & L_{2212}=1, & L_{6312}=1, \\ L_{2122}=1, & L_{6132}=1, & L_{4442}=2, & L_{2542}=1, & L_{6642}=1, & L_{2452}=1, & L_{6462}=1, & L_{4772}=2, & L_{2872}=1, \\ L_{6972}=1, & L_{2782}=1, & L_{6792}=1, & L_{5113}=2, & L_{6213}=1, & L_{3313}=1, & L_{6123}=1, & L_{3133}=1, & L_{5443}=2, \\ L_{6543}=1, & L_{3643}=1, & L_{6453}=1, & L_{3463}=1, & L_{5773}=2, & L_{6873}=1, & L_{3973}=1, & L_{6783}=1, & L_{3793}=1, \\ L_{1214}=1, & L_{1124}=1, & L_{4224}=2, & L_{5324}=1, & L_{5234}=1, & L_{1544}=1, & L_{1454}=1, & L_{4554}=2, & L_{5654}=1, \\ L_{5564}=1, & L_{1874}=1, & L_{1784}=1, & L_{4884}=2, & L_{5984}=1, & L_{5894}=1, & L_{4215}=1, & L_{4125}=1, & L_{2225}=2, \\ L_{6325}=1, & L_{6235}=1, & L_{4545}=1, & L_{4455}=1, & L_{2555}=2, & L_{6655}=1, & L_{6565}=1, & L_{4875}=1, & L_{4785}=1, \\ L_{2885}=2, & L_{6985}=1, & L_{6895}=1, & L_{5216}=1, & L_{5126}=1, & L_{6226}=2, & L_{3326}=1, & L_{3236}=1, & L_{5546}=1, \\ L_{5456}=1, & L_{6556}=2, & L_{3656}=1, & L_{3566}=1, & L_{5876}=1, & L_{5786}=1, & L_{6886}=2, & L_{3986}=1, & L_{3896}=1, \\ L_{1317}=1, & L_{4327}=1, & L_{1137}=1, & L_{4237}=1, & L_{5337}=2, & L_{1647}=1, & L_{4657}=1, & L_{1467}=1, & L_{4567}=1, \\ L_{5667}=2, & L_{1977}=1, & L_{4987}=1, & L_{1797}=1, & L_{4897}=1, & L_{5997}=2, & L_{4318}=1, & L_{2328}=1, & L_{4138}=1, \\ L_{2238}=1, & L_{6338}=2, & L_{4648}=1, & L_{2658}=1, & L_{4468}=1, & L_{2568}=1, & L_{6668}=2, & L_{4978}=1, & L_{2988}=1, \\ L_{4798}=1, & L_{2898}=1, & L_{6998}=2, & L_{5319}=1, & L_{6329}=1, & L_{5139}=1, & L_{6239}=1, & L_{3339}=2, & L_{5649}=1, \\ L_{6659}=1, & L_{5469}=1, & L_{6569}=1, & L_{3669}=2, & L_{5979}=1, & L_{6989}=1, & L_{5799}=1, & L_{6899}=1, & L_{3999}=2, \end{bmatrix} \quad \text{(A.3)}$$

References

[1] Reddy, J., *Introduction to the Finite Element method*, 4th ed., McGraw-Hill Education, New York, 2019.

[2] Farhat, C., and Roux, F.-X., "A Method of Finite Element Tearing and Interconnecting and its Parallel Solution Algorithm," *International Journal for Numerical Methods in Engineering*, Vol. 32, No. 6, 1991, pp. 1205–1227.

[3] Snyder, L. E., "Forced Vibration and Flutter Design Methodology," *AGARD Manual on Aeroelasticity in Axial Flow Turbomachines Structural Dynamics and Aero-elasticity*, AG-298, Vol. 28, 1988.

[4] Benner, P. (Eds.), *Model Order Reduction Volume 1: System- and Data-Driven Methods and Algorithms*, De Gruyter, Berlin, 2021, Chap. 1.

[5] Wild, S. M., Regis, R. G., and Shoemaker, C. A., "Optimization by Radial Basis Function Interpolation in Trust-Regions," *SIAM Journal on Scientific Computing*, Vol. 30, No. 6, 2008, pp. 3197–3219.

[6] Guo, M., and Hesthaven, J. S., "Reduced Order Modeling for Nonlinear Structural Analysis Using Gaussian Process Regression," *Computer Methods in Applied Mechanics and Engineering*, Vol. 341, 2018, pp. 807–826.

[7] Oulghelou, M., and Allery, C., "Non-Intrusive Method for Parametric Model Order Reduction using a Bi-Calibrated Interpolation on the Grassmann Manifold," *Journal of Physics*, Vol 426, 2021, p. 109924.

[8] Hinton, G. E., and Salakhutdinov, R. R., "Reducing the Dimensionality of Data with Neural Networks," *Science*, Vol. 313, 2021, pp. 504-507.

[9] San, O., and Maulik, R., "Neural Network Closures for Nonlinear Model Order Reduction," *Advances in Computational Mathematics*, Vol. 44, 2018, pp. 1717-1750.

[10] Guo, M., Manzoni, A., Amendt, M, Conti, P., and Hesthaven, J. S., "Multi-fidelity Regression using Artificial Neural Networks: Efficient Approximation of Parameter Dependent Output Quantities," *Computer Methods in Applied Mechanics and Engineering*, Vol. 389, 2022, p. 114378.

[11] Li, S., and Yang, Y., "Hierarchical Deep Learning for Data-driven Identification of Reduced-order Models of Nonlinear Dynamical Systems," *Nonlinear Dynamics*, Vol. 105, 2021, pp. 3409-3422.

[12] Park, K., Jun, S., Baek, S., Cho, M., Yee, K., and Lee, D., "Reduced-order Model with an Artificial Neural Network for Aerostructural Design Optimization," *Journal of Aircraft*, Vol. 50, 2013, pp. 1106-1116.

[13] Lee, S., Jang, K., Cho, H., and Shin, S.-J., "Parametric Non-intrusive Model Order Reduction for Flow-fields using Unsupervised Machine Learning," *Computer Methods in Applied Mechanics and Engineering*, Vol. 384, 2021, p. 113999.

[14] Wang, Q., Hesthaven, J. S., and Ray, D., "Non-intrusive Reduced Order Modeling of Unsteady Flows using Artificial Neural Networks with Application to a Combustion Problem," *Journal of Computational Physics*, Vol. 384, 2019,

pp. 289-307.

[15] Benner, P., Gugercin, S., and Willcox, K., "A Survey of Projection-Based Model Reduction Methods for Parametric Dynamical Systems," *SIAM Review*, Vol. 57, No. 4, 2015, pp. 483–531.

[16] Chatterjee, A., "An Introduction to the Proper Orthogonal Decomposition," *Current Science* [online journal], Vol. 78, No. 7, 2000, pp. 808–817, URL: https://www.jstor.org/stable/24103957 [retrieved 15 March 2021].

[17] Kumar, N., Rajagopal, K., Balakrishnan, S. N., and Nguyen, N. T., "Proper Orthogonal Decomposition Technique for Near Optimal Control of Flexible Aircraft Wings," AIAA Paper 2013-4935, August 2013.

[18] Wang, B., Ma, X., Tian, K., Hao, P., Zhou, Y., and Quan, D., "Concurrent Patch Optimization of Hybrid Composite Plates based on Proper Orthogonal Decomposition," *AIAA Journal*, Vol. 57, No. 11, 2019, pp. 4915–4926.

[19] Kramer, B., and Willcox, K., "Nonlinear Model Order Reduction via Lifting Transformations and Proper Orthogonal Decomposition," *AIAA Journal*, Vol. 57, No. 6, 2019, pp. 2297–2307.

[20] Shane, C., and Jha, R., "Structural Health Monitoring of a Composite Wing Model using Proper Orthogonal Decomposition," AIAA Paper 2007-1726, April 2007.

[21] Kim, Y., Cho, H., Park, S., and Shin, S.-J., "Advanced Structural Analysis based on Reduced Order Modeling for Gas Turbine Blade," *AIAA Journal*, Vol. 56, No. 8, 2018, pp. 3369–3373.

[22] Tiso, P., Jansen, E., and Abdalla, M., "Reduction Method for Finite Element Nonlinear Dynamic Analysis of Shells," AIAA Journal, Vol. 49, No. 10, 2011, pp. 2295–2304.

[23] Idelsohn, S. R, and Cardona, A., "A Reduction Method for Nonlinear Structural Dynamic Analysis," *Computer Methods in Applied Mechanics and Engineering*, Vol. 49, No. 3, 1985, pp. 253-279.

[24] Weeger, O., Wever, U., and Simeon, B., "On the Use of Modal Derivatives for Nonlinear Model Order Reduction," *International Journal for Numerical Methods in Engineering*, Vol. 108, No. 13, 2016, pp. 405–425.

[25] Kim, K., Radu, A. G., Wang, X. Q., and Mignolet, M. P, "Nonlinear Reduced Order Modeling of Isotropic and Functionally Graded Plates," *International Journal of Non-Linear Mechanics*, Vol. 49, 2014, pp. 100-110.

[26] Mignolet, M. P., Przekop, A., Rizzi, S. A, and Spottswood, S. M, "A Review of Indirect/Nonintrusive Reduced Order Modeling of Nonlinear Geometric Structures, *Journal of Sound and Vibration*, Vol. 333, No. 4, 2014, pp. 2437-2460.

[27] Perez, R., Wang, X. Q., and Mignolet, M. P, "Nonintrusive Structural Dynamic Reduced Order Modeling for Large Deformations: Enhancements for Complex Structures, *Journal of Computational Nonlinear Dynamics*, Vol. 9, No. 3, 2014, p. 031008.

[28] Rizzi, S. A., and Muravyov, A. A., "Improved Equivalent Linearization Implementations Using Nonlinear Stiffness Evaluation," NASA TM-2001-

210838, L-18068, NAS 1.15:210838, 2001.

[29] Kim, E., Kim, H., and Cho, M., "Model Order Reduction of Multibody System Dynamics Based on Stiffness Evaluation in the Absolute Nodal Coordinate Formulation, *Nonlinear Dynamics*, Vol. 87, 2017, pp. 1901-1915.

[30] Hollkamp, J. J, and Gordon, R. W, "Reduced-order Models for Nonlinear Response Prediction: Implicit Condensation and Expansion," *Journal of Sound and Vibration*, Vol. 318, No. 4-5, 2008, pp. 1139-1153.

[31] Delhez, E., Nyssen, F., Golinval, J.-C., and Batailly, A., "Reduced Order Modeling of Blades with Geometric Nonlinearities and Contact Interactions," *Journal of Sound and Vibration*, Vol. 500, 2021, p. 116037.

[32] Vizzaccaro, A., Givois, A., Longobardi, P., Shen, Y, Deü, J.-F., Salles, L., and Touzé, C., "Non-intrusive Reduced Order Modelling for the Dynamics of Geometrically Nonlinear Flat Structures using Three-dimensional Finite Elements," *Computational Mechanics*, Vol. 66, 2020, pp. 1293-1319.

[33] Lee, J, Lee, J., Cho, H., Kim, E., and Cho, M., "Reduced-Order Modeling of Nonlinear Structural Dynamical Systems via Element-wise Stiffness Evaluation Procedure combined with Hyper-reduction," *Computational Mechanics*, Vol. 67, 2021, pp. 523-540.

[34] Chaturantabut, S., and Sorensen D. C., "Nonlinear Model Reduction via Discrete Empirical Interpolation," *SIAM Journal on Scientific Computing*, Vol. 32, No. 5, 2010, pp. 2737–2764.

[35] Barrault, M., Maday, Y., Nguyen, N.-C., and Patera, A., "An 'Empirical

Interpolation' Method: Application to Efficient Reduced-Basis Discretization of Partial Differential Equations," *Comptes Rendus Mathematique*, Vol. 339, No. 9, 2004, pp. 667–672.

[36] Cho, H., Shin, S.-J., Kim, H., and Cho, M., "Enhanced Model-Order Reduction Approach via Online Adaptation for Parametrized Nonlinear Structural Problems," *Computational Mechanics*, Vol. 651, No. 2, 2020, pp. 331–353.

[37] Radermacher, A., and Reese, S., "POD-Based Model Reduction with Empirical Interpolation Applied to Nonlinear Elasticity," *International Journal for Numerical Methods in Engineering*, Vol. 107. No. 6, 2015, pp. 477–495.

[38] Ghavamian, F., Tiso, P., and Simone, A., "POD–DEIM Model Order Reduction for Strain-Softening Viscoplasticity," *Computer Methods in Applied Mechanics and Engineering*, Vol. 317, No. 15, 2017, pp. 458–479.

[39] Negri, F., Manzoni., A, and Amsallem, D., "Efficient Model Reduction of Parameterized System by Matrix Discrete Empirical Interpolation," *Journal of Computational Physics*, Vol. 303, No. 15, 2015, pp. 431–454.

[40] Bonomi, D., Manzoni, A., and Quarteroni, A., "A Matrix DEIM Technique for Model Reduction of Nonlinear Parametrized Problems in Cardiac Mechanics," *Computer Methods in Applied Mechanics and Engineering*, Vol. 324, No. 1, 2017, pp. 300–326.

[41] Willcox, K., "Unsteady Flow Sensing and *Estimation* via the Gappy Proper Orthogonal Decomposition," AIAA Paper 2004-2415, July 2004.

[42] Chaturantabut, S., and Sorensen, D. C., "Application of POD and DEIM on

Dimension Reduction of Non-linear Miscible Viscous Fingering in Porous Media," *Mathematical and Computer Modelling of Dynamical Systems*, Vol. 17, No. 4, 2011, pp. 337–353.

[43] Hinze, M., and Kunkel, M., "Discrete Empirical Interpolation in POD Model Order Reduction of Drift-Diffusion Equations in Electrical Networks," *Scientific Computing in Electrical Engineering (SCEE 2010)*. Springer-Verlag, Berlin, 2012, pp. 423–431.

[44] Cosimo, A., Cardona, A., and Idelsohn, S., "Improving the k-Compressibility of Hyper Reduced Order Models with Moving Sources: Applications to Welding and Phase Change Problems," *Computer Methods in Applied Mechanics and Engineering*, Vol. 274, 2014, pp. 237–263.

[45] Carlberg, K., Amsallem, D., Avery, P., Zahr, M., and Farhat, C., "The GNAT Nonlinear Model Reduction Method and Its Application to Fluid Dynamics Problems," AIAA Paper 2011-3112, June 2011.

[46] Carlberg, K., Farhat, C., Cortial, J., and Amsallem, D., "The GNAT Method for Nonlinear Model Reduction: Effective Implementation and Application to Computational Fluid Dynamics and Turbulent Flows," *Journal of Computational Physics*, Vol. 242, No. 1, 2013, pp. 623–647.

[47] Farhat, C., Avery, P., Chapman, T., and Cortial, J., "Dimensional Reduction of Nonlinear Finite Element Dynamic Models with Finite Rotations and Energy-based Mesh Sampling and Weighting for Computational Efficiency," *International Journal for Numerical Methods in Engineering*, Vol. 98, No. 9,

2014, pp. 625–662.

[48] Farhat, C., Chapman, T., and Avery, P., "Structure-preserving, Stability, and Accuracy Properties of the Energy-conserving Sampling and Weighting Method for the Hyper Reduction of Nonlinear Finite Element Dynamic Models," *International Journal for Numerical Methods in Engineering*, Vol. 102, No. 5, 2015, pp. 1077–1110.

[49] Grimberg, S., and Farhat, C., "Hyperreduction of CFD Models of Turbulent Flows using a Machine Learning Approach," AIAA Paper 2020-0363, January 2020.

[50] Soldner, D., Brands, B., Zabihyan, R., Steinmann, P., and Mergheim, J., "A Numerical Study of Different Projection-based Model Reduction Techniques Applied to Computational Homogenisation," *Computational Mechanics*, Vol. 60, No. 4, 2017, pp. 613–625.

[51] Jain, S., and Tiso, P., "Simulation-free Hyper-reduction for Geometrically Nonlinear Structural Dynamics: A Quadratic Manifold Lifting Approach," *Journal of Computational Nonlinear Dynamics*, Vol. 13, No. 7, 2018, p. 071003.

[52] Pourkiaee, S., and Zucca, S., "A Reduced Order Model for Nonlinear Dynamics of Mistuned Bladed Disks with Shroud Friction Contacts," *Journal of Engineering for Gas Turbines and Power*, Vol. 141, No. 1, 2019, p. 011031.

[53] Farokhi, H., Ghayesh, M., and Amabili, M., "Nonlinear Dynamics of a Geometrically Imperfect Microbeam based on The Modified Couple Stress Theory," *International Journal of Engineering Science*, Vol. 68, 2013, pp. 11-23.

[54] Wang, H., Guilleminot, J., Schafer, B. W, and Tootkabonia, M., "Stochastic Analysis of Geometrically Imperfect Thin Cylindrical Shells using Topology-aware Uncertainty," *Computer Methods in Applied Mechanics and Engineering*, Vol. 393, 2022, p. 114780.

[55] Decker, K. M, "The Monte Carlo Method in Science and Engineering: Theory and Application," *Computer Methods in Applied Mechanics and Engineering*, Vol. 89, No 1-3. 1991, pp. 463-483.

[56] Marconi, J., Tiso, P., and Braghin, F., "A Nonlinear Reduced Order Model with Parametrized Shape Defects," *Computer Methods in Applied Mechanics and Engineering*, Vol. 360, 2020, p. 112785.

[57] Marconi, J., Tiso, P., Quadrelli, D. E., and Braghin, F., "Higher-order Parametric Nonlinear Reduced-order Model for Imperfect Structures using Neumann Expansion," *Nonlinear Dynamics*, Vol. 140, 2021, pp. 3039-3063.

[58] Kim, Y., Kang, S., Cho, H., and Shin, S.-J., "Improved Nonlinear Analysis of a Propeller Blade based on Hyper-reduction*," AIAA Journal*, Vol. 60, No. 3, 2022, pp. 1909–1922.

[59] Kang, S., Kim, Y., Cho, H., and Shin, S.-J., "Improved Hyper-reduction Approach for the Forced Vibration Analysis of Rotating Components," Computational Mechanics, Vol. 69, 2022. pp. 1443-1456.

[60] Kim, Y., Kang, S., Song, D., Cho, H., and Shin, S.-J., "Efficient Nonlinear Dynamic Analysis of a Rotating Blade with Shape Defects," GPPS paper 2022-0139, September 2022.

[61] Kim, Y., Kang, S., Cho, H., Kim, H., and Shin, S.-J., "Parametric Reduced-order Modeling Enhancement for a Geometrically Imperfect Component via Hyper-reduction," *Computer Methods in Applied Mechanics and Engineering*, published online, October 2022.

[62] Dickens, J. M., Nakagawa, J. M., and Wittbrodt, M. J., "A Critique of Mode Acceleration and Modal Truncation Augmentation Methods for Modal Response Analysis," *Computers and Structures*, Vol. 188, No. 6, 1997, pp. 985-998.

[63] Cornwell, R. E., Craig, R. R., and Johnson, C. P., "On the Application of the Mode-Acceleration Method to Structural Engineering Problems," *Earthquake Engineering and Structural Dynamics*, Vol. 11, 1983, pp. 679-688.

[64] Dickens, J. M., and Pool, K. V., "Modal Truncation Vectors and Periodic Time Domain Analysis Applied to a Cyclic Symmetry Structure," *Computers and Structures*, Vol. 45, No. 4, 1997, pp. 985-998.

[65] Jain, S., and Tiso, P., Rutzmoser, J. B., and Rixen, D. J., "A Quadratic Manifold for Model Order Reduction of Nonlinear Structural Dynamics," *Computers and Structures*, Vol. 188, 2017, pp. 80-94.

[66] Wu, L., and Tiso, P., "Nonlinear Model Order Reduction for Flexible Multibody Dynamics: A Modal Derivatives Approach," *Multibody System Dynamics*, Vol. 36, 2016, pp. 405-425.

[67] Wu, L., Tiso, P., Tatsis, K., and Chatzi, E., "A Modal Derivatives Enhanced Rubin Substructuring Method for Geometrically Nonlinear Multibody Systems,"

Multibody System Dynamics, Vol. 45, 2019, pp. 57-58.

[68] Sirovich L., "Turbulence and the dynamics of coherent structures," *Quarterly of Applied Mathematics*, Vol. 45, 1987, pp. 561–590.

[69] Chung, J., and Hulbert, G. M., "A Time Integration Algorithm for Structural Dynamics with Improved Numerical Dissipation: The Generalized-α Method," *Journal of Applied Mechanics*," Vol. 60, No. 2, 1993, pp. 371-375.

[70] Bathe, K. J., *Finite Element Procedures*, 2nd ed., Klaus-Jürgen Bathe, Watertown, MA, 2014, Chaps. 6, 9.

[71] Guo, D., Chu, F. L., and Zheng, Z. C., "The Influence of Rotation on Vibration of a Thick Cylindrical Shell," *Journal of Sound and Vibration*, Vol. 242, No. 3, 2001, pp. 487–505.

[72] Alves, M. L., Rodrigues, J. M. C., and Martins, P. A. F., "Simulation of Three-Dimensional Bulk Forming Processes by Finite Element Flow Formulation," *Modelling and Simulation in Materials Science and Engineering*, Vol. 11, No. 5, 2003, pp. 803-821.

[73] Anonymous, *Intel Math Kernel Library developer reference, Ver. 2020*. Intel, Santa Clara, CA, 2020.

[74] Carlberg, K., Bou-Mosleh, C., and Farhat, C., "Efficient Nonlinear Model Reduction via a Least-Squares Petrov-Galerkin Projection and Compressive Tensor Approximations," *International Journal for Numerical Methods in Engineering*, Vol. 86, No. 2, 2011, pp. 155–181.

[75] Benner, P. (Eds.), *Model Order Reduction Volume 1: System- and Data-Driven*

Methods and Algorithms, De Gruyter, Berlin, 2021, Chap. 4.

[76] Barbič, J., and James, D., "Real-time Subspace Integration for St. Venant-Kirchhoff Deformable Models," *ACM Transactions on Graphics*, Vol. 24, No. 3, 2005, pp. 982-990.

[77] Cardarelli, F., *Materials Handbook*, 2nd ed., Springer-Verlag, London, 2008, Chaps 1-2.

[78] Anonymous, *ANSYS Mechanical, Software Package, Ver. 20.1*, ANSYS, Inc., Canonsburg, PA, 2020.

[79] Misra, AK., and Greenbauer-Seng, LA., "Aerospace Propulsion and Power Materials and Structures Research at NASA Glenn Research Center," *Journal of Aerospace Engineering*, Vol. 26, No. 2, 2013, pp. 459-490.

[80] Moffatt, S., He, L., "Blade forced response prediction for industrial gas turbines," *Journal of Propulsion and Power*, Vol. 21, 2005, pp. 707–714.

[81] Bazoune, A., "Relationship between softening and stiffening effects in terms of Southwell coefficients," *Journal of Sound and Vibration,* Vol. 287, 2005, pp. 1027–1030.

[82] Budiansky, B., "Theory of Buckling and Post-buckling Behavior of Elastic Structures," *Advances in Applied Mechanics*, Vol. 14, 1974, pp. 1-65.

[83] Wang, X., Chen, S., and Li, C., "Generalized Neumann Expansion and its Application in Stochastic Finite Element Methods," *Mathematical Problems in Engineering*, Vol. 2013, 2013. pp. 1-13.

[84] Rutzmoser, J. B., and Rixen, D. J., Tiso, P., and Jain, S., "Generalization of

Quadratic Manifolds for Reduced Order Modeling of Nonlinear Structural Dynamics," *Computers and Structures*, Vol. 188, No. 7, 2017, pp. 196-209.

[85] Tiso, P., "Optimal Second Order Reduction Basis Selection for Nonlinear Transient Analysis," *Conference proceedings of the society for experimental mechanics series*, Vol. 3, 2011, pp. 27-39.

[86] Vizzaccaro, A., Salles, L., and Touzé, C., "Comparison of Nonlinear Mappings for Reduced-order Modelling of Vibrating Structures: Normal Form Theory and Quadratic Manifold Method with Modal Derivatives," *Nonlinear Dynamics*, Vol. 103, 2020, pp. 3335-3370.

[87] Jain, S., Marconi, J., and Tiso, P., *YetAnotherFEcode* v1.1.1, Zenodo.

[88] Bader, B. W., Kolda, T. G., Acar, E., and Dunlavy, D. M., *Matlab tensor toolbox version 3.1*, 2019, URL: https://www.tensortoolbox.org.

[89] Chapman, T., Avery, P., Collins, P., and Farhat, C., "Accelerated Mesh Sampling for the Hyper Reduction of Nonlinear Computational Models," *International Journal for Numerical Methods in Engineering*, Vol. 109, No. 12, 2017, pp. 1623–1654.

[90] Stein, M., "Large Sample Properties of Simulations using Latin Hypercube Sampling," *Technometrics*, Vol. 29, No. 2, 1987, pp. 143-151.

국문초록

투영기반 하이퍼 차수축소모델링 및 비선형 구조 동역학에 대한 응용 연구

김용세

서울대학교 대학원

항공우주공학과

본 논문에서는 기하 비선형 예측이 가능한 유한요소 기반 비선형 구조해석 프레임워크를 개발하였다. 비선형 동적 해석은 반복해법 알고리즘에 의해 많은 계산이 요구된다. 이러한 계산 비용을 줄이기 위해 하이퍼 축소법을 결합한 차수축소모델링을 적용하였다. 효율적인 계산 수행을 위해 이산적 경험 보간법(DEIM), Gauss-Newton 근사법(GNAT), 에너지 보존 샘플링 및 가중치(ECSW) 등 하이퍼 축소법을 각각 적용하였다. 개발한 프레임워크를 이용하여 매개변수화 된 물성치와 하중을 포함한 비선형 시간과도 수치해석을 수행하였다. 그 결과, DEIM 대비 GNAT 과 ECSW 가 정확도 및 강건성 측면에서 향상된 차수축소 표현식을 구축하였으며, 특히 ECSW 가 다른 차수축소모델 대비 가장 높은 계산 효율성을 보여주었다.

반면, 구조물의 기하학적 결함 또는 불완전성에 의해 유한요소

표현식이 변화할 경우, 차수축소 표현식을 재구성하기 위해 높은 계산 비용이 요구된다. 이러한 계산적 비효율성을 해결하기 위해 매개변수화된 형상 결함을 효율적으로 고려할 수 있는 차수축소모델링을 제안하였다. 이 때, 차수축소 표현식은 결함과 실제 변형 관련 축소 텐서들로 구성된 다항 함수로 구축된다. 하지만, 많은 수의 이산화된 유한요소를 사용하여 축소 텐서를 구성하기 위해서는 일반적으로 상당한 계산 자원이 필요하다. 따라서, 이차 매니폴드 (quadratic-manifold) 기반 ECSW 기법을 적용하여 최적으로 선택된 몇 가지 요소에 관해 축소 텐서를 구축하였다. 제안한 프레임워크를 회전기계 구성품을 대상으로 시간과도 및 주파수 응답 해석을 각각 수행한 결과, 형상 결함 매개변수 변화에 대해 정확한 예측이 가능할 뿐만 아니라, 기존 차수축소 모델링 기법 대비 계산 비용을 상당히 절감하였다.

주제어: 투영기반 차수축소모델, 적합 직교 분해, 기하 비선형, 구조 동역학, 하이퍼 축소, 형상결함 파라메트릭 차수축소모델

학번: 2019-32693